Dissertation zur Erlangung des Doktorgrades
der Fakultät für Chemie und Pharmazie
der Ludwig-Maximilians-Universität München

Pathological Notch3 aggregation: Role of cysteine-sparing mutations and antiaggregatory strategies in CADASIL

von
Patrizia Yvonne Fresser geb. Hanecker
aus
Augsburg

2016

Erklärung

Diese Dissertation wurde im Sinne von § 7 der Promotionsordnung vom 28. November 2011 von Herrn PD. Dr. Christof Haffner betreut und von Herrn Prof. Dr. Don Lamb von der Fakultät für Chemie und Pharmazie vertreten.

Eidesstattliche Versicherung

Diese Dissertation wurde eigenständig und ohne unerlaubte Hilfe erarbeitet.

München, den

(Patrizia Fresser)

Dissertation eingereicht am 04.11.2016

1. Gutachter: Prof. Dr. Don Lamb

2. Gutachter: PD Dr. Christof Haffner

Mündliche Prüfung am 14.12.2016

Summary

Cerebral small vessel disease (SVD), characterized by pathological processes that affect structure and function of the brain microvasculature and result in subsequent damage of the cerebral white and deep grey matter, is the main cause for long-term disability and vascular dementia. Cerebral autosomal dominant arteriopathy with subcortical infarcts and leukoencephalopathy (CADASIL), the most common form of monogenic SVD leading to early-onset stroke and vascular dementia, is caused by mutations in the Notch3 transmembrane receptor. Accumulation and deposition of the extracellular domain of Notch3 (Notch3-ECD) in blood vessel walls are the earliest disease manifestations. However, the underlying molecular pathomechanism is incompletely understood and specific treatment options are not available. To study the aggregation behavior of Notch3 mutants we have recently developed an *in vitro* aggregation assay based on recombinant Notch3-ECD fragments and their detection by the single-molecule spectroscopy technique called scanning for intensely fluorescent targets (SIFT).

While the vast majority of CADASIL mutations alter the number of cysteine residues within the Notch3-ECD, over the last years several mutations not involving a cysteine have been reported to be associated with a CADASIL-like phenotype provoking a debate about their clinical significance. In the first part of this work, the *in vitro* assay was applied to study the pathogenic potential of five of these mutations. Three of them showed an aggregation behavior similar to cysteine-affecting mutations, a finding supported by the typical CADASIL-like clinical appearance of the mutation carriers and we thus classified them as pathogenic mutations. For the two other mutants the available clinical data had been fragmentary and in agreement with that, no significant aggregation potential was observed, strongly suggesting that they represent apathogenic polymorphisms. Thus, our *in vitro* assay offers new insights into the Notch3 aggregation mechanism and may serve as diagnostic tool determining the clinical relevance of cysteine-sparing mutations.

In the second part of this thesis, the *in vitro* assay was used to search for small-molecule aggregation inhibitors. Several synthetic compounds of the diphenylpyrazole (DPP) class as well as natural polyphenolic substances with antiaggregatory properties were identified. They not only inhibited the *de novo* aggregation of mutant Notch3 but were also capable of dissolving pre-formed aggregates. Some of the compounds were subsequently shown to be also effective in a novel cellular assay based on the accumulation of mutant Notch3 in the extracellular matrix (ECM) of mouse embryonic fibroblasts (MEF). With this study on drug-mediated inhibition of Notch3 accumulation we have laid a basis for an anti-aggregation therapy.

Zusammenfassung

Zerebrale Mikroangiopathien sind die häufigste Ursache für Langzeitbehinderung und vaskuläre Demenz. Sie sind durch pathologische Prozesse charakterisiert, die die Struktur und Funktion der Mikrovaskulatur im Gehirn beeinträchtigen und dadurch zu Schädigungen der weißen und tiefen grauen Substanz führen. CADASIL (zerebrale autosomaldominante Arteriopathie mit subkortikalen Infarkten und Leukoenzephalopathie), die häufigste monogene Form zerebraler Mikroangiopathien, führt zu juvenilen Schlaganfällen und vaskulärer Demenz und wird durch Mutationen im Notch3 Rezeptor verursacht. Frühestes pathologisches Merkmal ist die Akkumulation und Ablagerung der extrazellulären Domäne von Notch3 (Notch3-ECD) in den Wänden kleiner Blutgefäße. Allerdings ist bisher wenig über den zu Grunde liegenden molekularen Pathomechanismus bekannt und spezielle Behandlungsmöglichkeiten sind nicht verfügbar. Um das Aggregationsverhalten von Notch3 Mutanten zu studieren, haben wir einen *in vitro* Aggregationsassay entwickelt, der auf rekombinanten Notch3-ECD Fragmenten und ihrer Detektion mittels SIFT (scanning for intensely fluorescent targets) beruht, einer speziellen Einzelmolekülspektroskopietechnik.

Während die Mehrheit der CADASIL Mutationen die Anzahl der Cysteinreste in der Notch3-ECD verändert, ist in den letzten Jahren mehrfach über Mutationen ohne Cysteinbeteiligung berichtet worden, die mit einem CADASIL-ähnlichen Phänotyp assoziiert sind und über deren klinische Relevanz derzeit diskutiert wird. Im ersten Teil dieser Arbeit wurde der *in vitro* Assay zur Untersuchung des pathogenen Potentials von fünf dieser Mutationen verwendet. Drei von ihnen zeigten ein ähnliches Aggregationspotential wie klassische Cystein-Mutationen, ein Befund, der durch die typischen CADASIL Symptome der Mutationsträger gestützt wird. Wir klassifizieren sie daher als pathogene Mutationen. Für die beiden anderen Mutanten, deren klinische Beschreibung lückenhaft war, konnte dementsprechend kein signifikantes Aggregationspotential beobachtet werden, so dass sie wahrscheinlich apathogene Polymorphismen darstellen. Somit eröffnet unser *in vitro* Assay neue Einblicke in den Notch3-Aggregationsmechanismus und könnte als diagnostische Methode zur Bestimmung der klinischen Relevanz von Nicht-Cystein Mutationen eingesetzt werden.

Im zweiten Teil dieser Arbeit wurde der *in vitro* Assay für die Suche nach kleinen Molekülen mit aggregationsinhibierender Aktivität eingesetzt. Mehrere synthetische Substanzen aus der Klasse der Diphenylpyrazole (DPP), sowie natürliche Polyphenole mit antiaggregatorischen Eigenschaften wurden identifiziert. Sie hemmten nicht nur die *de novo* Aggregation von einer Notch3 Mutante, sie waren auch in der Lage, präformierte Aggregate wieder aufzulösen. Für einige der Substanzen konnte anschließend auch eine Wirkung in

einem zellulären Assay gezeigt werden, der auf der Akkumulation einer Notch3 Mutante in der extrazellulären Matrix (ECM) muriner embryonaler Fibroblasten (MEF) beruht. Mit dieser Studie zur substanzvermittelten Hemmung der Notch3 Akkumulation haben wir den Grundstein für eine Antiaggregationstherapie gelegt.

Contents

1 Introduction

Stroke represents, after ischemic heart disease, the second leading cause of death with 6.7 million casualties worldwide in 2012.[1] Thus, it is a major burden for public health. Another huge impact on financial costs to society is caused by dementia. Whereas in 2010 around 25.6 million people were affected by dementia with worldwide costs of US $ 604 billion, the total number of cases in 2050 is projected to be about 115.4 million.[2]

Two main types of stroke can be distinguished (Figure 1.1): Haemorrhagic stroke and ischemic stroke. Haemorrhagic stroke accounts for about 20 % of the cases and arises from vessel wall rupture leading to extravasation of the blood into the surrounding tissue. In 80 % of the cases acute vessel occlusion or chronic hypoperfusion and subsequent depletion of oxygen and nutrients in the surrounding tissue occurs resulting in ischemic stroke.[3] The main causes for ischemic stroke are large-artery atherosclerosis, cardioembolism and small vessel disease (SVD).[4] SVD is - although accounting for only 20 % of all stroke cases - the main cause for long-term disability and vascular dementia, which represents the most common form of cognitive impairment after Alzheimer's dementia.[5]

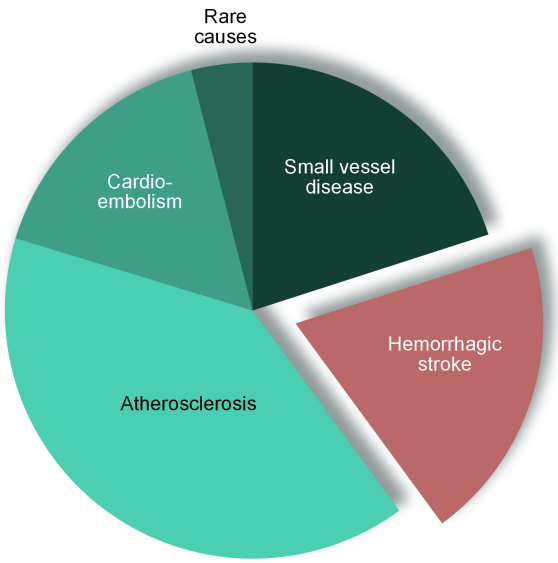

Figure 1.1: Distribution of hemorrhagic (red) and ischemic (green) stroke in white population. Ischemic stroke can be further subdivided into small vessel disease, cardioembolism, large artery atherosclerosis and other rare causes (adapted from Warlow et al.[3])

1.1 Cerebral small vessel disease

Cerebral SVD is characterized by pathological processes that affect structure and function of the brain microvasculature, including small arteries, perforating arterioles, capillaries and small veins and the subsequent damage of the cerebral white and deep grey matter.[5] Sporadic SVD normally remains unnoticed over years before becoming evident at higher age with sudden-onset stroke symptoms as well as neurological symptoms such as cognitive decline, dementia and depression.[6]

In contrast to large arteries, small arteries can not be visualized and investigated easily *in vivo*.[7] Thus, only the consequences of changes in the small vessel network, the parenchyma lesions can be detected with neuroimaging and therefore serve as a marker of small vessel disease.[5] These changes manifest in small subcortical infarcts, lacunes, white matter hyperintensities, visible perivascular spaces, cerebral microbleeds and brain atrophy.[6] Since pathological data are mainly available from end-stage SVD patients little is known about the pathogenesis and the earliest disease causing events. Histopathological characteristics are mainly described as loss of vascular smooth muscle cells (vSMCs), thickening of the vessel wall and narrowing of the lumen which can lead to reduced blood flow.[5] However, it is still under debate how this correlates with the neurological and cognitive symptoms.[6] Although risk factors such as age, hypertension, smoking, diabetes mellitus, atrial fibrillation and obesity have been identified[8], they account only for part of the disease risk[9] and other factors including genetics may be pivotal.

Besides the sporadic form of SVD, several monogenic forms have been identified that share the main clinical and pathological features of the disorder (Table 1.1). They include cerebral autosomal recessive arteriopathy with subcortical infarcts and leukoencephalopathy (CARASIL), retinal vasculopathy with cerebral leukodystrophy (RVCL), Collagen type IV-related SVD and cerebral autosomal dominant arteriopathy with subcortical infarcts and leukoencephalopathy (CADASIL).[10,11] Table 1.1 depicts the characteristic clinical features and affected genes for these inheritable forms of SVD. Due to their defined genetic etiology and early onset of the clinical symptoms, the monogenic SVD forms serve as valuable models to study vascular changes and biological pathways that finally lead to vascular dementia.

In this work we focus on CADASIL, the most common monogenic SVD. Although abundant clinical data are available, there is still a lack in the knowledge of the molecular pathomechanism and also specific treatment options are missing. Identifying details of the initiation factors as well as the examination of the progression of this disease may not only help to find a cure, but also to advance our understanding of sporadic SVD.

Table 1.1: Monogenic cerebral small vessel diseases. CADASIL: cerebral autosomal dominant arteriopathy with subcortical infarcts and leukoencephalopathy, CARASIL: cerebral autosomal recessive arteriopathy with subcortical infarcts and leukoencephalopathy, RVCL: retinal vasculopathy with cerebral leukodystrophy, COL4: collagen type IV

Disorder	Affected gene	Characteristic clinical features
CADASIL	*NOTCH3* (autosomal dominant)	migraine with aura, subcortical infarcts, mood disturbance, apathy, cognitive impairment
CARASIL	*HTRA1* (autosomal recessive)	recurrent small strokes, alopecia, kyphosis, spondylosis
RVCL	*TREX1* (autosomal dominant)	retinal vasculopathy, strokes, cognitive dysfunction, headaches, personality disorders
COL4-related disorders	*COL4A1/A2* (autosomal dominant)	ischemic stroke, intracerebral haemorrhages, migraines with/without aura, dementia

1.2 CADASIL

Starting in the 1970's first descriptions of European families suffering from a vascular dementing disease appeared in the literature. The disease was described with similar pathological findings, but the name varied from chronic familial vascular encephalopathy[12], hereditary multi-infarct dementia[13,14], autosomal dominant syndrome with stroke-like episodes and leukoencephalopathy[15] to a familial disorder with subcortical ischemic strokes, dementia, and leukoencephalopathy[16]. In 1993, Tournier-Lasserve et al.[17] linked the disease to chromosome 19 and created the acronym CADASIL, **C**erebral **A**utosomal **D**ominant **A**rteriopathy with **S**ubcortical **I**nfarcts and **L**eukoencephalopathy depicting the main characteristics of the disease. The same group identified *NOTCH3* as the defective gene[10] and described the stereotypic mutations in detail three years later.[18] Until today over 200 different CADASIL mutations have been identified. The disease prevalence is estimated to be about 4 per 100 000.[11]

The neurological and neuropsychological symptoms in CADASIL patients can appear isolated but develop successively in general with some variances in onset and duration (Figure 1.2). Although there is a high heterogeneity in clinical appearance between and also within families, the disease can be characterized by four principle symptoms: migraine with aura, subcortical ischemic events, mood disturbances/apathy and cognitive impairment.[11] The first manifestation in young CADASIL patients is primarily migraine with aura[19,20], but

since this symptom occurs in other neurological conditions as well, CADASIL is diagnosed often after the first ischemic episode occuring on average with 51 years.[21] Importantly, cognitive decline is already observed before the first ischemic strokes.[22] CADASIL progresses slowly with exacerbations of the symptoms. During the course of the disease cognitive and motoric abilities decline due to recurrent strokes leading to deficits in episodic memory, attention, executive and visuospatial functions together with psychomotor slowing and a narrowing of the field of interest.[23] The infarcts are located in the white matter or basal ganglia as well as in the brain stem, whereas the cerebral cortex is well preserved.[24,25] Finally, by the age of 65, 80 % of CADASIL patients are demented.[26] Death occurs within a mean period of 23 years after onset of the disease.[26]

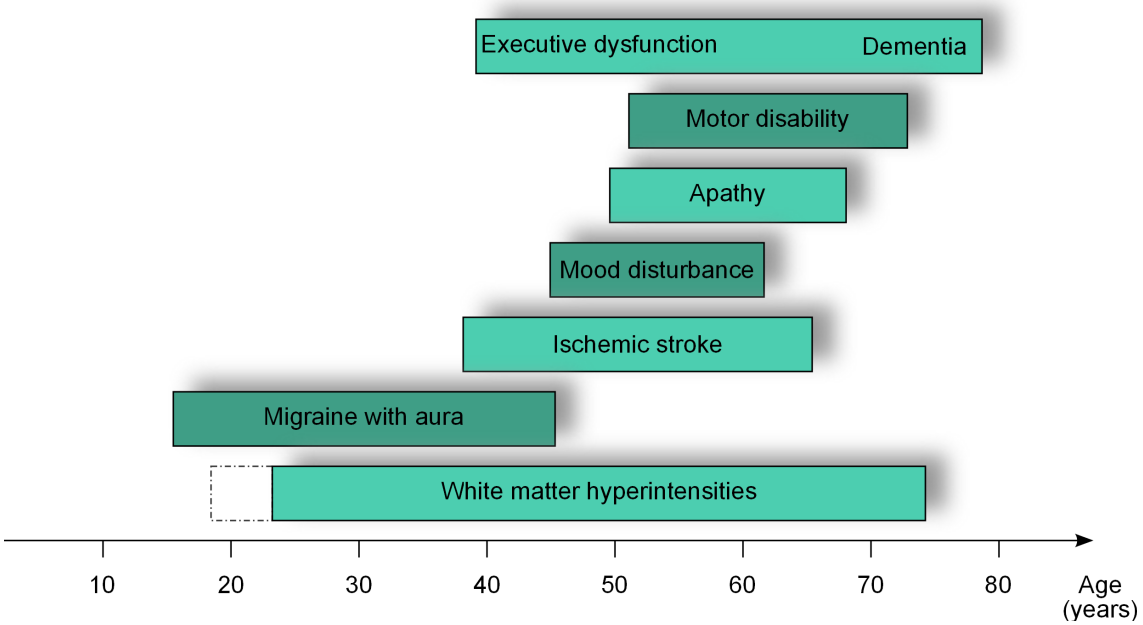

Figure 1.2: Time axis of the main clinical manifestations of CADASIL. The earliest appearance of magnetic resonance imaging (MRI) white matter abnormalities is unknown (dotted line) Adapted from Chabriat et al.[11]

Changes in the brain parenchyma of CADASIL patients can be detected by cranial MRI. Increased signals on T2-weighted or fluid-attenuated inversion recovery images represent white matter abnormalities, that normally precede the onset of other symptoms by 10-15 years.[11] These white matter hyperintensities (WMH) can also be observed in asymptomatic patients carrying the mutated gene and may be associated with axonal demyelination.[27] Since periventricular WMH regions are very common in CADASIL patients with a prevalence of 96 % , their absence almost excludes the diagnosis.[27] Furthermore, lacunar lesions, subcortical infarcts and microstructural tissue alterations that finally lead to cortical thinning and brain atrophy characterize the etiopathology of CADASIL patients.[28–31]

MRI observations have a high diagnostic value on a macroscopic level, but typical CADASIL abnormalities can also be detected by microscopic and ultrastructural inves-

tigations. Histological stainings of post-mortem brains show a loss of vSMCs[32,33] and a thickening of the walls of small and medium-sized leptomeningeal and penetrating arteries in the white matter resulting in lumen stenosis.[25,33] This non-arteriosclerotic fibrosis may be due to accumulation of extracellular matrix (ECM) proteins, such as fibronectin and type I collagen[24,25,34] as well as deposition of degenerated vSMCs debris.[25,33] These morphological changes share CADASIL patients with patients suffering from sporadic SVD.

Although the symptoms are exclusively neurological, CADASIL is a systemic arteriopathy, since vascular changes can also be found in other organs, for example in skin and muscle, providing histological diagnosis options.[35,36] Apart from the thickening of arterial walls (Figure 1.3 A), the presence of granular osmiophilic material (GOM) is an invariant hallmark of CADASIL (Figure 1.3 B). GOM, a granular electron-dense extracellular material, can be found typically close to the surface of vSMCs, varying in size between 0.2 to 0.8 µm and is composed of 10 to 15 nm granules.[24,35,36] These deposits are negative for histological stainings with Congo red, thioflavin and other markers of cerebrovascular diseases[24,37] and have, on the other hand, not been detected in other diseases.[36]

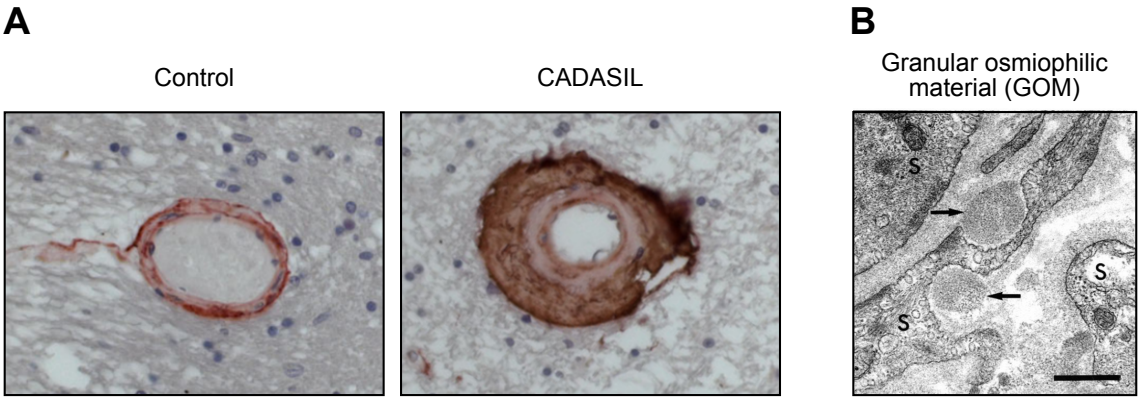

Figure 1.3: Appearance of arterial changes in CADASIL. A) Paraffin-embedded brain sections of a healthy control and a CADASIL patient were stained for fibronectin, counterstained with hematoxylin and analyzed by bright-field microscopy. Brain vessel of CADASIL patient shows characteristic thickening of the vessel wall. Adapted from Kast et al.[34] B) Electron micrograph of a dermal artery showing deposits of GOM (arrows) at the surface of vSMCs (S). Adapted from Kalimo et al.[25]

Despite of all the diagnostic tools developed over the years, there is still a lack in effective treatment of CADASIL. Until now there is no curative therapy for CADASIL, only symptoms can be medicated. Forteza et al.[38] published in 2001 that acetazolamide can alleviate the symptoms of migraine with aura in CADASIL patients. Furthermore, Dichgans et al.[39] observed a improvement in executive functions of patients treated with the cholinesterase inhibitor donepezil, although the results were not significant. Peters et al.[40] on the other hand described that the administration of L-arginine induces increased cerebral vasoreactivity in CADASIL patients, thus suggesting it as a possible substance for therapeutic treatment.

1.3 The Notch3 Receptor

1.3.1 Structure and Function

Joutel et al.[10] identified in 1996 *NOTCH3* on chromosome 19p13 as the mutated gene underlying the CADASIL pathology. The human *NOTCH3* gene encompasses 41.3 kilobases containing 33 exons. It encodes the 280 kDa (2321 amino-acids) single-pass type I transmembrane receptor Notch3 which belongs to the family of Notch proteins conserved from worms to man. Notch signaling between neighboring cells plays an important role in cell type differentiation and organogenesis.[41]

The four mammalian isoforms of Notch are highly homologous and share the same domain structure. Notch3 consists of a large extracellular domain (ECD) containing 34 epidermal growth factor (EGF)-like repeats, three cysteine-rich lin12/notch repeats (LNR), a transmembrane domain and an intracellular domain (ICD) with seven ankyrin repeats flanked by two nuclear localization signals and a PEST motif (Figure 1.4).

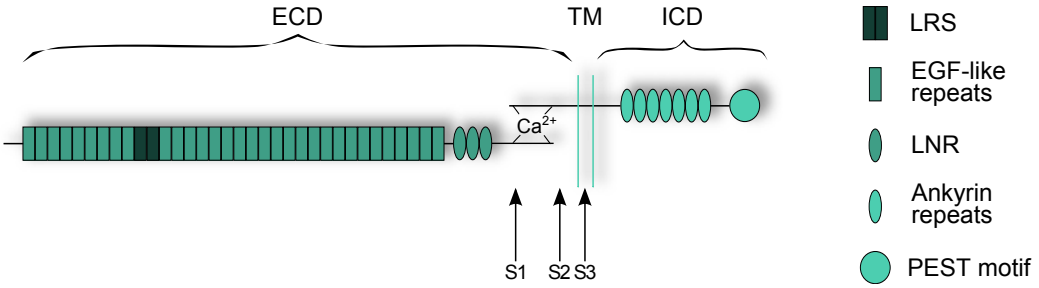

Figure 1.4: Notch3 structure. The heterodimer is built up of an ECD comprising 34 EGF-like repeats and three cysteine-rich LNR repeats including the ligand recognition site (LRS) on EGF-like repeats 10/11. After the transmembrane domain (TM), an ICD follows with seven ankyrin repeats and a PEST motif. Arrows indicate the three cleavage sites S1-3.

The protein is synthesized as a 280 kDa precursor which undergoes in total three proteolytic cleavages (S1-S3) during maturation and signaling. The S1 cleavage occurs in the Golgi complex by a furin-like convertase generating a non-covalently associated heterodimer which is subsequently inserted into the plasma membrane.[42] S2 and S3 cleavages are initiated during signaling. Membrane-bound ligands (e.g. Delta or Serrate) from neighboring cells interact with the ligand binding domain in the Notch EGF-like repeats 10/11 leading to the extracellular S2 cleavage by an ADAM family metalloprotease, the TNFα-converting enzyme (TACE) close to the transmembrane domain.[43] The ECD is shedded and the truncated receptor becomes susceptible for S3 cleavage by γ-secretase, an unusual protease complex cleaving within the plasma membrane.[44] This results in the release of the ICD into the cytosol, its translocation to the nucleus and association with DNA-binding transcriptional regulators like RBP-Jκ to activate target genes.[45] In the

extracellular space the ligand-Notch3 ECD complex is internalized by the signaling cell, followed by recycling of the ligand and degradation of Notch3 ECD.[46]

Mutations in various members of the Notch signaling pathways cause developmental diseases affecting different human organs.[47] In contrast, CADASIL is an adult-onset disease. Notch3 is mainly expressed in mural cells (vSMCs, pericytes) of the vasculature[48] and studies on Notch3 knockout (*Notch3* $^{-/-}$) mice demonstrated that Notch3 is non-essential for survival, since the mice are viable and fertile. However, structural defects of arteries in adult mice, compromised arterial pressure and cerebral blood flow (CBF), as well as the abnormal shape of adult vSMCs demonstrate, that Notch3 is an essential regulator of arterial differentiation and maturation.[49–51]

1.3.2 Classical Notch3 mutations

In over 500 families more than 200 mutations have been reported, all of them located in exons 2-24 out of the 33 exons of *NOTCH3*.[11] These exons encode for the 34 EGF-like repeats of the ECD, each of which contains six highly conserved cysteine residues. These form three disulfide bridges between cysteines 1 and 3, 2 and 4 and 5 and 6 (Figure 1.5 A) which are essential for the 3D structure of each EGF-like repeat.[52] 95 % of the CADASIL-linked mutations are missense mutations, only few are in-frame deletions or splice-site mutations, but almost all mutations lead to an odd number of cysteines either by gain or loss of one cysteine (Figure 1.5 B).[11] Containing over 85 % of the mutations, the mutational hotspot can be found within EGF-like repeats 2 to 6 (Figure 1.6).[53] Until now, genetic screening for mutations in the *NOTCH3* gene is with almost 100 % sensitivity as well as 100 % specificity the gold standard for the CADASIL diagnosis.[53–55]

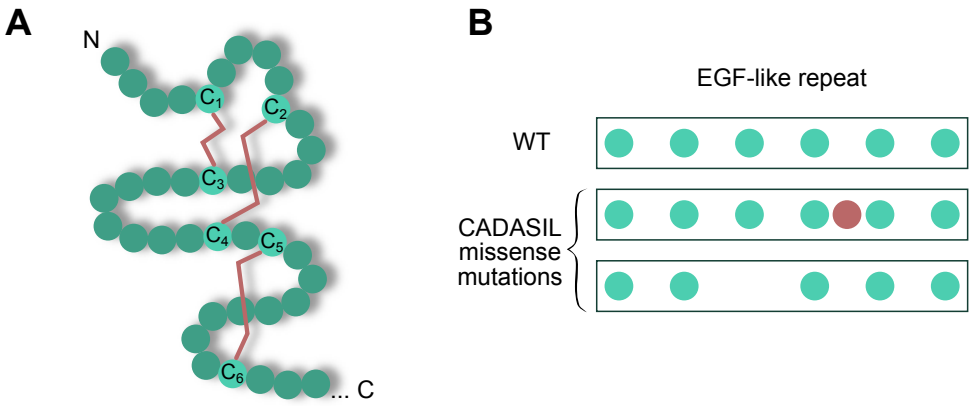

Figure 1.5: Schematic drawings of an EGF-like repeat and typical CADASIL mutations. A) Six highly conserved cysteine residues form three disulfide bridges (red) between C1-C3, C2-C4 and C5-C6. B) Typical CADASIL missense mutations lead to an odd number of cysteines either due to an additional one (red dot) or a lack of one. Adapted from Chabriat et al.[11]

A variety of *in vitro* and mouse studies revealed that Notch3 mutations typically neither influence receptor maturation nor ligand binding and activate the signaling cascade efficiently.[55–60] Together with the fact that the loss of Notch3 in *Notch3* $^{-/-}$ mice does not lead to the typical CADASIL pathology, this suggests that loss of function is not the prevalent pathogenic mechanism of CADASIL mutations. This hypothesis is also supported by data from different mouse models expressing mutated Notch3.[61–64] Taken all the data together, Joutel[65] suggested that a neomorphic toxic mechanism for mutant Notch3 rather than compromised canonical Notch3 function is the main cause for CADASIL.

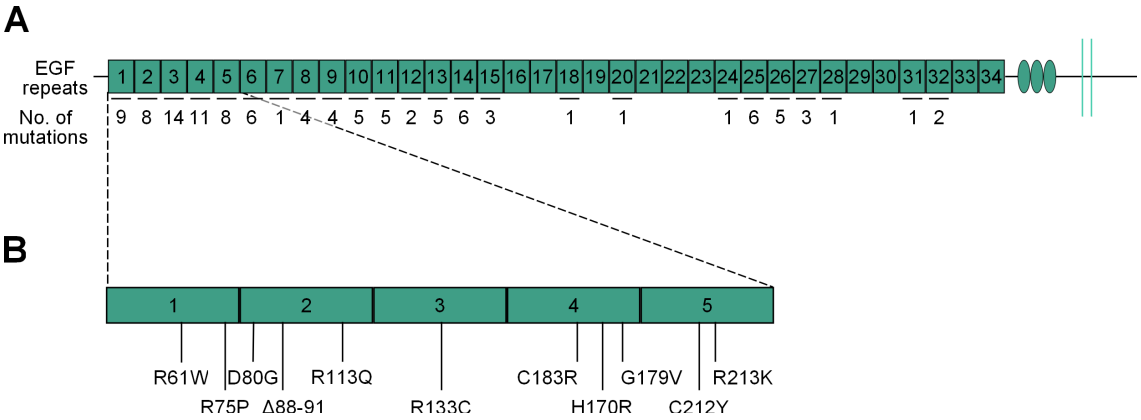

Figure 1.6: Distribution of Notch3 mutations in EGF-like repeats 1-34. A) Number of different mutations found in the EGF-repeats of extracellular domain of Notch3 (Notch3-ECD). B) Mutations and polymorphisms used in this work.

Joutel et al.[48] revealed that the S2 cleavage product, the 210 kDa Notch3-ECD, accumulates in the vSMC layer of vessel walls (Figure 1.7). Ishiko et al.[66] confirmed that the Notch3-ECD is one component of the GOM deposits. Data from patients reveal that the accumulation of Notch3 and the presence of GOM deposits are the earliest manifestations of CADASIL, already preceding the first symptoms.[67,68] These data are supported by experiments using a transgenic mouse model with a CADASIL-causing Notch3 point mutation that leads to the main pathological features of the disease including Notch3-ECD accumulation, followed by GOM deposits and later also to progressive white matter damage and reduced CBF.[63] This transgenic mouse thus serves as an early disease model and together with the patient data reveals the accumulation of Notch3-ECD as one of the first key features of CADASIL.

Thus, CADASIL can be considered a protein misfolding disease with dementia as final consequence. In this respect it resembles a variety of human diseases characterized by either extracellular or intracellular accumulation and deposition of insoluble aberrant or misfolded proteins. The most common ones are Alzheimer's disease (AD), Parkinson's disease (PD), Huntington disease (HD), Creutzfeldt-Jakob disease (CJD) and frontotemporal dementia (FTD). In contrast to CADASIL, the deposits found in these diseases (also called amyloidoses) contain mainly fibrillar material rich in β-sheet structures and

therefore bind to the histochemical dye Congo red, which, combined with polarized light, makes the protein appear green.

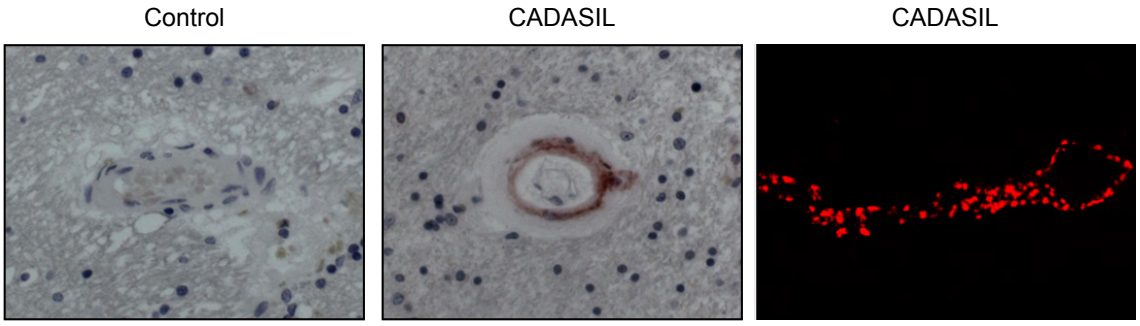

Figure 1.7: Accumulation of Notch3-ECD in the vessel wall. Left and middle: Paraffin-embedded brain sections of a healthy control and a CADASIL patient were stained for Notch3, counterstained with hematoxylin and analyzed by bright-field microscopy. Right: Frozen brain section of a CADASIL patient stained for Notch3 and analyzed by confocal fluorescent microscopy. Adapted from Kast et al. [34]

So far, the molecular mechanism underlying the aggregation of Notch3-ECD is still unknown. Already in 1997 Joutel et al. [18] hypothesized that aberrant dimerisation of the unpaired cysteine residues of two Notch3 proteins or with another cysteine-containing protein may lead to the accumulation of Notch3-ECD. This was confirmed by modeling the 3D structures of the first six EGF-like domains offering two potential pathomechanisms: 1) domain misfolding due to disulfide bridge reorganisation and 2) unphysiological intermolecular disulfide bridge formation. [69] Our group has developed an *in vitro* assay and demonstrated that aggregation of mutant proteins is triggered by their unpaired sulfhydryl groups. [70] We further obtained data from the analysis of a truncated purified Notch3-ECD fragment containing the first five EGF-like domains and showed that in contrast to wild-type (wt) protein CADASIL-mutant Notch3 is able to aggregate *in vitro*. [71] Furthermore, we revealed that mutant Notch3 is able to sequester wt Notch3 as well as other proteins such as thrombospondin 2 (TSP-2) into the aggregates. Another study identified latent TGF-β binding protein (LTBP-1) as major interactor of mutant Notch3, once more arguing for a neomorphic effect of the Notch3 mutations. [34] Our finding that Notch3 aggregates can be dissolved in SDS-buffer only in presence of a reducing agent such as β-mercaptoethanol (β-ME), substantiated the existing data that mutant Notch3 aggregates are cross-linked by disulfide bonds. [71,72]

1.3.3 Atypical (cysteine-sparing) Notch3 mutations

Although typical CADASIL mutations alter the number of cysteines, over the last years different mutations not involving a cysteine residue have been reported to be associated with a CADASIL-like phenotype. Their relevance for the disease progress is still controversially discussed. So far it is not clear, whether these mutations are rare missense

polymorphisms or deleterious variants.[73] Due to the lack of appropriate approaches the pathogenicity of these variants could so far not be studied experimentally.

At the beginning of this thesis eight mutations that do not alter the number of cysteines had been reported, five of them located within the EGF repeats 1-5 (Table 1.2).[74–85] The mutation R61W which substitutes a basic amino acid with an aromatic amino acid was found in an American patient suspected with CADASIL. In this case *NOTCH3* exons 1-33 were sequenced and skin biopsies displayed GOM deposits.[82] The R75P mutation introducing a bulky proline instead of the basic arginine residue is the best characterized cysteine-sparing mutation so far occurring in Japanese, Chinese and Korean patients.[77–79,83,84] Depending on the case report nearly all relevant exons were sequenced and also skin biopsies indicated the presence of classical GOM deposits. In addition to these point mutations the in-frame deletion ΔA88-G91 has been reported which results in the loss of four consecutive amino acids altering the distance between two cysteines to just one residue. This mutation was found in an Italian family, screened for exons 2-23 and positive for GOM deposits.[76] The conservative mutation R213K substituting one basic amino acid with another was found in a Japanese autopsy case without information about sequenced exons or GOM deposits.[74,75] The mutations T577A and S978R were published only in a short note without information about sequenced exons and presence of GOM.[80] The mutation A1020P on the other hand was examined in more detail.[81] Exons 2-24 were sequenced and one patient also was diagnosed positive for Notch3 deposits by skin biopsy and immunostaining. The other patient however had normal skin biopsy findings. The mutation D80G with an amino acid exchange from acidic to aliphatic was identified in one of our own CADASIL families.[85] Sequencing the complete *NOTCH3* gene revealed four family members with a typical CADASIL clinical and imaging phenotype. Skin biopsy, however, revealed GOM deposits in only one patient. The mutation was absent in a healthy sibling.

The pathomechanism underlying cysteine-sparing mutations is unknown and their clinical relevance intensively discussed. One possibility is that they also lead to protein misfolding due to steric hindrances or polarity change of amino acids. This could also result in aberrant disulfide bonding or may promote the aggregation process via another unknown mechanism.

Table 1.2: Features of cysteine-sparing mutations and polymorphisms of Notch3 analyzed in this study. NA: not available ; ESP: exome sequencing project

Mutation	Substitution	Patients (families)	Sequenced exons	GOM (biopsies)	Comments	Reference
R61W	basic → aromatic	2 (1)	1-33	+		Brass et al. [82]
			2-23		rare polymorphism without GOMs	Tournier-Lasserve, unpublished data
					0.05 % allele frequency	ESP (European American)
R75P	basic → structural	16 (4)	3-4, 11,18	+		Kim et al. [77]
	disruptor	4 (2)	1-33	+		Mizuno et al. [79]
		1 (1)	2-24	+		Wang et al. [83]
		2 (2)	NA	NA	no MRI data	Choi et al. [78]
		6 (NA)	2-11,14,15,18-23,25	NA		Kim et al. [84]
D80G	acidic → aliphatic	2 (1)	1-33	+		Wollenweber et al. [85]
ΔA88-G91	deletion	2 (1)	2-23	+		Mazzei et al. [76]
R113Q	basic → amide				0.07 % allele frequency	ESP (European American)
H170R	basic → basic				0.3 % allele frequency	ESP (European American)
		1 (1)	2-23		rare polymorphism (1 out of 684 pat.)	Ungaro et al. [86]
		3 (NA)	2-6, 8, 11, 14, 18-19, 22-23	NA		Ampuero et al. [87]
G179V	aliphatic → aliphatic				0.18 % allele frequency	ESP (Black American)
R213K	basic → basic	1 (1)	2-33	+	reexamination of an autopsy case	Santa et al. [75]
		1 (1)	NA	NA		Uchino et al. [74]

1.4 Confocal single molecule spectroscopy

While many studies in the past have focused on the description of Notch3-ECD aggregates *in vivo*, little is known about the molecular mechanisms underlying their formation. This is primarily due to the lack of *in vitro* aggregation assays and methods to monitor it. Confocal single molecule spectroscopy techniques such as fluorescence correlation spectroscopy (FCS) were originally developed to study the behavior of single fluorescent molecules in solution. FCS can detect extremely low concentrated particle diffusing in aqueous buffer solution with a stationary focus. This fluctuation is reflected by the fluorescent emission of the molecules detected by avalanche photo diodes (APDs). The signal can be quantified by mathematical procedures such as autocorrelation analysis. By this means different parameters of the investigated particles such as specific fluorescent intensity, local concentration, lateral diffusion coefficient and thus size of the molecule can be determined. The theoretical concept of FCS was described in Schwille[88] and Schwille et al.[89]. In biomedicine it was applied to the analysis of molecules at submicromolar concentrations and used to examine the aggregation behavior of proteins such as α-synuclein (α-syn) and prion protein (PrP) *in vitro* and to learn more about the molecular origins of neurodegenerative diseases associated with mutations in these proteins. Thus, FCS appeared to be highly suited to study the features of the Notch3 aggregation process.

1.4.1 Scanning for intensely fluorescent targets (SIFT)

In FCS diffusion time becomes a limiting factor as soon as large molecule at sub-picomolar concentrations have to be detected. The probability of a molecule passing through the focus within a reasonable measurement time decreases the larger it is and thus the slower it diffuses. Thus, SIFT was developed which uses a scanning procedure instead of a stationary focus to detect large molecules with low diffusion times. A mobile focus is used that scans in a meander-like fashion through the sample volume (Figure 1.8). The scanning allows a molecule detection in a femtomolar range, thus increasing the number of particles passing through the focus by about 100-fold compared to the static measurements. As the dwell time of a molecule in the focus is no longer determined by the diffusion time but by the scanning speed of the laser beam , large targets can be recognized by intensity analysis. With the intensity distribution the highly intensive signal of multiple labeled large target molecules can be separated from the background signal. At the same time the number of peaks should be proportional to the number of target molecules. The principle of the SIFT technique was described in Bieschke et al.[90] and Giese et al.[91].

The development of dual-color SIFT now allows a simultaneous measurement of two molecules with different fluorescent properties in the same sample. The emitted photons of the excited fluorescent dyes are collected by the same objective and passed through the first dichroic mirror, where the signal is separated from the laser beam. The following

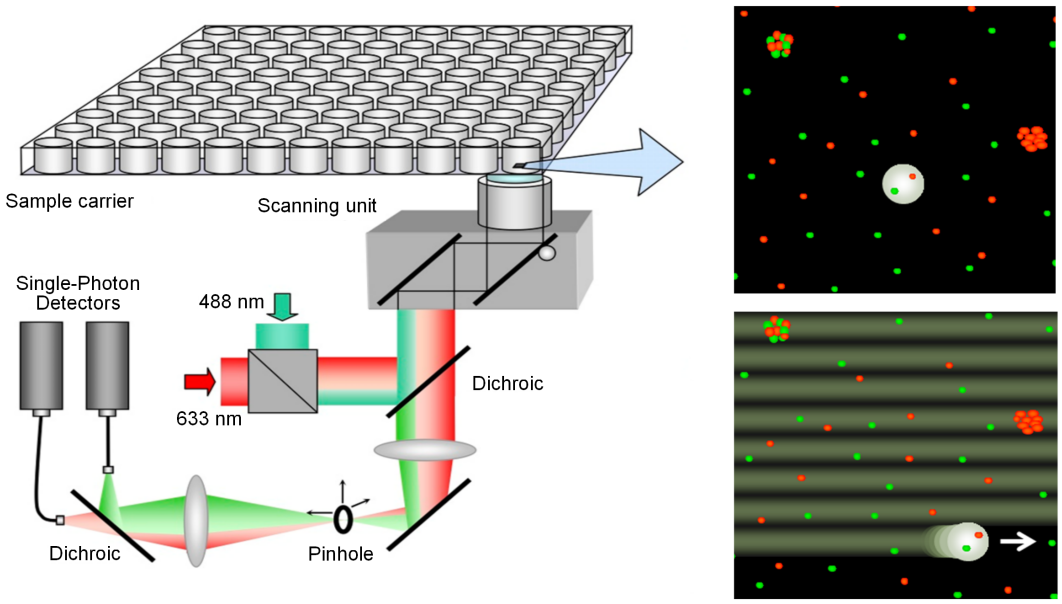

Figure 1.8: Measurement setup of the Insight II Reader. Schematic picture of a two-color FCS reader with scanning unit for SIFT measurements. Laser beam is focused through a dichroic mirror and a water immersions objective into the sample. The sample with fluorescently labeled proteins of different sizes is scanned. The emitted fluorescent light passes through the same objective and is directed by dichroic mirrors through the pinhole to the APDs.

pinhole with a diameter of 70 µm blocks any fluorescent light not originating from the focal region, thus separating the signal from unspecific background. Finally, the emission signals from the two fluorophores are separated by a second dichroic mirror and detected by two separate APDs (Figure 1.8). Thus, the signal of dual-color molecules can be detected in both detection channels and analyzed in a two-dimensional histogram (Figure 1.9). This enables for example the separation of the dual-color signal of the target aggregates from any mono-color signals generated during purification and labeling procedures. On the other hand, interaction behavior of two different target molecules can be studied as well.

1.4.2 Analysis of Notch3 aggregation by SIFT

SIFT was successfully used to study the aggregation process of α-syn and PrP.[92] We therefore have applied it to study the aggregation behavior of Notch3 mutants identified in CADASIL patients. First attempts with cell lysates containing overexpressed Notch3-ECD indicated enhanced multimer formation of CADASIL-mutated constructs, however multimer formation could be also detected in wt Notch3-ECD.[70] We improved the assay by using purified Notch3 protein. To ensure correct folding and posttranslational modification, we obtained it from the supernatant of transiently transfected cultured cells. Since secretion of the complete Notch3-ECD is very inefficient due to complicated folding of its 34 EGF-like domains, we used a Notch3 fragment containing EGF-like repeats

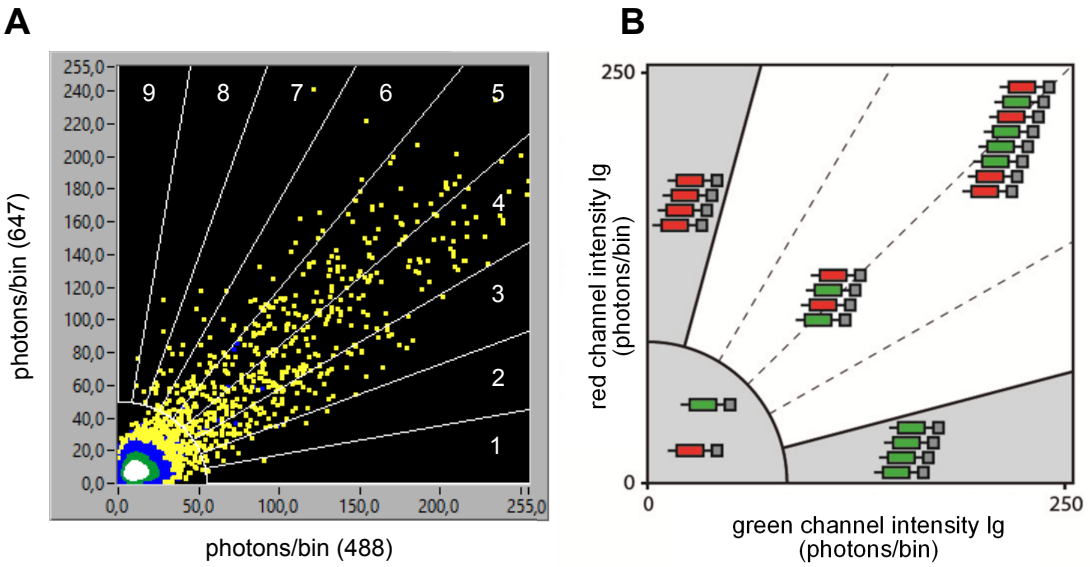

Figure 1.9: SIFT intensity histogram. A) 2D histogram depicts the intensity of the photon counts in the green (Alexa 488) channel (x-axis) and the red (Alexa 647) channel (y-axis). The plot is divided into 9 equal segments. Low intensity signals are excluded by setting a threshold. B) Distribution of detected proteins in the 2D histogram. Monomers are located in the lower left corner. Higher order multimers of one color are aligned along the axes and dual-color multimers are located in the white area of the histogram.

$1-5$ (Notch3-EGF$_{1-5}$), the mutational hotspot harbouring 70 % of all known CADASIL mutations[53], which is secreted very efficiently.[71] Purified His-tagged Notch3-EGF$_{1-5}$ was obtained by metal ion affinity chromatography. With the purified protein we could show that CADASIL-mutant but not wt Notch3-EGF$_{1-5}$ spontaneously form multimers. Furthermore, experiments with β-ME and bismaleimide, a crosslinker specific for sulfhydryl groups, could demonstrate the involvement of cysteine residues and thus sulfhydryl groups in the aggregate formation. We could further show that mutant Notch3-EGF$_{1-5}$ spontaneously co-aggregates with TSP-2 as well as with LTBP-1.[34,71]

1.5 Aim of this work

The aggregation of the Notch3-ECD triggered by mutations is considered the key determinant of CADASIL pathogenesis and our establishment of an *in vitro* aggregation assay has turned out to represent an important advancement in the field. The procedure used so far for the purification of Notch3 fragments required for this assay relies on a metal ion affinity matrix binding to a His-tag and the elution by EDTA. The drawbacks of this method were the tedious removal of the EDTA, the presence of the His-tag on the purified protein and the suboptimal purity. Therefore, the first aim of this thesis was to improve the protein purification procedure by establishing a new system based on the HaloTag technology which allows covalent binding of the target protein to a purification matrix and subsequent proteolytic removal of the affinity tag.

The second goal was to apply the improved method to the analysis of the aggregation behavior of cysteine-sparing Notch3 variants. Some of them have been reported to cause CADASIL, but their pathogenic potential and clinical relevance is currently under debate.

The third goal of this thesis was to identify small molecule aggregation inhibitors. A number of synthetic and natural compounds were screened in the *in vitro* assay. Some of the substances with significant efficiency were further tested in a cellular assay using mouse embryonic fibroblasts (MEFs) transfected with Notch3-EGF$_{1-5}$ fragments.

2 Results

2.1 HaloTag-mediated purification of Notch3 fragments

Using SIFT we have developed an *in vitro* assay to study details of the aggregation process triggered by mutations in the Notch3-ECD (see section 1.4). This assay relies on the availability of highly purified and correctly folded proteins which can be obtained from conditioned supernatant of transiently transfected cultured cells. Since our earlier studies had revealed inefficient secretion of the full ECD or versions containing the first 10 or 15 EGF-like repeats, we had chosen a Notch3-ECD fragment consisting of the signal peptide and EGF-like repeats $1-5$ encompassing the mutational hotspot of CADASIL (Figure 1.6).[71] Purification from cell culture supernatants had so far been performed by a metal ion affinity purification approach making use of the C-terminal His tag attached to Notch3-EGF_{1-5}. However, this approach suffered from several drawbacks including elution from the matrix by EDTA (which had to be removed by an additional dialysis step), suboptimal purity and yield and the inability to remove the affinity tag. To overcome these limitations, we investigated whether HaloTag-mediated purification[93] could be used as alternative procedure.

2.1.1 The Halo affinity tag

The HaloTag protein is a mutated form of the dhaA hydrolase that can form a stable covalent bond with immobilized chloroalkane substrates enabling an efficient and specific capture of proteins expressed as HaloTag fusion proteins.[93] To examine its suitability for purifying Notch3-EGF_{1-5} fragments we fused it to the C-terminus of our target protein and used it for affinity purification (Figure 2.1). Conditioned medium was dialyzed and secreted fusion protein was bound covalently to the HaloLink resin. In contrast to metal affinity matrices the HaloLink resin shows low nonspecific binding and impurities can be efficiently removed by stringent washing. The target protein is released by tobacco etch virus (TEV) protease, recognizing a specific cleavage site located between both proteins, while the HaloTag protein remains bound to the resin. Subsequently, the TEV protease is removed via its His-tag using HisLink resin yielding highly purified tag-free target protein.

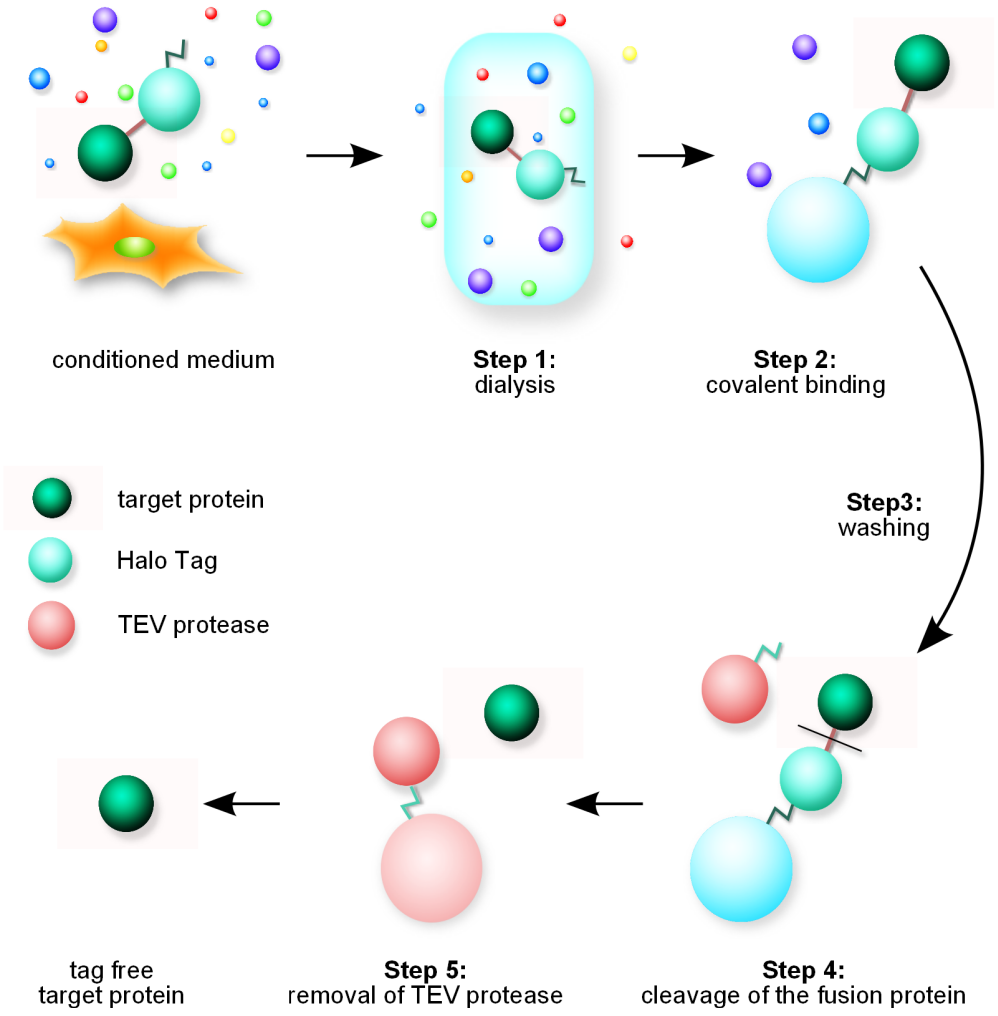

Figure 2.1: Scheme of the HaloTag purification. Conditioned medium from HEK293E cells transiently transfected with the HaloTag fusion protein was collected and dialyzed. The fusion protein binds covalently to HaloLink resin via the HaloTag. After stringent washing the target protein was released from the HaloTag bound to the resin by cleaving of TEV protease. TEV protease was removed by binding to HisLink resin via its His-tag. The tag-free target protein was recovered in PBS.

2.1.2 Overexpression and secretion of Notch3-EGF$_{1-5}$

Since the molecular size of the HaloTag protein (33 kDa) differs substantially from the previously used myc-His tag, expression and secretion conditions had to be reestablished. We, therefore tested two different expression vector systems: one using the standard vector available with the HaloTag purification system (pFC14A) and one using the previously used pTT5 vector. After cloning the Notch3-EGF$_{1-5}$ insert into the pFC14A vector, it is expressed from the cytomegalovirus (CMV) promotor as fusion protein with a C-

terminal HaloTag. For expression from the pTT5 vector which contains an improved CMV expression cassette optimized for protein expression in HEK293E cells[94] we replaced the previously used myc-His tag with the HaloTag sequence (Figure 2.2).

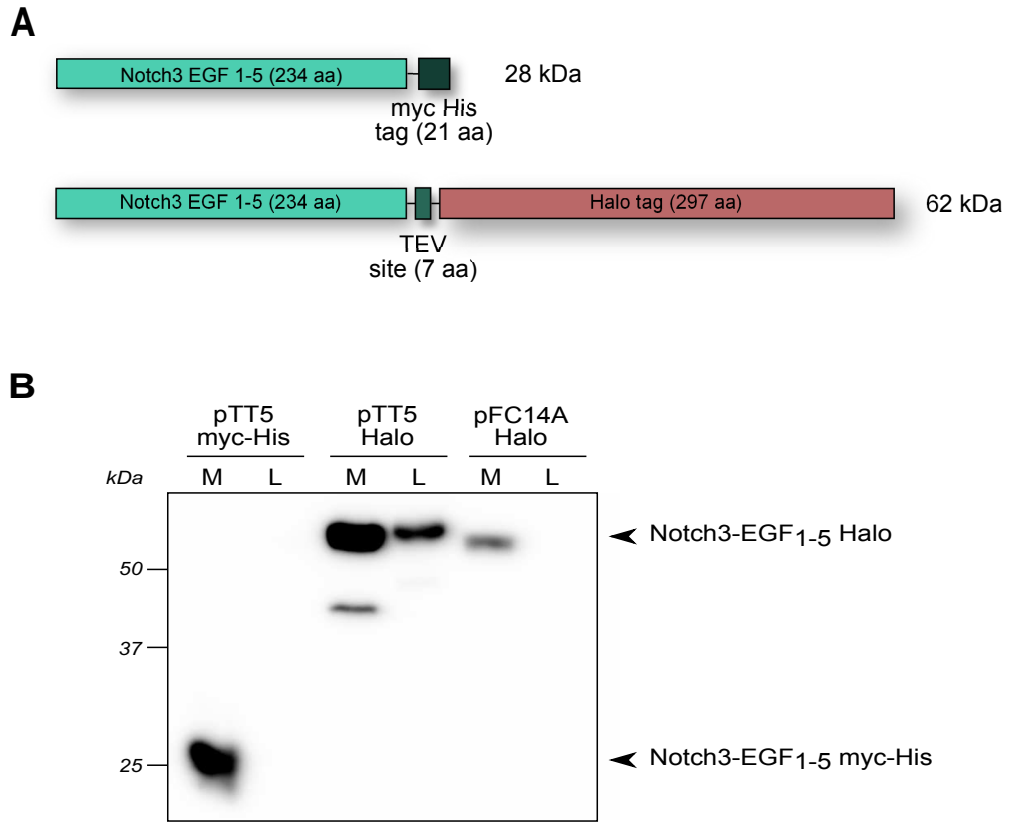

Figure 2.2: Expression analysis of wt Notch3-EGF$_{1-5}$. A) Schematic illustration of both Notch3-EGF$_{1-5}$ fusion proteins with myc-His tag and HaloTag respectively. Notch3-EGF$_{1-5}$ myc-His contains the myc tag of 15 amino acids with six histidines fused to the C-terminus of Notch3-EGF$_{1-5}$. Notch3-EGF$_{1-5}$ Halo contains a HaloTag linked with a TEV recognition site to the C-terminus of Notch3-EGF$_{1-5}$. B) HEK293E cells were transiently transfected with the original myc-His-tagged version in the pTT5 vector and the two Halo-tagged versions in the pTT5 and pFC14A vector. Cells were harvested after three days. Amount of expressed Notch3-EGF$_{1-5}$ in conditioned medium (M) and cell lysate (L) is determined by Western Blotting under reducing conditions. 2 µg of cellular protein (1.25 % of total) and 12.5 µl of media (1.25 % of total) were loaded. Proteins were detected with monoclonal anti-Notch3 antibody 3G6.

In transient transfection experiments in HEK293E cells, cellular expression and secretion efficiency of the HaloTag fusion proteins were analyzed in comparison to the previously used myc-His tag fusion protein. While Notch3-EGF$_{1-5}$ expressed from the pFC15A vector was detected in significantly lower amounts in the medium fraction, production from the pTT5 vector was comparable to myc-His tagged Notch3-EGF$_{1-5}$ (Figure 2.2 B). Moreover, a large fraction of the HaloTag fusion protein was secreted, although a residual signal was observed in the cellular fraction, in contrast to the myc-His tagged protein. This result

demonstrated that the combination of pTT5 vector and HaloTag yields protein levels in the medium sufficiently high for purification purposes.

2.1.3 Optimization of the purification procedure

We next analyzed the efficiency of Notch3-EGF$_{1-5}$ Halo binding to the HaloLink resin by varying several parameters: (1) incubation time (1 and 16 h); (2) amount of resin used in the binding step; (3) addition of glycerol to reduce hydrophobic interactions and (4) addition of β-ME to test the influence of Notch3 structure on binding. Although the addition of β-ME breaks the structure of the protein and is therefore not suitable for purification, we tested its effect to exclude possible structure related hindrances for correct binding. Figure 2.3 A shows the flowthroughs after HaloLink resin coupling representing the amounts of unbound protein. Extending the coupling time had by far the strongest effect while increasing amounts of resin and the addition of glycerol had only little impact. β-ME treatment improved the binding suggesting an influence of Notch3 structure, however, this caveat could be overcome by the increased coupling time.

We then performed a complete small-scale purification procedure to estimate the ultimate yield and quality of purified Notch3-EGF$_{1-5}$ Halo. Gel electrophoresis and silver staining of the material after TEV protease-mediated cleavage and its removal revealed the presence of a single band of 25 kDa corresponding to the calculated size of Notch3-EGF$_{1-5}$. No degradation products were detected in significant amounts (Figure 2.3 B).

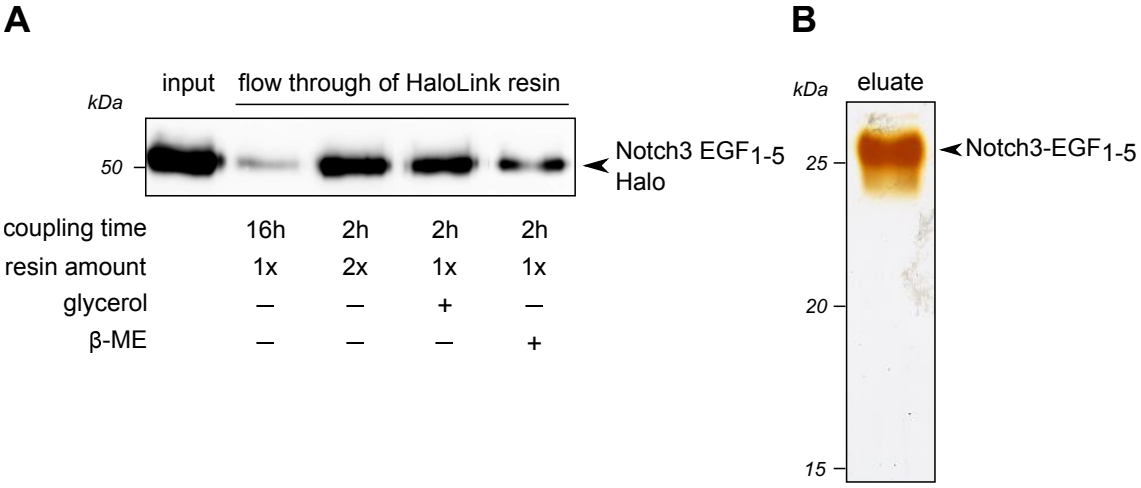

Figure 2.3: Optimization of Notch3-EGF$_{1-5}$ purification. A) Immunoblot with anti-Notch3 antibody 3G6 of flowthroughs after the HaloLink binding step. HEK293E cells were transfected with Notch3-EGF$_{1-5}$ Halo and medium was collected after five days. Binding efficiency of different conditions was compared to conditioned medium before binding (input). Coupling time was varied from two hours to 16 hours. Resin amount was doubled in one sample and influence on binding of 5 % glycerol and 14 mM β-ME was checked. B) Silver staining of a 15 % SDS-PAGE of eluted Notch3-EGF$_{1-5}$ shows no degraded low-size fragments.

2.1.4 Large scale purification

After optimizing the purification protocol a large-scale purification of wt Notch3-EGF$_{1-5}$ was carried out. As established previously with the metal resin based purification system, medium was collected from four 500 cm^2 flasks of HEK293E cells transiently transfected with Notch3-EGF$_{1-5}$ Halo after five days. Each purification step was controlled by silver staining (Figure 2.4 A upper panel) and Western blotting (Figure 2.4 A lower panel).

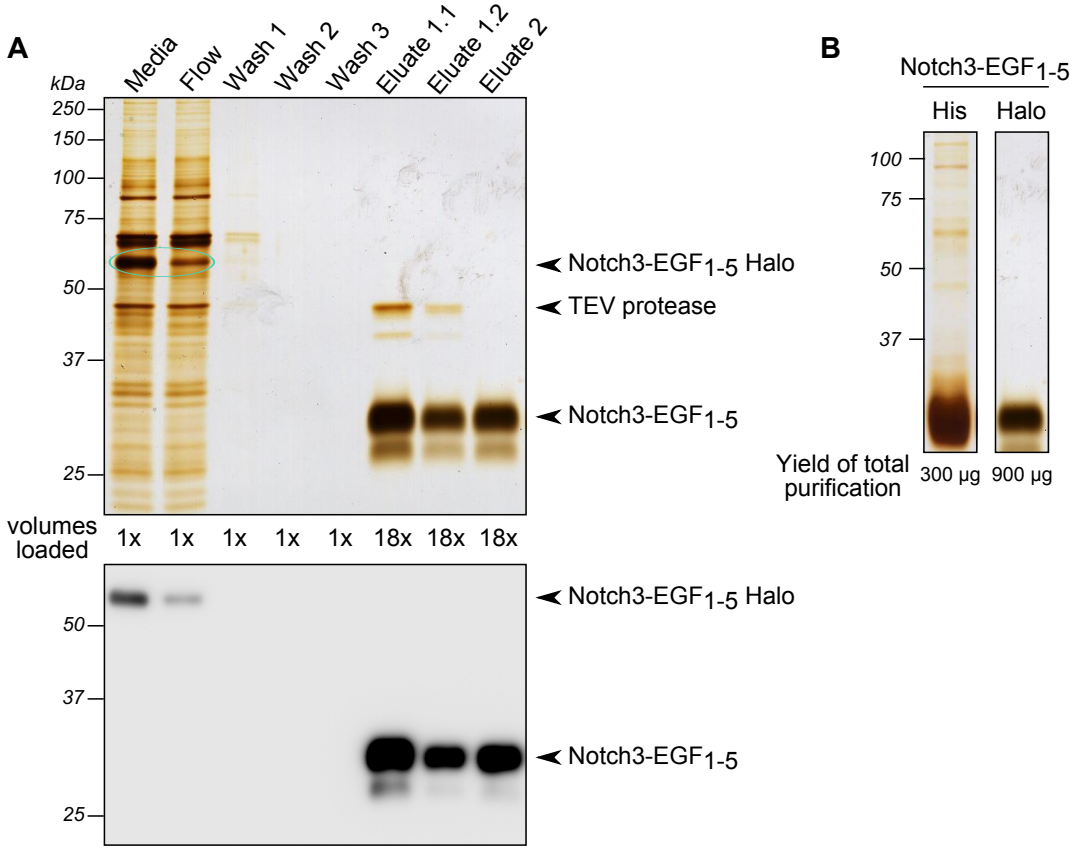

Figure 2.4: Large-scale purification of Notch3-EGF$_{1-5}$. A) Silver staining and Western blotting of a representative purification of wt Notch3-EGF$_{1-5}$ with the HaloTag purification system. Media: Conditioned medium of transiently transfected HEK293E cells, Flow: Flow-through after binding to HaloLink Resin, Eluate 1.1 and 1.2: fractions after TEV protease cleavage, Eluate 2: pooled eluate 1.1 and 1.2 after removal of TEV protease. Of note, the ratio of loaded sample is, due to the different volumes 18 times higher in the elution fractions compared to the media and flow fraction. Proteins on Western blot were analyzed with anti-Notch3 antibody 3G6. B) Comparison of His-tag and HaloTag purification concerning purity determined by silver staining.

Silver staining of the starting material revealed two prominent bands, one of $\sim$ 60 kDa representing the HaloTag fusion protein (Figure 2.4 A upper panel). The comparison of the starting material (Media) and the flow through of the HaloLink resin (Flow) shows a considerable reduction of the 60 kDa band indicating an effective binding of the fusion protein. Immunoblotting confirmed that this band represents Notch3-EGF$_{1-5}$ Halo.

Stringent washing of the resin removed traces of remaining protein already in the first washing step (Wash 1). Addition of TEV protease led to the release of Notch3-EGF_{1-5} from the HaloLink (Eluate 1.1). Residual Notch3-EGF_{1-5} was recovered from the resin by washing the beads again with buffer (Eluate 1.2). TEV protease ($\sim$ 45 kDa) was efficiently removed from the pooled eluate fractions by binding to HisLink resin. In figure 2.4 B the increased purity of Notch3-EGF_{1-5} purified by the Halo technology in comparison to Notch3-EGF_{1-5} His is demonstrated. In addition, the yield of the purified protein was improved by a factor of three resulting in 900 µg of highly purified tag-free wt Notch3-EGF_{1-5}. In parallel, the mutant protein C183R was purified with a yield of 560 µg.

2.1.5 Multimer formation of purified tag-free Notch3-EGF_{1-5}

To analyze the multimerization behavior of tag-free Notch3 fragments purified via the Halo technology, aliquots of the pure protein fractions of wt Notch3-EGF_{1-5} and the C183R mutant were each labeled over night (o/n) with a 3-fold molar excess of $Alexa^{488}$ (green) or $Alexa^{647}$ (red) succinimidylester and unbound dye was removed by desalting columns. Proteins were aliquoted, frozen in liquid nitrogen and stored at $-80°C$. For each experiment a new aliquot was thawed and unspecific multimers pre-formed due to the freezing procedure were removed by ultracentrifugation. A 1:1 mixture of green and red labeled protein for each construct was incubated for five days at 37°C on a rotary shaker. SIFT analysis was performed at baseline, three days and five days (Figure 2.5). At baseline none of the constructs showed any high-intensity signal indicating successful removal of pre-formed multimers. During incubation the number of dual-color high intensity signals increased dramatically for the mutant but not for the wt protein. Quantification of seven independent experiments revealed that this effect is robust and reproducible. This demonstrated a differential multimerization behavior similar to that observed previously for His-tagged Notch3-EGF_{1-5}. We concluded that tag-free Notch3 fragments purified by the HaloTag system are suitable for *in vitro* aggregation analysis.

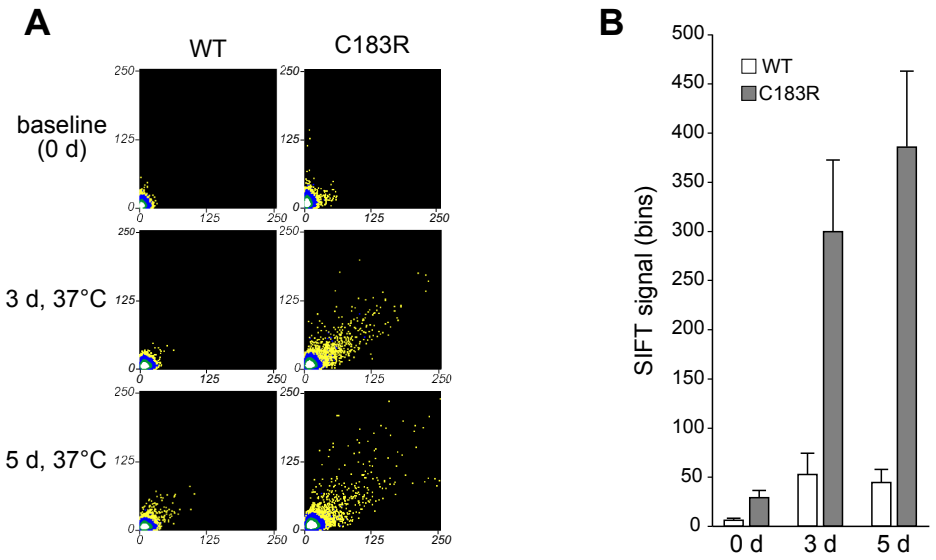

Figure 2.5: Spontaneous multimerization of tag-free mutant Notch3-EGF$_{1-5}$. A) SIFT analysis reveals dual-color high intensity signal of mutant Notch3-EGF after three and five days indicating spontaneous *de novo* multimer formation of mutant protein, whereas wt remains in the monomer form depicted as low intensity signal in the left lower corner of the histogram. B) Quantification of dual-color high-intensity SIFT signals from wt and mutant. Mean + standard error of the mean (SEM) of seven independent experiments.

2.2 Aggregation analysis of cysteine-sparing Notch3 mutations

The overwhelming majority of Notch3 mutations associated with CADASIL lead to an odd number of cysteine residues in one of the EGF-like repeats of the Notch3-ECD. However, over the last years several cysteine-sparing mutations have been reported to cause a CADASIL-like phenotype and their relevance for the disease is controversially discussed (see section 1.3.3). These findings are difficult to reconcile with the currently favored pathomechanism involving disulfide-mediated Notch3-ECD aggregation.

To gain insight into the possible pathogenicity of cysteine-sparing mutations we set out to investigate their multimerization behavior in our SIFT assay. Since the Notch3 fragments used in this assay comprises only EGF-like repeats $1-5$ we focused on mutations within the first 4 exons (Table 1.2). Four cysteine-sparing mutations within this region (R61W, R75P, ΔA88-G91 and R213K) had been published[74–79,82,83], a fifth one (D80G) had been identified in one of our own patients. As positive controls, we used the well-described mutations R133C and C183R, as well as the C212Y mutation described in Bentley et al.[95]. As negative controls besides wt we chose three single nucleotide polymorphisms (SNPs) from the exome sequencing project (ESP) (R113Q, H170R and G179V) with an allele frequency of at least 0.1% which had so far not been associated with CADASIL (Table 1.2). Although the mutation H170R had been described as disease causing by Ampuero et al.[87], there was evidence that it can be considered as a rare polymorphism, since

no clinical details of the patient were presented and it emerged as polymorphism in our database research. Thus, this variant was classified as polymorphism.

2.2.1 Cysteine-sparing mutants are efficiently expressed and secreted

All Notch3 mutant constructs were generated by mutagenesis from the pTT5 Notch3-EGF_{1-5} Halo plasmid and verified by sequencing. Their expression and secretion efficiencies after transient transfection into HEK293E cells were analyzed after three days by Western blotting. Equal protein amounts were loaded and medium volume was adjusted to the corresponding lysate. Detection with an anti-Notch3 antibody revealed cellular expression levels as well as secretion efficiencies in the medium comparable to wt Notch3 demonstrating the suitability of the mutant fragments for large-scale purification (Figure 2.6).

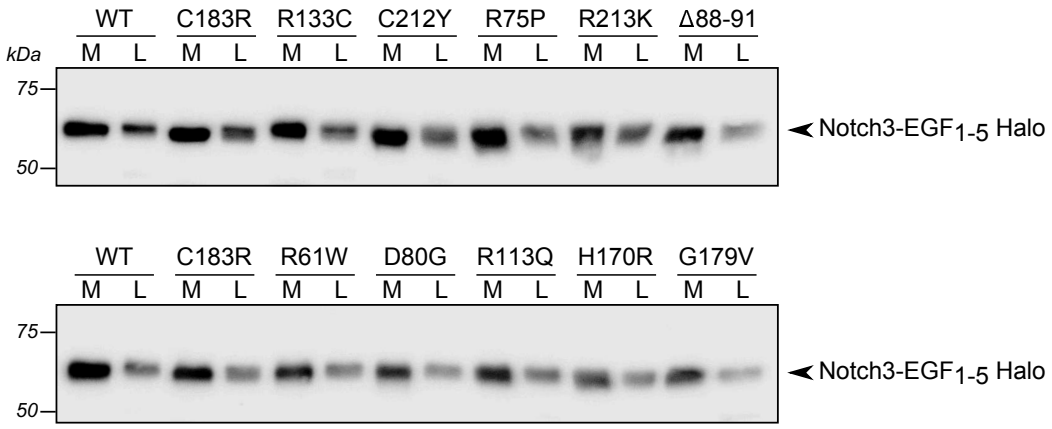

Figure 2.6: Expression analysis of different Notch3 variants. HEK293E cells were transiently transfected with Notch3-EGF_{1-5} constructs bearing different amino acid changes or the wt form. Medium and cells were harvested three days after transfection. Protein concentration of cell lysates was determined and adjusted. Volume of conditioned medium was adjusted to the corresponding cell lysate. Amount of expressed Notch3-EGF_{1-5} in conditioned medium (M) and cell lysate (L) under reducing conditions was determined by immunoblotting. Transfected wt and C183R samples served as control on both blots. Proteins were detected using anti-Notch3 antibody 3G6.

Notch3-EGF$_{1-5}$ fragments carrying various polymorphisms or mutations were purified in large scale using the HaloTag technology. Purity and yield of most variants was comparable to wt Notch3-EGF$_{1-5}$, except for the R133C and C183R mutations having lower yields (Figure 2.7).

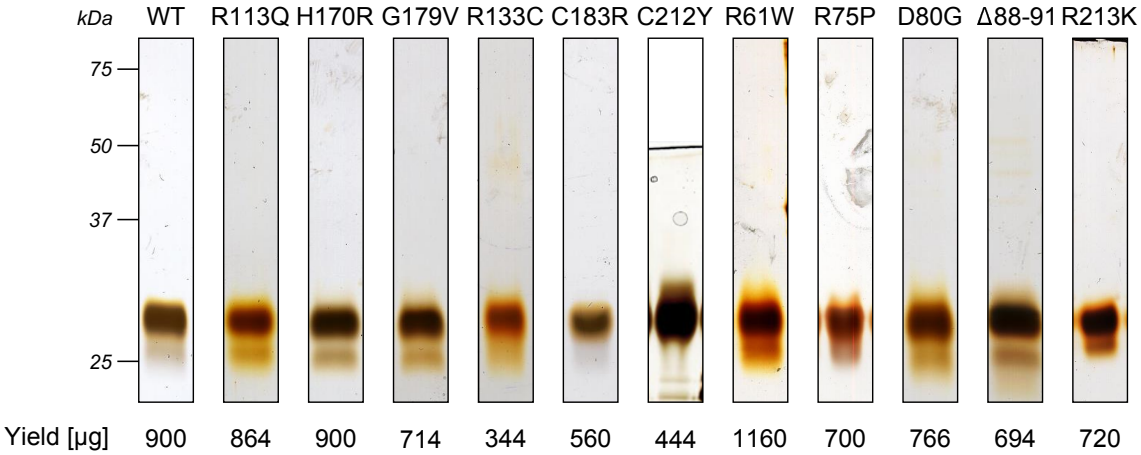

Figure 2.7: Purity and yield of all purified Notch3-EGF$_{1-5}$ mutation variants. Silver staining of final eluates from purified mutant Notch3-EGF$_{1-5}$ constructs including wt. All purified mutant proteins showed high purity comparable to wt. Final protein yield was determined by protein concentration measurements. Amount of protein for most mutants obtained in one purification was comparable to wt, only the R133C and C183R mutation showed reduced yields.

2.2.2 Cysteine-sparing mutants show differential aggregation behavior

Purified Notch3-EGF$_{1-5}$ fragments containing classical CADASIL mutants, cysteine-sparing mutants and polymorphisms were fluorescently labeled and their multimerization potential was analyzed by SIFT at baseline, three and five days. Figures 2.8 and 2.9 show the raw data of representative experiments and Figure 2.10 shows the quantification of six independent experiments. At baseline, high-intensity signals were low for all variants examined, demonstrating the absence of preformed aggregates. In the polymorphism group none of the variants showed a stronger aggregation tendency than the wt protein suggesting no aggregation potential. In contrast, all three cysteine mutants displayed a significant increase in high-intensity signals after three and five days of incubation demonstrating their well-established aggregation potential (Figure 2.8).

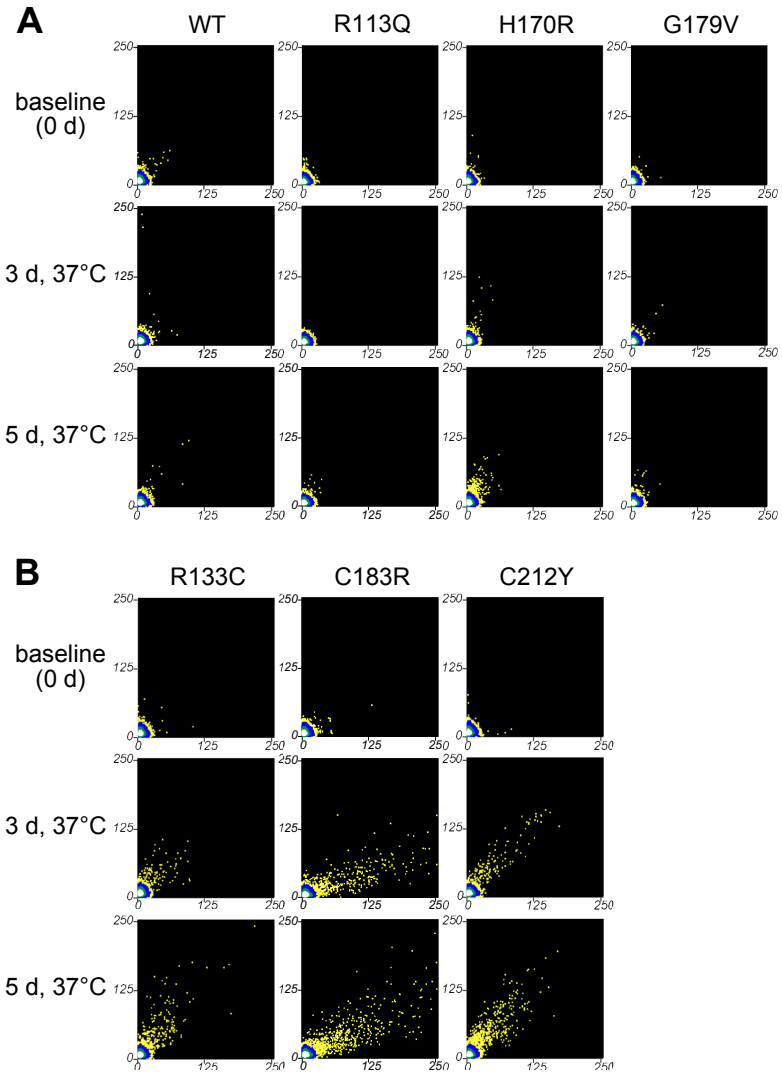

Figure 2.8: Aggregation assay with polymorphisms and canonical cysteine-affecting mutations of Notch3-EGF$_{1-5}$. Representative 2D histogram plots show multimerization for A) wt and polymorphisms and B) cysteine-affecting mutants at baseline and after incubation for three and five days at 37°C. Polymorphisms show no or only low aggregation potential comparable to wt. In contrast, the cysteine mutants exhibit an increased multimer signal after incubation.

For the various cysteine-sparing variants differing results were obtained. R213K, the only reported cysteine-sparing mutation with a conservative exchange of amino acids (basic → basic) showed the lowest multimerization tendency suggesting that it in fact represents a polymorphism. For R61W, an increase was observed after three and five days but total signal levels were not higher than with wt protein or the H170R polymorphism (Figure 2.9). However, the three variants R75P, D80G and ΔA88-G91 showed a significant increase which was as strong as with the classical mutants (Figure 2.10).

This data indicate that indeed some cysteine-sparing mutations in Notch3-EGF$_{1-5}$ favor the aggregation process of the protein *in vitro*. The potential consequences of our findings are discussed in section 3.1.

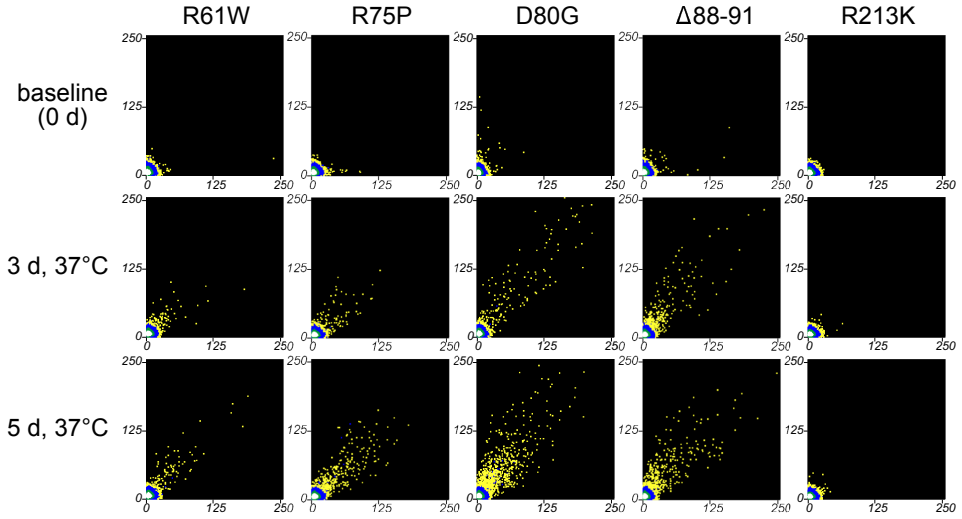

Figure 2.9: Aggregation assay with cysteine-sparing Notch3-EGF$_{1-5}$. Representative 2D histogram plots of cysteine-sparing Notch3-EGF$_{1-5}$ mutations show mixed results. While R75P, D80G and Δ88-91 show after incubation multimer signals similar to classical cysteine mutations, the aggregation potential of R61W and R213K is as low as in wt and polymorphisms.

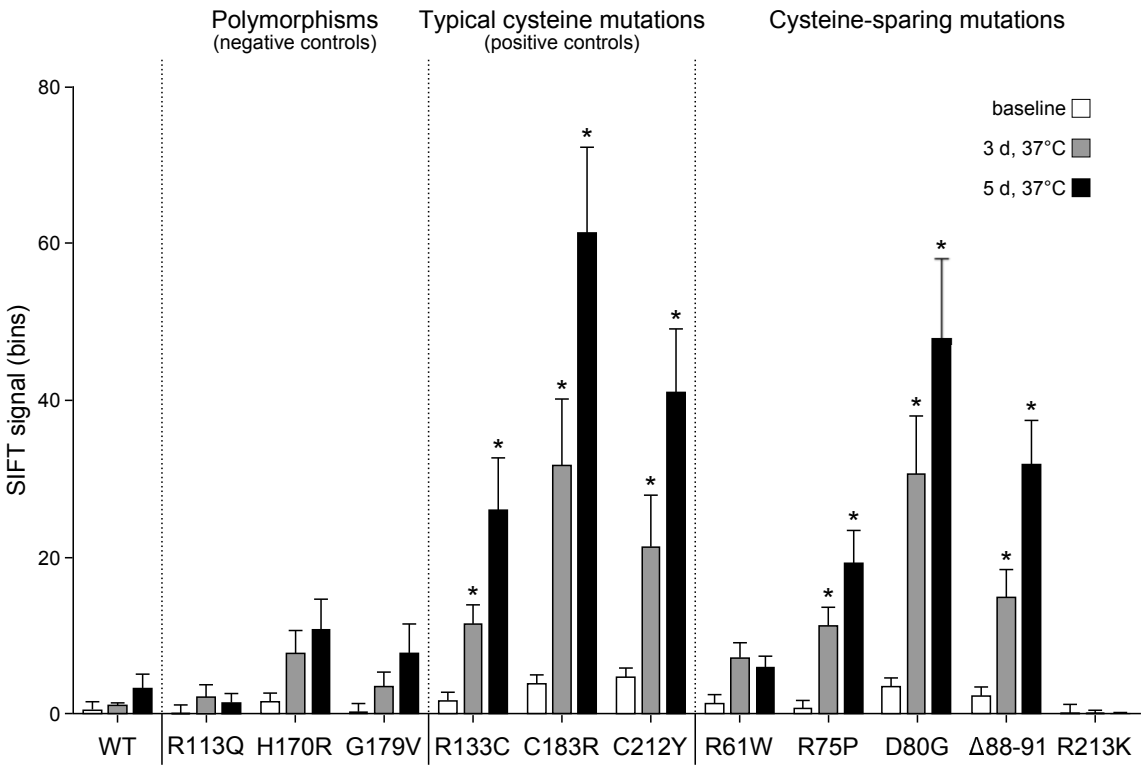

Figure 2.10: Analysis of spontaneous *in vitro* multimerization. The quantification of dual-color high-intensity signals from SIFT analysis shows the mean + SEM of six independent experiments. After incubation, the cysteine-affecting mutants show a higher multimer signal compared to wt and therefore serve as positive control group. This increase is mostly absent in the polymorphisms serving as negative control group. Results from the cysteine-sparing group are variable with three mutations having a significant increase in multimer signal after incubation but two with low or completely without multimer signal. Group statistics compared with wt at the same time point; * $p<0.05$ (post hoc Wilcoxon signed-rank sum test with false discovery rate correction).

2.3 Identification of Notch3 aggregation inhibitors

2.3.1 Synthetic small-molecule compounds

To date, there is no cure for CADASIL. Since the aggregation of Notch3 plays a key role in the pathogenesis of the disease, inhibiting or modulating this process would serve as a basis for a pharmacological therapy. Being able to monitor the aggregation of CADASIL-mutated Notch3 *in vitro* with our SIFT assay provides the opportunity to test small-molecule compounds for antiaggregatory activity. The potential of anti-aggregatory treatment is currently intensely investigated in several neurodegenerative diseases including prion disease and PD.[96–98] The substance class of diphenylpyrazole (DPP)-based compounds (Figure 2.11) has been shown to be effective in preventing aggregation of PrP and α-syn[98] We therefore selected 15 compounds of this class to test their efficiencies in our

Notch3 aggregation assay. Purified Notch3-EGF$_{1-5}$ fragment containing the archetypal C183R mutation (see section 2.1) was used throughout this study.

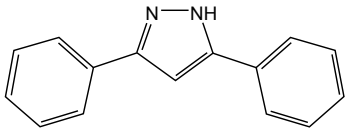

Figure 2.11: Lead structure di-phenyl-pyrazole (DPP).

All compounds were dissolved in DMSO and used at a final concentration of 10 µM in 1% DMSO as described in previous studies[98]. They were added to fluorescently labeled Notch3-EGF$_{1-5}$ C183R at baseline and the formation of multimers was measured at day three and five. DMSO alone had no significant effect on the aggregation behavior of the C183R mutant (Figure 2.12). Figure 2.13 A shows representative data of an experiment with anle138b (no inhibition), sery118 (weak inhibition) and anle138c (strong inhibition). Quantification of the data at day five from all compounds confirmed the wide range of inhibition efficiencies. While three compounds (anle138b, anle 253b and anle 137b) had no effect, six compounds (sery118, sery139, sery144, sery320a, sery95 and sery159a) resulted in a moderate but significant signal decrease and six compounds (anle138c, anle136c, sery106, anle 137c, sery166a and sery105) showed a reduction of more than 88 % (Figure 2.13 B).

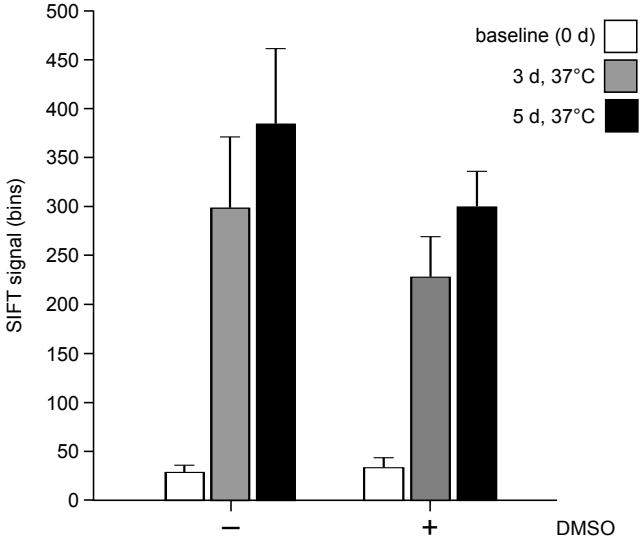

Figure 2.12: Influence of DMSO on aggregation behavior of Notch3-EGF$_{1-5}$ C183R. Quantification of SIFT signal at baseline and at day three and five after incubation at 37°C of mutant Notch3-EGF$_{1-5}$ shows normal aggregation behavior with addition of 1 % DMSO comparable to negative control. No significant difference could be detected. Mean and SEM of six independent experiments. Group statistics compared at the same time points (Mann -Whitney test).

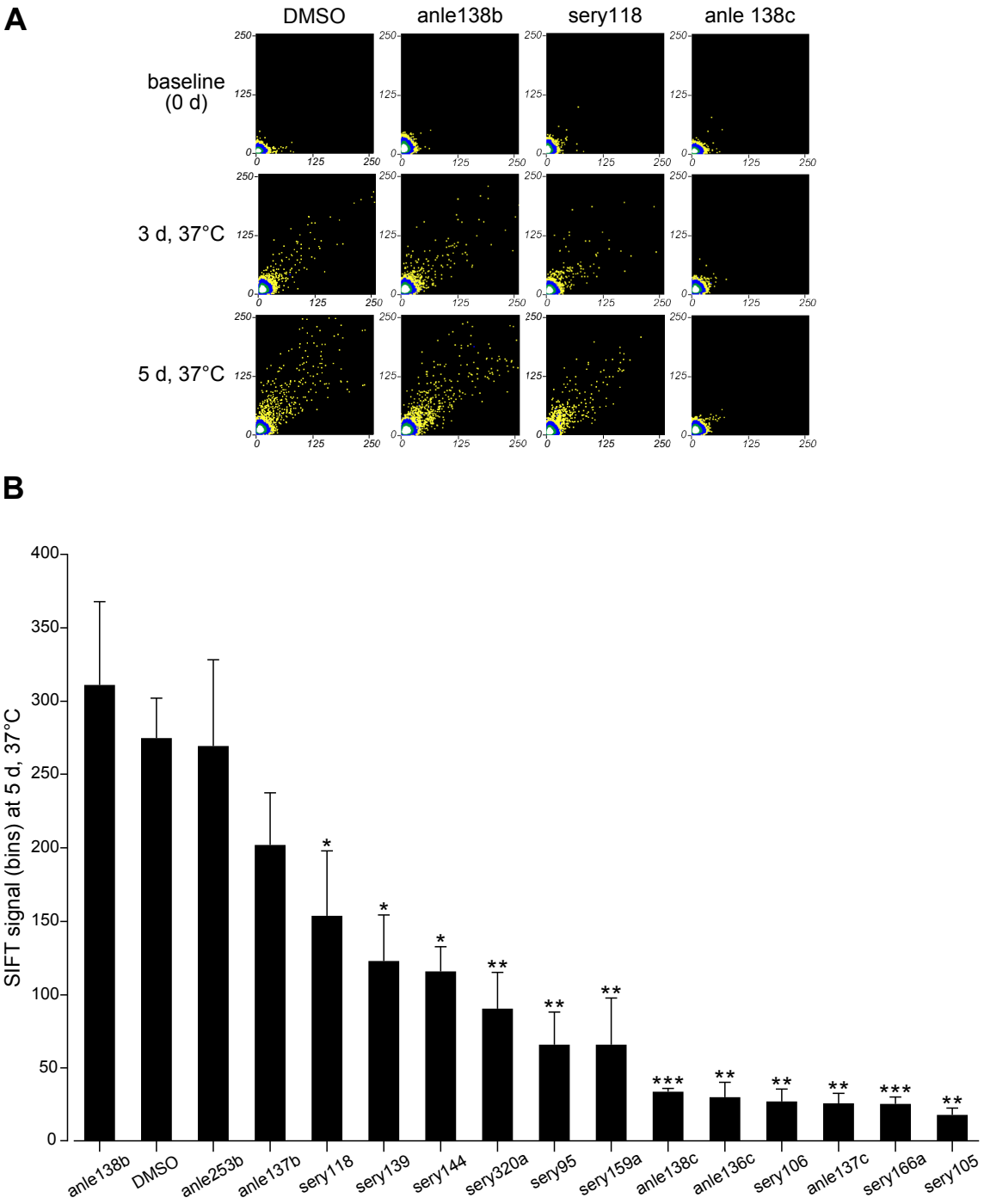

Figure 2.13: Aggregation inhibition using synthetic small molecule compounds. A) Representative 2D histogram plots show either no (anle138b), weak (sery118) or strong (anle138c) inhibition of multimer formation after addition of 10 µM compound to Notch3-EGF$_{1-5}$ C183R at baseline and incubation for five days at 37°C compared to DMSO control. B) Quantification of dual-color high-intensity SIFT signals at day five for *de novo* inhibition of mutant Notch3 aggregation using different DPP derivatives at a final concentration of 10 µM in 1 % DMSO. Mean + SEM of four independent experiments; group statistics compared with DMSO control at the same time point; * $p<0.05$; ** $p<0.01$; *** $p<0.001$ (Mann-Whitney test).

Analysis of the compound structures revealed that hydroxyl groups (OH groups) might be required for efficient inhibition of Notch3 aggregation, since only substances containing at least one OH group showed inhibitory activity (Table 2.1). Even more notable were the differential effects with pairs of highly related compounds. While anle138c (two OH groups) and anle137c (three OH groups) displayed strong anti-aggregatory activity, anle 138b and anle 137b (both without OH group) were only weakly effective. We, therefore, concluded that OH groups were essential for aggregation inhibition. However, other structural features of the compound appear to be crucial for inhibitory activity as well.

Table 2.1: Structure-activity relationship for various DPP-derivatives.

Comp.	Structure	% inh.	Comp.	Structure	% inh.
sery105	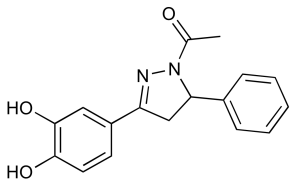	94	sery320a	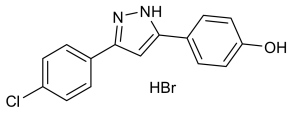	68
sery166a	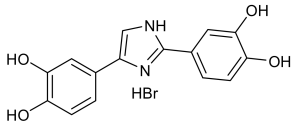	91	sery144	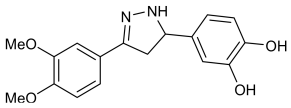	58
anle137c	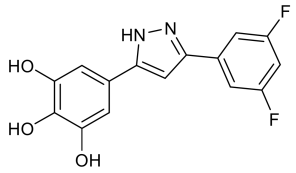	91	sery139	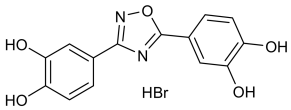	55
sery106	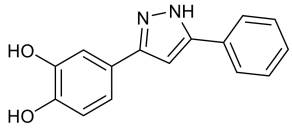	91	sery118	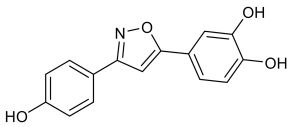	44
anle136c	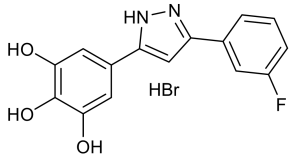	90	anle137b	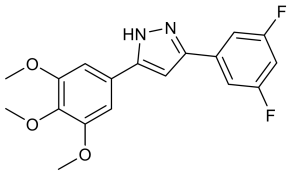	27
anle138c	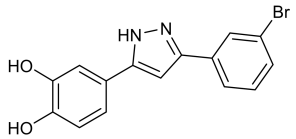	88	anle253b	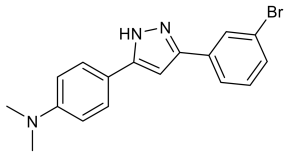	$\leq$ 10
sery159a	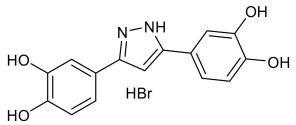	76	anle138b	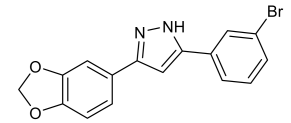	$\leq$ 10
sery95	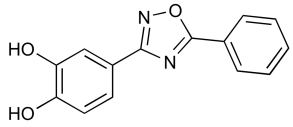	76			

All compounds were tested at a final concentration of 10 µM, a concentration that reflects best physiological conditions. Since lower dosages with a high inhibition potency would be favorable for further drug developments, we next analyzed a possible dose-response relationship for two of the most potent inhibitors, anle138c and sery166a. Their effect on the C183R mutant aggregation was analyzed at 0.1, 0.3, 1, 3 and 10 µM concentration.

Analysis of this data revealed that the high-intensity SIFT signal decreases with increasing compound concentration. Highest signals could be found in the DMSO control, whereas no multimeric signal could be observed with a compound concentration of 10 µM. At 1 µM both compounds showed significant inhibition of more than 50 %. For sery166a this was already the case at 0.3 µM (Figure 2.14). No difference in baseline signal could be observed for both compounds. These data confirm that both compounds have a high inhibition efficacy, thus inhibiting Notch3 aggregation already at low concentrations.

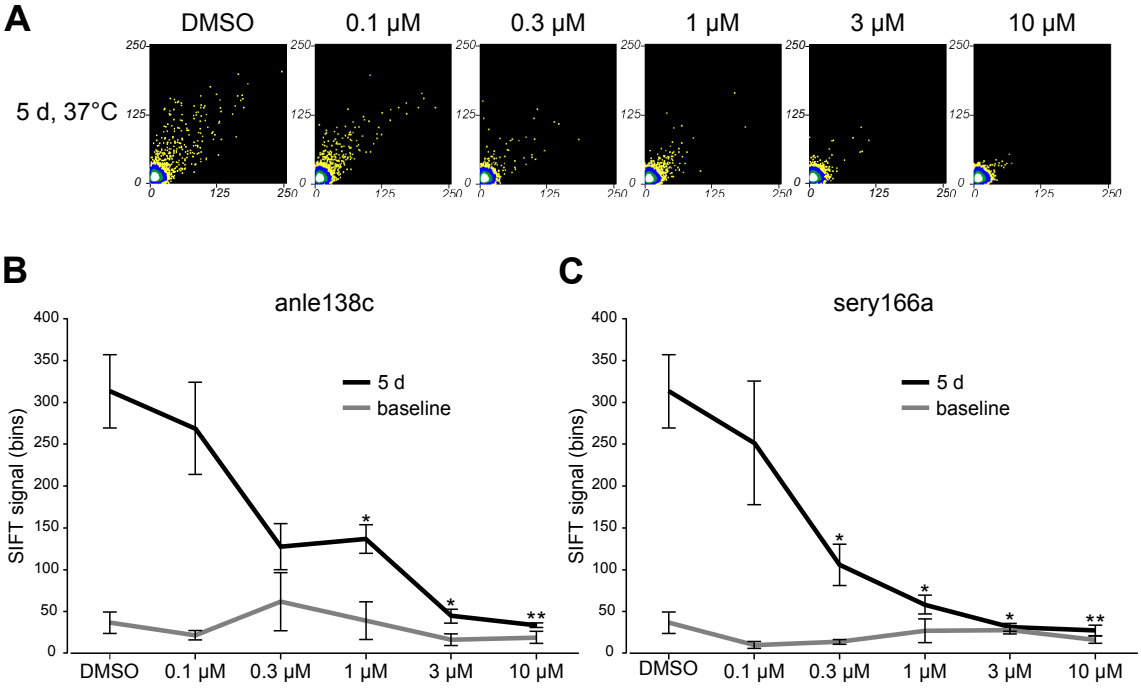

Figure 2.14: Dose dependency of anle138c and sery166a on Notch3-EGF$_{1-5}$ aggregation. A) SIFT-signal revealed decrease in high-intensity signals with increasing compound concentration at day five. B+C) Dose-dependency curves of anle138c (B) and sery166a (C) at baseline and day five. Concentrations decline from 10 µM to 0.1 µM in 1 % DMSO. Mean + SEM of four independent experiments; group statistics compared with DMSO control at the same time point; * $p<0.05$; ** $p<0.01$ (Mann-Whitney test).

2.3.2 Natural polyphenolic compounds

In our analysis of different synthetic small molecule compounds we could define the presence of one or more OH groups as a key feature for effective inhibition of Notch3 aggregation (see section 2.3.1). An important class of compounds characterized by the presence of multiple OH groups on aromatic rings are the natural polyphenolic compounds. They are abundant in a wide range of fruits, herbs, vegetables and beverages (Table 2.2) and have been well studied in a variety of clinical conditions including neurodegenerative diseases[99,100]. Most notably, they have been demonstrated to influence the aggregation of α-syn *in vitro*, a process crucial for the development of PD.[96,97] Since their bioavailability and physiological tolerance have been studied extensively, we decided to test a variety of them for their ability to inhibit Notch3 aggregation.

Table 2.2: List of natural polyphenolic compounds used in this work. All natural polyphenolic compounds are listed together with their chemical description and source. BTE: black tea extract, EGCG: (-)-epigallocatechin gallate

Name	Class	Source
Apigenin	flavone	chamomile, celery, parsley
Baicalein	flavone	roots of *Scutellaria baicalensis*
BTE	$\geq$ 80 % theaflavins	black tea
Catechin	flavanol	apples, barley, black currant, cocoa, peaches
Chrysin	flavone	chamomile, honeycomb, passion flower
Curcumin	diarylheptanoid	tumeric
EGCG	flavanol	black-eyed peas, cocoa, grapes, lentils, tea, wine
Fisetin	flavanol	apples, grapes, onions, strawberries, tea, wine
Genistein	isoflavone	red clover, soybeans
Gingkolide B	terpenic lactones	gingko leaves
Morin	flavonol	Osage orange, old fustic, leaves of common guava
Myricetin	flavonol	black currant, grapes, walnuts
Propylgallate	phenylpropanoid	artificial food additive
Quercetin	flavanol	apples, beans, broccoli, wine
Resveratrol	stilbenoid	red grape skins, roots of Japanese knotweed, red wine
Rosmarinic acid	phenolic acid	basil, lemon balm, marjoram, rosemary, sage
Tannic acid	phenolic acid	woods

We selected 16 natural polyphenols and black tea extract (BTE), which contains > 80 % polyphenolic compounds, to investigate their effect on Notch3 aggregation (Figure 2.15). Of interest, nine of them belong to the group of flavonoids (Figure 2.15 boxed compounds), which includes flavones, isoflavones and flavanols (Table 2.2) and show a similar structure as the most potent synthetic inhibitors anle138c and sery166a evaluated in section 2.3.1.

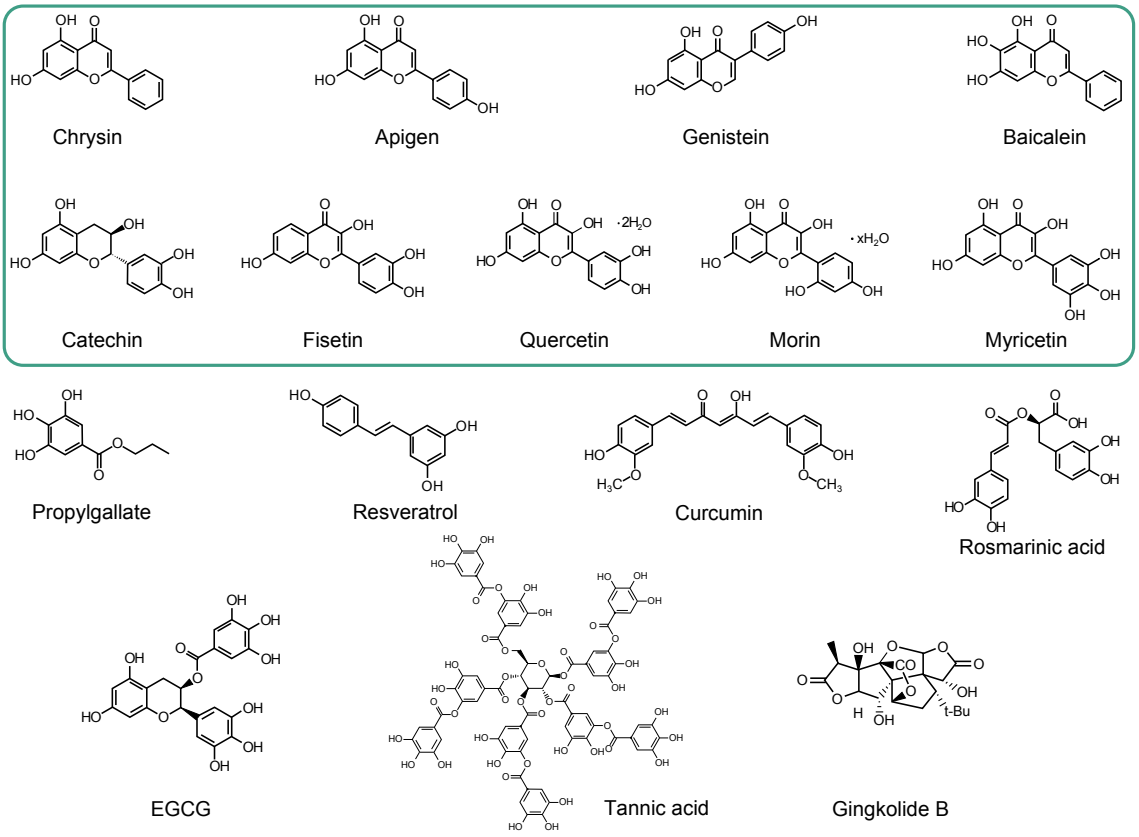

Figure 2.15: Chemical structure of natural polyphenols used in this work. Compounds within the box represent flavonoids.

The remaining compounds belong to molecule classes with unrelated structures, but all contain at least two OH groups. (Fig. 2.15). Similar to the analysis of synthetic compounds natural polyphenols were tested in the SIFT assay at a final concentration of 10 µM on Notch3-EGF$_{1-5}$ R183C fragments for three and five days. Data from a representative experiment with apigenin (no inhibition), BTE and baicalein (both strong inhibition) are shown in Figure 2.16 A. Quantitative analysis at day five of four experiments performed with all compounds revealed inhibition efficiencies between 50 and 85 % with almost half of the compounds (morin, resveratrol, tannic acid, catechin, quercetin, rosmarinic acid, baicalein and BTE) showing a significant reduction (Figure 2.16 B). However, the overall inhibitory effect was weaker compared to the synthetic small-molecule compounds. The weakest significant change could be observed with the flavanole morin (50 % inhibition), whereas the strongest effect could be obtained with BTE (75 % inhibition), which consists about 80 % of theaflavins. This result is comparable to the inhibition efficiency of the middle group of synthetic compounds that show a significant aggregation inhibition up to 25 %. However, we could not identify more potent inhibitors within this set of natural polyphenols that could reduce the aggregation further.

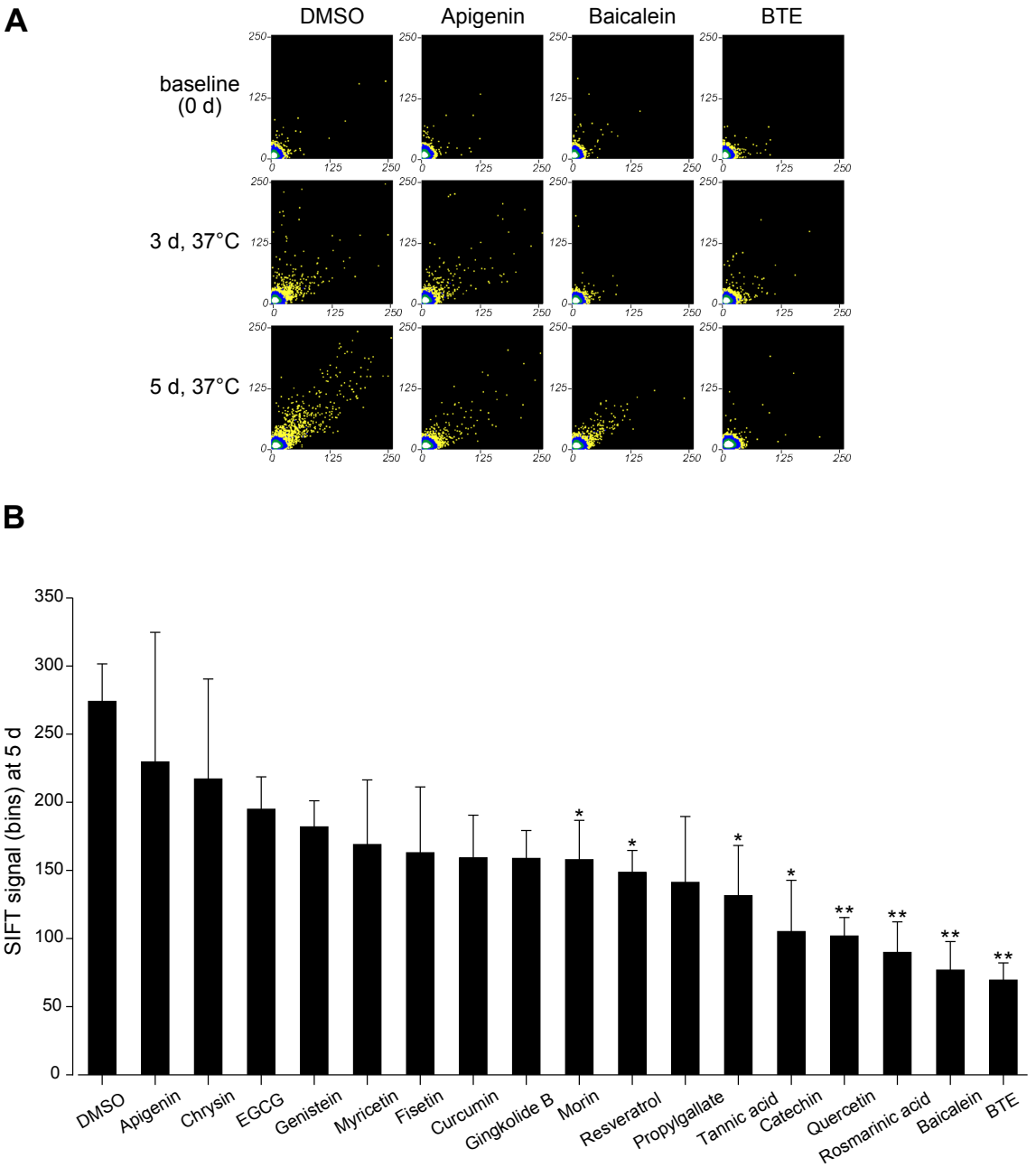

Figure 2.16: Aggregation inhibition using natural polyphenolic compounds. A) Representative 2D histogram plots show either no (apigenin) or strong (baicalein and BTE) reduction of multimer formation after addition of 10 µM compound to mutant Notch3-EGF$_{1-5}$ at baseline incubation for five days at 37°C compared to DMSO control. B) Quantification of dual-color high-intensity SIFT signals at day five for *de novo* inhibition of Notch3-EGF$_{1-5}$ C183R aggregation using natural polyphenolic compounds at a final concentration of 10 µM in 1 % DMSO. Mean + SEM of four independent experiments; group statistics compared with DMSO control at the same time point; * $p<0.05$; ** $p<0.01$ (Mann-Whitney test).

These data not only demonstrate that SIFT-analysis is an ideal method to identify potent inhibitors of Notch3 aggregation *in vitro* in different compounds classes, but also suggested that structural analysis of aggregate-compound interaction would need further investiga-

tion. Still, we have revealed different compounds, synthetic as well as natural, that could serve as pharmacological basis for an efficient drug development for CADASIL.

2.3.3 Dissolution of preformed aggregates

The formation of Notch3 aggregates and GOM deposits represents an early event in CADASIL pathogenesis.[68] Thus, the dissolution of preformed aggregates would be a highly desirable feature of clinically interesting inhibitors. We addressed this question by testing the efficacy of the most potent of our identified aggregation inhibitors on pre-formed Notch3-EGF$_{1-5}$ C183R multimers. Our previous studies have shown aggregate dissolution is principally possible using a combination of 1 % SDS and 1 % β-ME[71] and we used this condition as positive control. We first performed a pilot experiment with two of the most potent inhibitors anle183c and baicalein to test the dissolution kinetics. Notch3 multimers were pre-formed over five days and after addition of the compounds at a final concentration of 10 µM, SIFT signals were measured at baseline, two and four hours. As depicted in figure 2.17, neither baicalein nor anle183c exhibited significant effects within the used time periods, while SDS and β-ME treatment led to a complete loss of the multimer signal immediately after addition.

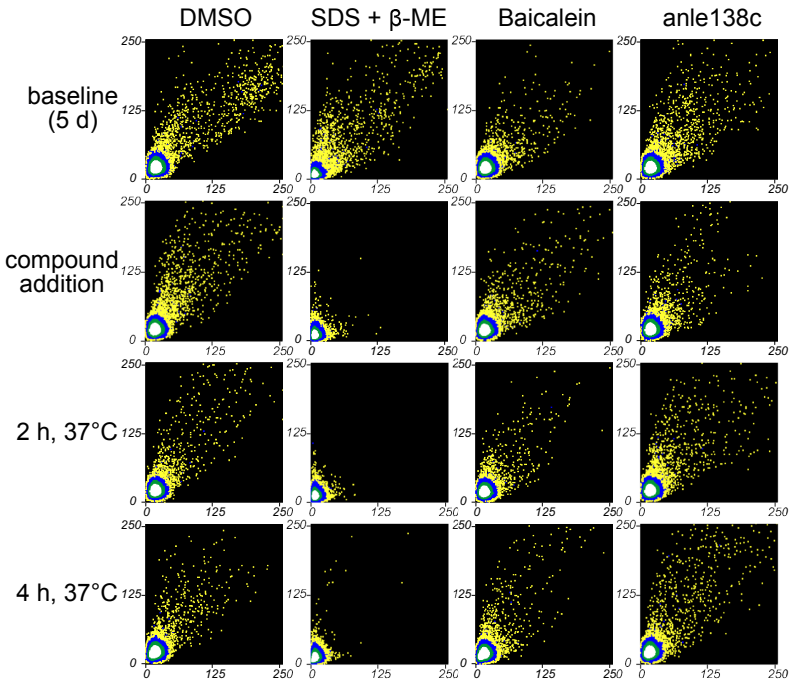

Figure 2.17: Dissolution analysis within four hours. Pre-formed Notch3 aggregates were incubated with 10 µM baicalein, anle138c and the combination of 1 % SDS and 1 %β-ME as control, respectively, and analyzed over a time period of four hours. The addition of SDS and β-ME resulted immediately in a loss of the multimer signal, whereas the addition of baicalein or anle138c did not show any effect.

Next, we prolonged treatment time to 24 hours to account for possible slow dissolution kinetics and examined seven synthetic and four natural compounds. Figure 2.18 shows the raw data of a representative experiment and Figure 2.19 the quantification of three independent experiments. Similar to the inhibition experiments, synthetic compounds showed a much stronger activity compared to natural polyphenols with anle137c and anle138c as most potent molecules with dissolution rates about 90 %. In contrast, their close derivatives anle137b and anle138b showed no activity at all indicating that inhibition of aggregate formation and aggregate dissolution are mediated by the same chemical groups. As most potent natural polyphenols baicalein and rosmarinic acid turned out with dissolution rates of 50-60 %. Interestingly, BTE did not show any dissolution effect despite representing the most potent aggregation inhibitor suggesting a mechanism of action different from the other compounds.

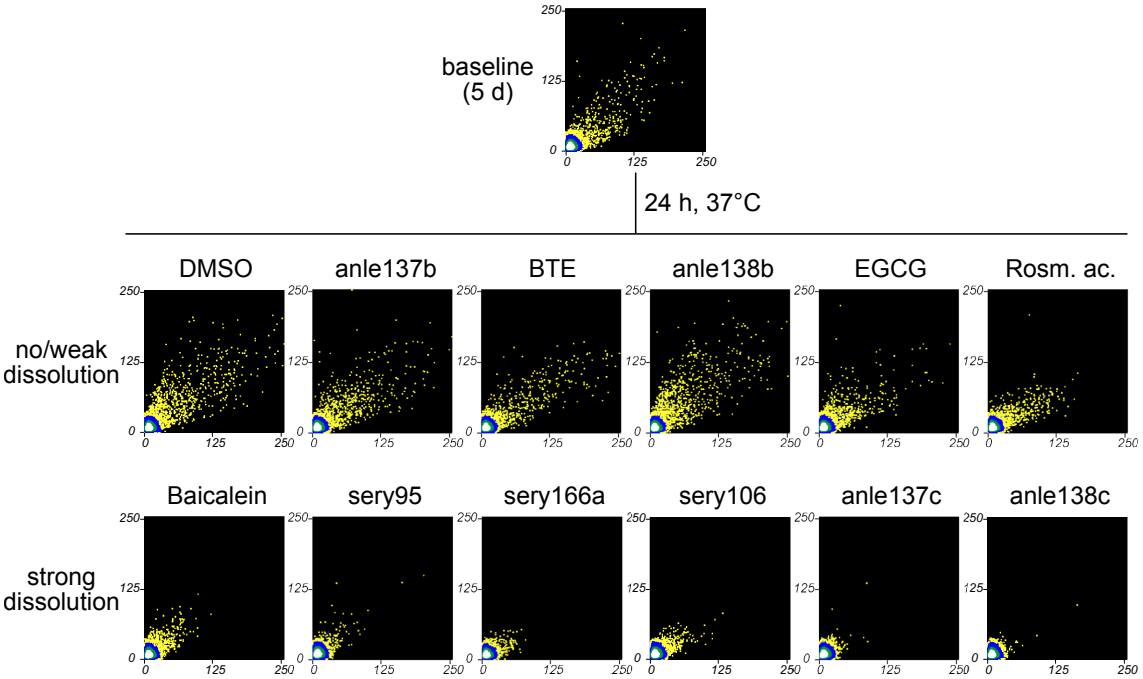

Figure 2.18: Dissolution of pre-formed Notch3 multimers. Pre-formed Notch3 aggregates were incubated with 10 µM of different compounds for 24 hours and subsequently analyzed. Compounds could be divided into two groups: One that had no or little dissolution effect, and the other that showed the ability to dissolve pre-formed aggregates almost completely.

Taken together, these data demonstrate that Notch3 aggregation *in vitro* can be inhibited efficiently by different small-molecule compounds. The much slower kinetics compared to artificial aggregate dissolution indicates that the process is specific. Substances containing OH group might be promising candidates for high-efficiency inhibitors. Thus, selected compounds are worth to be examined further.

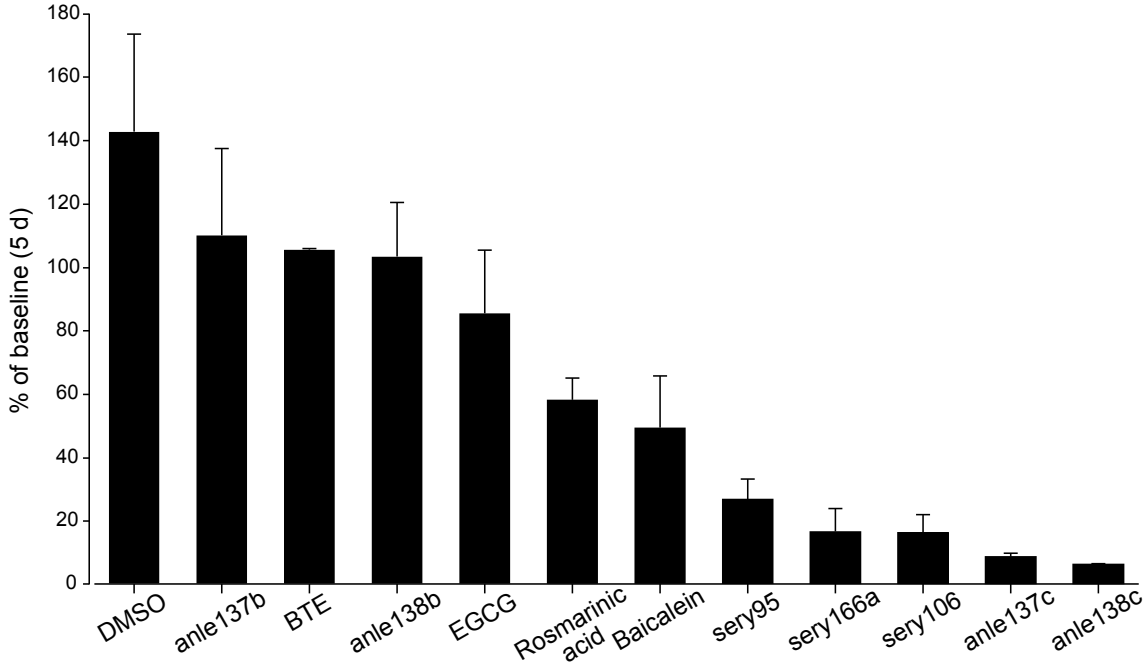

Figure 2.19: Analysis of pre-formed Notch3 multimer dissolution. Quantification of the relative amount of high-intensity SIFT-signals after dissolution compared to the pre-formed multimers. Mutant Notch3 was pre-formed for five days at 37°C, inhibitors from the synthetic small molecule group as well as from the natural polyphenols were added with a final concentration of 10 µM and the mix was further incubated for one day at 37°C. Mean + SEM of three independent experiments.

2.4 Notch3 aggregation analysis in cultured MEFs

Having identified compounds with anti-aggregatory Notch3 activity in our SIFT assay, we sought to develop a more physiological system for validating the most promising candidate inhibitors. In CADASIL patients GOM deposition occurs in the extracellular space within vessel walls. Thus, Notch3 deposits are likely to occur within the ECM network and proteomic studies strongly suggest that ECM components are part of the GOM.[72] Fibroblasts, a major source for the production of ECM proteins, can be cultivated *ex vivo* and are amenable for manipulations such as DNA transfection. We therefore used MEFs to investigate whether the Notch3 aggregation process can be recapitulated under tissue culture conditions.

2.4.1 Transfected MEFs show mutant Notch3 enrichment in the extracellular matrix

All following experiments were performed with five independent MEF cell lines isolated from 14.5-dpc (days post coitus) embryos of wt mice and immortalized through serial passaging by Scharrer[101].

When seeded on a plastic dish and grown to confluence, these fibroblast lines produce an extensive ECM within two to five days. For the analysis of ECM proteins by Western blotting the culture medium was removed and the cells were lysed with a buffer containing 0.1% Triton and 20 mM NH_3. This resulted in a mild cell lysis due to a combination of low detergent concentrations and osmotic swelling (Figure 2.20). After collection of cell lysates and repeated washing steps the ECM was recovered in a Tris buffer containing 1 % SDS and samples were homogenized by pasing through a 25G syringe. Using this extraction method a separation of the cellular and ECM protein fractions was achieved.

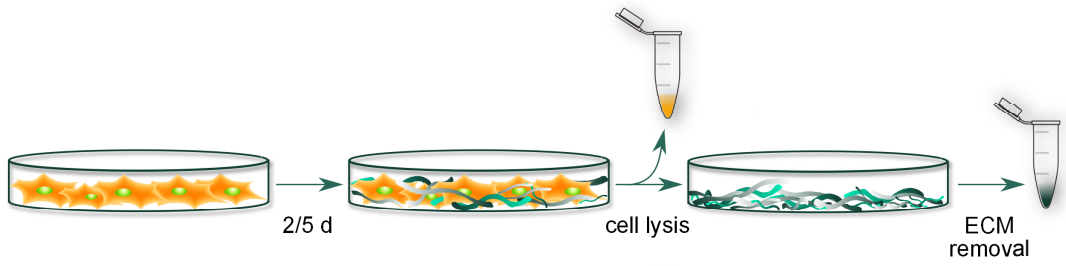

Figure 2.20: Scheme of matrix separation. Cultured MEFs build up a stable ECM. After growing them for two or five days, the cells were treated with a mixture of 0.1 % Triton as a mild detergent in combination with 20 mM NH_3, that leads to an unbalanced osmotic pressure within the cells leading to cell lysis without affecting the ECM. After several washing steps the ECM was resuspended in buffer containing 1 % SDS.

To analyze the behavior of Notch3 in this system, transfection of fibroblasts with wt and C183R mutant Notch3-EGF_{1-5} fragments containing a C-terminal myc-His tag was performed. As we could already show in HEK293E cells, these truncated ECD constructs are efficiently secreted (Figure 2.2). Cells were transfected after reaching $\sim$ 90 % confluence and harvested five days later. Immunodetection of Notch3 fragments was achieved with an anti-myc antibody. As control for the purity of our preparations and for equal gel loading we used antibodies against fibronectin, platelet-derived growth factor receptor beta (PDGFRβ) and tubulin. Fibronectin is secreted from fibroblasts and incorporated into the ECM, PDGFRβ is a transmembrane receptor and was used to monitor the absence of plasma membrane proteins in the ECM fraction and tubulin is a cytosolic protein found exclusively in the cellular fraction. Immunoblotting for these proteins revealed a high extent of separation between medium, cellular and ECM fraction (Figure 2.21). Fibronectin was detected only in the medium and the ECM indicating that our cell lysis conditions did not affect the matrix. Furthermore, cell lysis was complete, as a tubulin signal was visible only in the lysate fraction. The main fraction of cell membranes could also be removed as evident from the very low PDGFRβ signal present in the ECM fraction. Labeling with the anti-myc antibody revealed comparable secretion of wt and C183R Notch3 into the medium. In the cell lysate fractions only little amounts of Notch3, both wt and C183R mutant, could be observed, whereas the ECM fraction revealed a strong

enrichment of mutant but not wt Notch3. In the cellular and ECM fractions several bands of higher molecular weight were observed (Figure 2.21 asterisks), but appeared also in the control lanes and thus represent unspecific signals. The signal at about 60 kDa possibly represents Notch3 dimers.

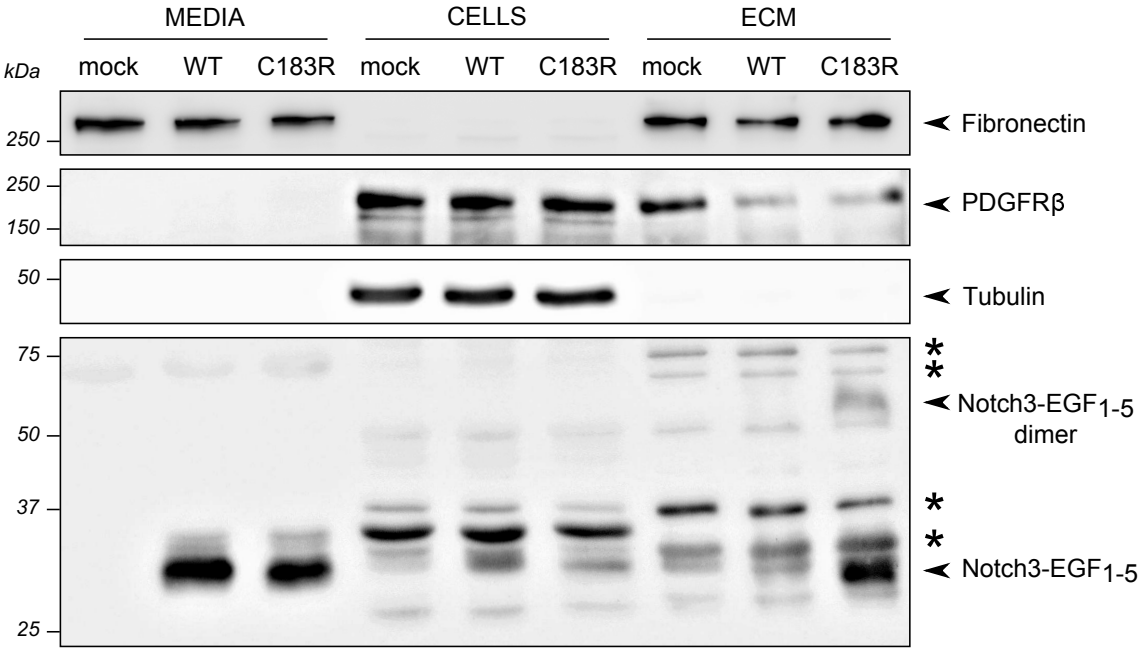

Figure 2.21: Mutated Notch3 EGF$_{1-5}$ but not wt accumulates in the ECM fraction. MEFs were transfected with either Notch3 EGF$_{1-5}$ myc-His C183R, wt or empty vector (mock). Conditioned media, cell lysates and ECM fraction were collected after five days and analyzed by Western blotting under reducing conditions. Purity and equal loading for each fraction was controlled using antibodies against fibronectin for the conditioned media and the ECM fraction and against tubulin for the cell lysates. Immunoblotting with an antibody against PDGFRβ, a transmembrane protein, served as control for identifying traces of cell membrane remaining in the ECM fraction. Whereas both, wt and C183R Notch3 EGF$_{1-5}$, show equal secretion into conditioned media, only the mutant accumulates in the ECM fraction as detected by the anti-myc antibody. * indicate unspecific bands.

To further investigate the Notch3 accumulation process, we harvested transfected MEFs at two different time points, two and five days after transfection. Figure 2.22 shows that already after two days mutant Notch3-EGF$_{1-5}$ could be detected in the matrix in a considerable amount. After five days, the signal of the monomeric form did not increase significantly, but bands of higher molecular weight appeared likely representing dimers, trimers and higher order oligomers. In contrast, no significant amounts of wt Notch3 were detected in the ECM fraction.

To verify the enrichment of mutant Notch3 in the ECM, we performed immunofluorescent microscopy. We treated the MEF culture in the same way as for matrix harvesting, but fixed the cells five days after transfection with 4 % PFA and stained with antibodies against fibronectin and myc tag. We did not permeabilize the cells with any detergent, thus, only

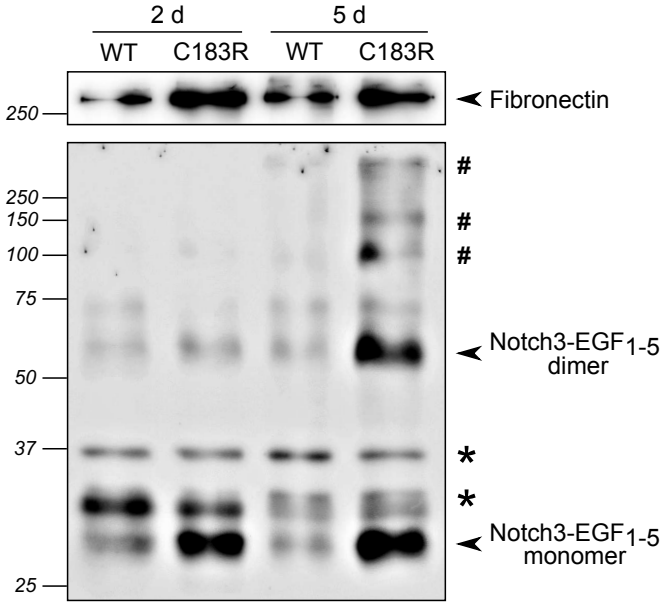

Figure 2.22: Mutated Notch3 EGF$_{1-5}$ shows high molecular bands in the ECM fraction. ECM fractions of MEFs were harvested 2 days and 5 days after transfection, respectively. Immunoblotting with the anti-myc antibody under reducing conditions revealed after 2 days a monomeric Notch3-EGF$_{1-5}$ of mutant C183R. After 5 days an additional band of $\sim$ 58 kDa, likely a dimer, and several bands of higher molecular weight (#), possibly higher-oder oligomers, appeared. None of those bands could be detected in significant amounts with the wt construct. * indicate unspecific bands.

extracellular proteins were detected. Staining for fibronectin revealed an extensive fibrillar network demonstrating that an ECM had been formed by the fibroblasts. Similar to the immunoblotting results Notch3 deposition in the ECM could only be detected with C183R but not wt protein (Figure 2.23).

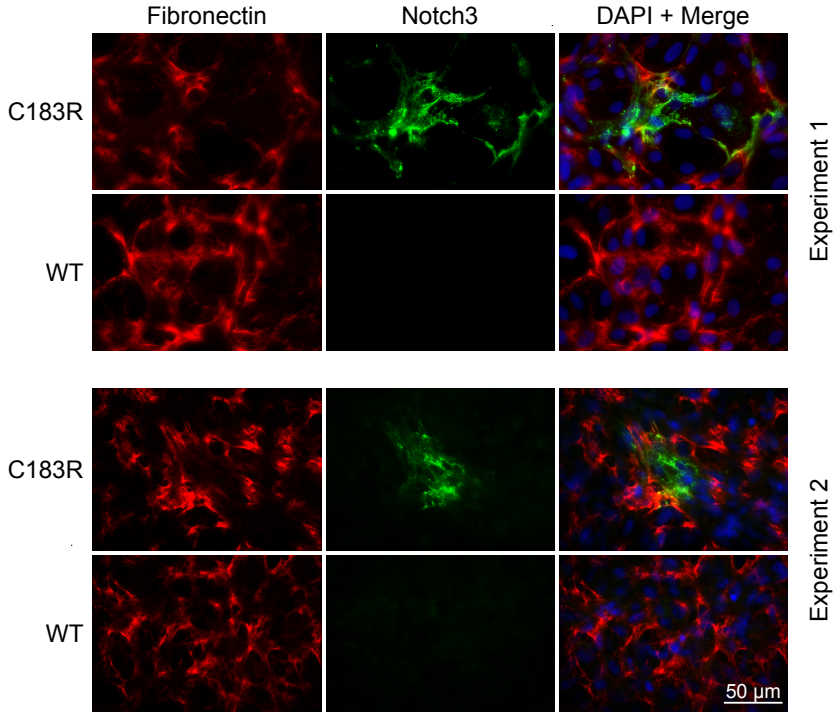

Figure 2.23: Deposits of mutated Notch3 EGF$_{1-5}$ but not wt are localized in the ECM of MEFs. Transfected MEFs were fixed with 4 % PFA remaining non-permeabilized. Cells were stained with antibodies against fibronectin and myc, the latter for detecting myc-tagged Notch3 EGF$_{1-5}$, and analyzed by immunofluorescence.

Higher resolution images of the matrix from mutant expressing cells showed Notch3 staining in a dot-like structure along extracellular fibers, partly also stained for fibronectin (Figure 2.24). This suggested that mutant Notch3 accumulates locally within the ECM of fibroblasts and provided strong evidence that the aggregation of CADASIL-mutant Notch3-EGF$_{1-5}$ fragments can be recapitulated in cultured cells.

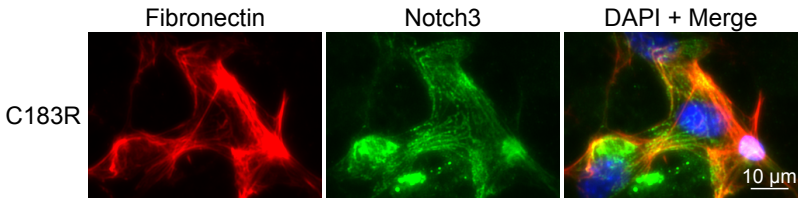

Figure 2.24: Notch3 EGF$_{1-5}$ C183R is enriched in a dot-like structure in the ECM and shows an intense accumulation pattern. Non-permeabilized MEFs transfected with Notch3 EGF$_{1-5}$ C183R were stained with antibodies against fibronectin and myc and analyzed by immunofluorescence.

2.4.2 Preselected compounds show different effects on extracellular Notch3

In section 2.3 we identified several potent small molecule compounds that could effectively inhibit the formation and promote the dissolution of Notch3 aggregates *in vitro*. However, the GOM accumulation *in vivo* likely involves factors other than Notch3 and potential aggregation inhibitors have to be efficient also in such more complex systems. We, therefore, used pre-selected inhibitors in our established cell culture assay to test their effect in a more physiological setting.

We performed the assay as described in section 2.4.1. Since we could demonstrate that already two days after transfection a detectable amount of mutated Notch3 is enriched in the ECM fraction (Figure 2.22), we started the compound treatment at this time point. We added anle138b, anle138c and baicalein at a final concentration of 10 µM to the medium and incubated the cells for three more days. Control cells were treated with the same volume of 1 % DMSO.

Immunoblot analysis of conditioned media with the anti-fibronectin antibody showed that treatment with the compounds did not impair protein secretion (the weaker signal in the control sample was due to reduced protein loading) (Figure 2.25).

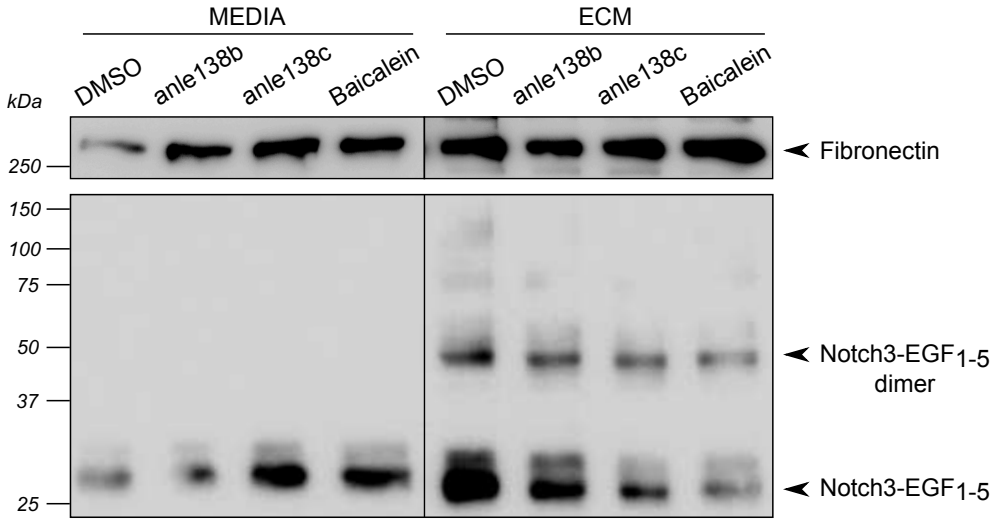

Figure 2.25: Notch3 EGF_{1-5} myc-His ECM accumulation is reduced by compound treatment. MEFs were transfected with mutant Notch3 EGF_{1-5}-myc C183R. Two days after transfection, preselected compounds anle138b, anle138c and baicalein were added at a final concentration of 10 µM and incubated for three more days. DMSO served as control. ECM was harvested and analyzed together with conditioned media by Western blotting. Proteins were detected with anti-fibronectin and anti-myc antibodies.

Staining for the Notch3 mutant revealed a strong reduction upon treatment with baicalein and anle138c, both very effective compounds, in the *in vitro* assay. For anle138b, which had shown no effect *in vitro*, a much less pronounced reduction was observed. Moreover, bands of higher molecular weight likely representing Notch3 C183R oligomers were also

reduced in a manner comparable to monomers further indicating an inhibition of Notch3 oligomerization. These data indicate that the cellular assay largely recapitulates the effects of anti-aggregatory compounds from the SIFT assay.

3 Discussion

The accumulation and aggregation of the Notch3-ECD is a hallmark of the monogenic SVD CADASIL and considered the starting point of a series of pathological events eventually resulting in the malfunction of the cerebral microvasculature.[63] The aggregation process, which is typically initated by *NOTCH3* mutations affecting the number of cysteine residues, has recently been recapitulated in an *in vitro* assay by using the single molecule detection technique SIFT. In this thesis the assay was further optimized, applied to the investigation of the pathogenic potential of rare cysteine-sparing mutations and used to screen for small-molecule compounds with anti-aggregatory properties.

To improve yield and purity of the Notch3 fragments required for the SIFT assay, the HaloTag purification system was used allowing the more efficient removal of contaminating proteins during the purification procedure and the protease-mediated elution of Notch3 proteins from the affinity matrix. This yielded in highly pure protein without affinity tag and in two-fold higher amounts than with the previously used His-tag-mediated purification. Furthermore, the usage of EDTA in the elution step was no longer required and the purified protein could be obtained in the final aggregation buffer. Its analysis in the SIFT assay revealed an aggregation behavior of wt and mutant variants comparable to previous experiments.

3.1 Cysteine-sparing Notch3 variants can be pathogenic

For decades the prevailing dogma in the CADASIL field stated that only a change in the number of cysteine residues and thus in the organization of disulfide bridges can initiate missfolding and trigger aggregation of the Notch3-ECD. However, in the last years the question whether cysteine-sparing Notch3 variants represent only polymorphisms or pathogenic mutations has been heavily debated.[73,81,102] At least in some cases including one reported by our group[85] strong evidence for a clinical relevance emerged. We therefore decided to study the pathogenic potential of five of these mutations in our *in vitro* aggregation assay in comparison to wt Notch3, three well-characterized cysteine mutants and three non-pathogenic polymorphisms. The latter are defined by their high prevalence in the population (0.1 to 0.3 % allele frequency in the ESP). Whereas their multimerization behavior was comparable to wt protein, the three selected cysteine mutants showed a significant increase of multimer signal at day three and five. The outcome of the five

selected cysteine-sparing mutants was variable , with R75P, D80G and ΔA88-G91 showing multimerization comparable to the cysteine mutants, and R61W and R213K revealing no significant signal. These inconsistent results led us to reevaluate the reported clinical data of the mutation carriers (Table 3.1).

Table 3.1: Evaluation of cysteine-sparing mutants.

Mutation	Biochemical properties	Accuracy of clinical data	SIFT aggregation
R61W	basic → aromatic	−	−
R75P	basic → structural	+	+
D80G	acidic → aliphatic	+	+
ΔA88-G91	deletion	+	+
R213K	basic → basic	−	−

The data available for the three variants showing an effect in our assay further support their classification as pathogenic mutations. R75P is the best characterized cysteine-sparing mutation to date with data available from several Asian families.[77–79,83,84] MRI findings of patients were typical for CADASIL and the presence of GOM deposits could be demonstrated providing convincing evidence for the diagnosis. Furthermore, the replacement of a basic arginine residue by a bulky proline, a known structural disruptor of α-helices and β-sheets, likely leads to a conformational change of the affected EGF-like repeat increasing the aggregation potential.

The D80G mutation was found in four patients, but neither in healthy members of a affected German family nor in control genomes from the ESP.[85] The mutation carriers showed an archetypical CADASIL phenotype in absence of vascular risk factors. Although the presence of GOM could be shown in only one subject, all affected family members showed T2-hyperintense lesions in the temporal pole, which is the most prominent MRI finding in CADASIL patients. The replacement of an acidic aspartate by a small aliphatic glycine is also likely to influence the protein conformation.

The ΔA88-G91 deletion was identified in one Italian family.[76] Although the patient number (2) is small, the pathogenicity of the mutation can be considered as well documented on the basis of clinical and histological data. Although no cysteine is affected, the deletion of four amino acids changes the highly conserved distance between two cysteine residues likely disrupting the protein structure in a significant way.

In contrast, the R61W and R213K mutations did not exhibit significant multimer formation raising doubts about their clinical relevance. This is supported by the incomplete description of their clinical phenotype. Although the two siblings with the R61W mutation suffered from migraine and stroke-like episodes, their white matter lesions as determined

by MRI were atypical. Furthermore, they had no family history for neurological deficits.[82] The presence of GOM deposits was reported, but only from the patient's brother carrying the same mutation. Thus, the clinical evidence for CADASIL in this case was not entirely convincing. Moreover, recent data from the ESP revealed an allele frequency for the R61W variant of 0.05 % in Americans of European origin, (Table 1.2), a number far higher than the estimated CADASIL prevalence of 2-4/100,000.[103] Although the replacement of a basic arginine by an aromatic phenylalanine residue may also cause an interruption of secondary protein structure, we tend to the conclusion that R61W is rather a polymorphism than a disease-causing mutation. However, additional investigations including detailed structural analysis and comprehensive examination of more patients carrying this mutation are required to make a definite statement.

The R213K mutation was found in a single autopsy case with questionable genetic, clinical and histological data.[74,75] Only mild migraine, moderate dementia and gait disturbance were reported as neurological and neurophysiological symptoms. The authors even considered the possibility of a vascular disease different from CADASIL[74] or a rare polymorphism.[75] Although we could not find this variant in the ESP, we still consider it as rare polymorphism, an assumption supported by the conservative nature of the amino acid exchange, with the substitution of one basic amino acid by another basic one.

In summary, our *in vitro* aggregation data provide further evidence for the pathogenicity of some cysteine-sparing mutations raising two possibilities as underlying mechanisms. First, such an amino acid exchange may lead to a conformational change which in turn results in the disruption of an existing disulfide bond. As a consequence two unpaired cysteines would be generated triggering a sulfhydryl group-mediated multimerization similar to cysteine mutants. Second, the cysteine-sparing amino acid exchange may lead to misfolding via a cysteine-independent mechanism such as exposing hydrophobic parts and triggering the formation of β-sheet-rich oligomeric structures, a common cause of protein aggregation. Although contradicting the current view of disulfide-mediated Notch3 aggregation, this possibility has to be given more attention in future studies. In addition to providing a valuable tool for mechanistic studies, our aggregation assay might in the future be used for diagnostic purposes to distinguish more clearly between benign Notch3 polymorphisms and pathogenic CADASIL mutants. The reported CADASIL cases carrying cysteine-sparing mutations are rare in the literature, but maybe they have been so far mostly overlooked due to the fact that CADASIL was originally characterized as a disease caused by cysteine mutations. Future studies are required for a better understanding of the role cysteine-sparing mutants play in CADASIL pathogenesis.

3.2 Identification of anti-aggregatory compounds

Since the vascular deposition of Notch3-ECD is a central determinant of CADASIL pathology, preventing Notch3 aggregation is likely to represent a promising therapeutic approach. One goal of this study was to evaluate whether our *in vitro* assay is suitable for the identification of Notch3 aggregation inhibitors. Bertsch et al.[104] had used SIFT for a high-throughput screening of 10,000 drug-like compounds to identify lead structures for anti-prion drugs. Compounds of the DPP class were found to be highly effective and Wagner et al.[98] tested a focused DPP library consisting of 150 compounds *in vitro* for the inhibition of pathological PrP and α-syn oligomer formation and further in cell culture and *in vivo* animal models. They could identify anle138b as novel disease-modifying substance that targets directly and specifically oligomeric forms of proteins. Based on this study we investigated the effect of 15 DPP-based compounds on Notch3 aggregation. We identified six compounds with a high (> 80%) and three with a moderate (> 68%) ability to inhibit *de novo* multimer formation. Anle138b showed no effect at all, but the closely related derivative anle138c was highly active. The six most potent inhibitors for Notch3 showed similar effects in the inhibition of α-syn comparable to the results reported in Wagner et al.[98] (Table 3.2).

Table 3.2: Efficiency of various DPP inhibitors on Notch3 and α-syn aggregation in the SIFT assay.

Compound	% inhibition of Notch3	% inhibition of α-syn[a]
sery105	94	95
sery166a	91	100
anle137c	91	100
sery106	91	97
anle136c	90	99
anle138c	88	100
sery159a	76	100
sery95	76	69
sery320a	68	≤ 10
sery144	58	91
sery139	55	100
sery118	44	76
anle137b	27	≤ 10
anle253b	≤10	50
anle138b	≤10	77

[a] A. Giese, unpublished data

This raises the interesting possibility that DPP compounds can act on various kinds of neurotoxic aggregates. However, Notch3 aggregates have so far been assumed to be structurally different from those formed by most other misfolded proteins, since they do not consist of amyloid fibrils and do not bind to certain chemical dyes such as Congo red and thioflavinT. For anle138c and sery166a, two of the highly effective compounds, we in addition obtained dose-response curves, which revealed that already concentrations of 0.3 µM are sufficient for significant inhibition. These are important data for further therapeutic studies, since lower concentrations are in a better agreement with the drug tolerance of cells or living organisms.

Based on our data we performed a structure-activity analysis revealing that an inhibition of > 40 % requires the presence of at least one OH group. However, this chemical group seems to be necessary but not sufficient for effective inhibition, other molecular features may be crucial as well. Comparing the structure and hydrophobicity of anle138c, a potent compound with an inhibition efficacy of 90 %, and sery118 with an efficacy of 44 %, revealed that although their molecular composition is similar (Table 2.1), however the 3D structure as well as the arrangement of hydrophobic and hydrophilic parts are different (Figure 3.1). This diversity may be important for binding to Notch3 and thus inhibiting the aggregation process.

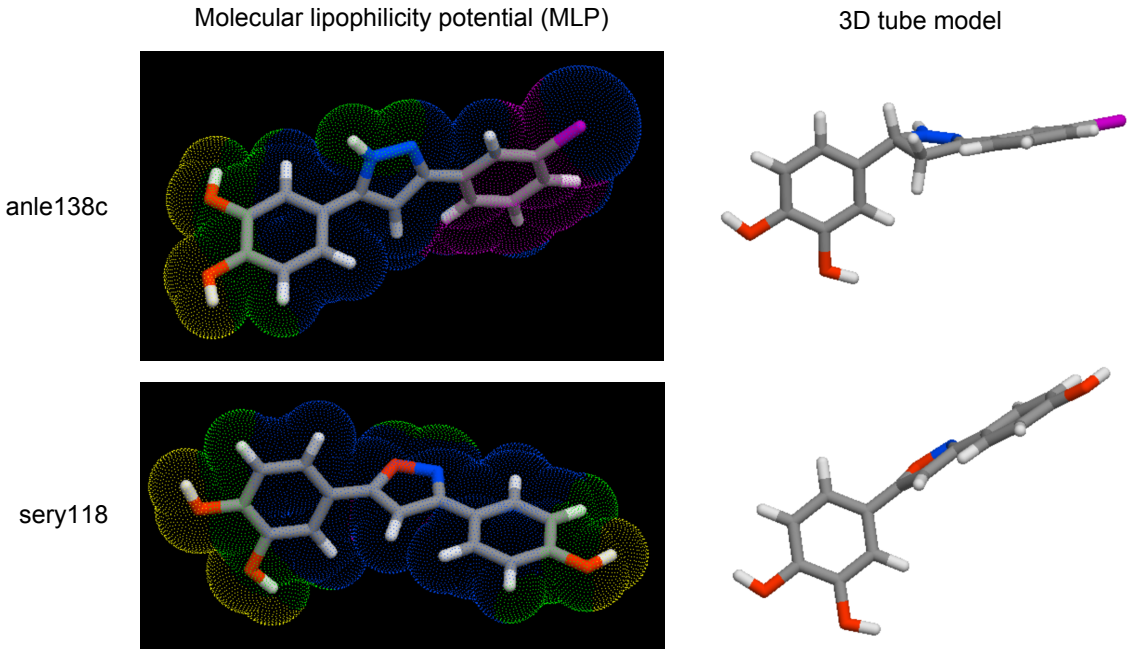

Figure 3.1: Structural details of anle138c and sery118. Structures of both compounds are displayed as 3D tube model with atoms in different colors: grey = C, white = H, red = O, blue = N and pink = Br; and with their molecular lipophilicity potential (MLP): pink and blue dots = hydrophobic surface, yellow and green dots = hydrophilic surface. MLP is calculated from atomic hydrophobicity contribution. Structural models were created with molinspiration.com

To identify the exact binding site of protein and inhibitor, detailed structural analysis will be required. However, the atomic resolution structure of the Notch3-ECD remains

to be elucidated, which is a major challenge for drug development in the CADASIL field. Thus, our SIFT assay is an innovative approach for the drug identification, since only low concentrations of Notch3 are required and it is easy to screen for candidates for further assessment. We provide proof-of-principle for the suitability of this assay to identify aggregation inhibitors. In the future, systematic variations of the structure of effective inhibitors have to be performed to reveal a well-defined structure-activity relationship as it has been done in the work of Wagner et al. [98]. Since the identified effective compounds have a poor predicted bioavailability due to their OH groups, screening of additional compound classes might be required. Furthermore, the results of our experiments have to be validated with additional mutants including ones from other ECD regions.

Due to the apparently important role of OH groups for the inhibition of Notch3 aggregation, we decided to investigate natural polyphenols, a group of compounds rich in OH groups. They are abundant in food and beverages of plant origin and considered as responsible for the observed beneficial effect of Mediterranean and Asian diets on cardiovascular and neurodegenerative diseases. [105] Several of them have been shown to inhibit the aggregation of α-syn in a SIFT assay. [96,97] We selected 16 natural polyphenols as well as BTE, a mixture of mostly polyphenolic compounds, to analyze their effects on Notch3 aggregation. Their overall inhibition rate was lower compared to the synthetic compounds. Nevertheless, we could identify seven polyphenols and BTE with a significant effect, although the overall inhibition rate was higher towards α-syn aggregates (Table 3.3). [96] The three most effective compounds in our assay were BTE (69 % inhibition), baicalein (68 % inhibition) and rosmarinic acid (66 % inhibition). However, since the bioavailability of natural polyphenols is poor, they are not very well suited as therapeutic drugs. Intelligent drug design and encapsulation strategies may overcome these negative effects and retain the characteristics of the natural product scaffold.

The diagnosis of CADASIL usually is made years after disease onset, when Notch3 deposits have already been formed. Thus, antiaggregatory compounds that are able to resolve preexisting aggregates would be desirable. We therefore investigated the dissolution efficacy of selected synthetic as well as natural inhibitors and found that all compounds effective on the *de novo* aggregation also show dissolution potential, with the exception of BTE. One possible explanation for this finding could be that binding of active BTE components to Notch3-ECD monomers is rather unspecific preventing *de novo* aggregation but not allowing aggregate dissolution. In contrast, the activity of all other identified active compounds could thus be specific, an assumption supported by the finding that the kinetics of compound-mediated dissolution are much slower in comparison to unspecific dissolution with β-ME and SDS.

Table 3.3: Efficiency of various natural polyphenol inhibitors on Notch3 and α-syn aggregation in the SIFT assay. (-)-epigallocatechin gallate (EGCG)

Compound	**% inhibition of Notch3**	**% inhibition of α-syn[a]**
BTE	69	100
Baicalein	68	∼ 97
Rosmarinic acid	66	55
Quercetin	57	88
Tannic acid	44	∼ 98
Resveratrol	37	53
Morin	29	99
Gingkolide B	24	∼ 92
Myricetin	24	90
EGCG	≤ 10	∼ 93
Genistein	≤ 10	31
Apigenin	≤ 10	35
Purpurogallin	≤ 10	∼ 46

[a] Caruana et al. [96]

3.3 Validation of compounds in a novel *ex vivo* assay

Having identified several inhibitors *in vitro*, we aimed to validate them in a more complex and thus physiological system. While a variety of studies have previously been performed examining the effect of CADASIL mutations on Notch3 ligand binding, signaling capacity and actin organization [56,106–110], no cell culture model allowing specifically the analysis of Notch3 aggregation in a physiological setting is available. We therefore established an assay system based on the incorporation of Notch3 fragments into the ECM by transiently transfecting MEFs that produce a stable ECM after reaching confluency with wt and C183R mutant. Using different buffers we were able to collect cell and matrix fraction separately. Analyis by Western blotting revealed a strong enrichment of mutated but not wt Notch3 in the ECM already two days after transfection. At day five bands of higher molecular weight appeared, likely representing dimers and higher-order multimers that could not be resolved under the applied reducing conditions. Immunofluorescence experiments confirmed the mutant-depending Notch3 accumulation. Mutant but not wt Notch3 could be detected in a dot-like structure pattern on fibrillar structures which showed partial co-localization with the ECM protein fibronectin. This finding ruled out an unspecific attachment of Notch3 fragments to the plastic surface of the culture dish and suggested that the accumulation occurs in a focal manner, similar to the deposition of GOM in human vascular material. Nevertheless, further experiments including co-

localization studies with additional ECM proteins are required to find out to what extent these Notch3 deposits in cell culture correspond to *in vivo* aggregates.

Having shown that mutant Notch3 fragments accumulate in aggregate-like structures, we treated the MEFs with three of the compounds with antiaggregatory activity *in vitro*. Western blotting revealed a strong reduction of the Notch3 signal in the ECM fraction upon treatment with anle138c and baicalein recapitulating the results from the SIFT assay. Anle138b, which had shown no effect *in vitro*, also reduced the amount of Notch3 in the ECM, but to a much lesser extent. Whether this is the reason of different compound solubility in the aqueous buffer compared to the hydrophobicity of the matrix has to be further investigated. The generation of stable cell lines constitutively expressing the mutant Notch3 fragment would improve the comparability of the effect of different compounds.

3.4 The future of CADASIL treatment approaches

Our inhibitor studies have yielded several compounds which can now be further studied, e.g. in the mouse model PAC-Notch3 R169C, a well established preclinical CADASIL model. The transgenic mice carry a P1-derived artificial chromosome (PAC) containing the entire rat Notch3 locus with the R169C mutation resulting in a $\sim$ 4-fold overexpression of mutant Notch3.[63] The first pathological alterations the mice show are Notch3-ECD accumulation (at one month of age) and GOM deposits (at five months of age) supporting the view that Notch3 aggregation is the key determinant of CADASIL pathogenesis. At higher age they develop several histological and functional symptoms of a microangiopathy demonstrating that they can also serve as a model for functional analysis. Recently, Ghosh et al.[111] described reduced microvascular reactivity and a reduction of pericytes in this mouse model providing a hint for the underlying cellular pathomechanism. Furthermore, Capone et al.[112] could prove that Timp3 and vitronectin, which are abnormally recruited in Notch3-ECD-containing deposits, play a pathophysiological role in CADASIL. In addition to testing some of the identified compounds *in vivo* it might also be necessary in the future to screen more compound classes with our *in vitro* assay to identify substances with better medicinal chemistry features.

In addition to the antiaggregation approach the possibility of a vaccination as in the AD field is considered. Both active and passive immunization could be used and would also allow a protective vaccination of asymptomatic individuals. However, the aggregating protein Notch3-ECD is large and it is unclear which part of it should be targeted by an antibody. Further, little is known about differences in the toxicity of different Notch3 mutants. It would have to be evaluated whether one immunogen/antibody would be sufficient for treatment of all CADASIL patients or whether several alternative treatments would be necessary. Also, significant targeting of endogenous wt Notch3, required for

a variety of physiological processes, has to be avoided. Even more, the impact of the immune response is generally hard to predict. In AD research, the vaccine AN-1792 used in an active immunization approach did not pass the phase II trial, since several patients developed serious brain inflammation leading to a halt of the trial.[113] In a passive immunotherapy approach, no active antibody production would happen, however, it would require regular applications to maintain the antibody levels. So far, no studies investigating these different kind of questions have been reported demonstrating that a lot of work is still ahead to evaluate the applicability of the immunization approach.

An approach a little bit more advanced is the exon skipping approach suggested by Rutten et al.[114]. Exon skipping is a therapeutic approach that uses antisense oligonucleotides (AONs) to modify a protein on mRNA level either by restoring the open reading frame, blocking gene expression, inducing alternative splicing sites or modifying the number of exons. The most promising results using exon skipping have been achieved with Duchenne muscular dystrophy (DMD) by skipping of an additional exon to restore the protein transcript and in spinal muscular atrophy (SMA) by directing AONs against a splice silencer to include an additional exon.[115] Rutten et al.[114] now proposed the exclusion of the mutated Notch3 EGF-like domain by exon skipping to prevent Notch3 aggregation through cysteine correction. This approach makes use of the fact that the majority of Notch3 exons encode complete single EGF-like domains or combinations of them. Moreover, a variety of exons and exon combinations are amenable for exon skipping due to the preservation of the open reading frame. Rutten et al.[114] selected several exons and exon combinations as targets, analyzed the structure of the corresponding truncated Notch3 proteins by *in silico* studies and designed the appropriate AONs for modulating hnRNA splicing. They could show that skipping occurs to significant extent in cultured cells and that the truncated proteins display normal processing, ligand binding and ligand-induced activation. However, their aggregation behavior could not be comprehensively evaluated due to the lack of an appropriate assay. To analyze this approach further, *in vivo* data from a mouse model will be needed. Also the administration routes have to be evaluated. An alternative AON-mediated approach is the reduction of full-length Notch3 expression in general with the goal to reduce the amount of mutated receptor to a level no longer pathological. However, wt Notch3 would also be affected and its expression levels would have to be tightly controlled in treated cells and tissues.

In summary, several promising therapeutic approaches are considered for CADASIL treatment, however, none of them has so far reached a stadium approaching clinical application. A number of future studies are required to investigate the applicability, efficiency and safety of the different approaches. But with our initial studies on drug-mediated inhibition of Notch3 aggregation we have laid the groundwork for an anti-aggregation therapy that might some day be applied to CADASIL patients.

4 Material and methods

4.1 Equipment

CO_2 incubator HeraCell	Heraeus
Coffee machine DeLonghi	Nespresso
Incubation shaking cabinet Certomat BS-1	Sartorius
Insight Research Reader	Evotec Biosystems
Magnetic stirrer KMO 2 basic	IKA
Magnetic stirrer RCT basic safety control	IKA
Magnetic stirrer RH basic 2	IKA
Microscope Axiovert 200M	Zeiss
Microscope imaging system AxioCam MRm	Zeiss
Microscope Wilovert S	Hund Wetzlar
Multi imaging system Fusion FX7	Vilber Lourmat
Oven Thermocenter TC 40/100	Salvis Lab
Overhead shaker Reax 2	Heidolph
PCR machine PTC-200	MJ Research
pH-electrode BlueLine	Schott Instruments
pH-meter Lab 850	Schott Instruments
Pipettor Pipetboy	Integra
Plate reader Multiskan RC	Thermo Lab Systems
Power supply Power Pac 200	BioRad
Power supply Power Pac 300	BioRad
Power supply Power Pac HC	BioRad
Precision analytical balance ALC-80.4	Acculab
Rotator 2-1175	neoLab
Shaker ST 5	Ingenieurbüro CAT
Spectrophotometer Nanodrop ND-1000	peqlab
Thermo shaker MKR 23	HLC by Ditabis
Thermo shaker Thriller	peqlab
Thermo shaker Ts-100	Biosan

Ultracentrifuge Optima MAX-XP (TLA-55 rotor)	Beckman Coulter
Vacuum pump BVC 21	Vacuubrand
Vacuum pump BVC control	Vacuubrand
Vortex Genie 2	Scientific Industries
Water bath 1005	GFL
Water purification system Milli-Q (Q-POD)	Millipore

15 ml Falcon	VWR
24-well cell culture dishes	BD Falcon
384-well Sensoplate plus, PS, glass bottom	Greiner Bio-One
50 ml Falcon	BD Falcon
6-well cell culture dishes	Omnilab
Biosphere filtertips, extralong (200 µl, 1250 µl)	Sarstedt
Cell culture flasks 25 cm^2	Sigma
Cell scraper	BD Bioscience
Centrifuge tubes 1.5 ml	Beckman Coulter
Coverslips, round ∅ 18 mm	Thermo Scientific
Filtertips 10 µl (0.1 - 10 µl) G short	peqlab
Filtertips 10 µl (0.5 - 10 µl) E long	peqlab
Microscope slide Menzel Gläser Superfrost Plus	Thermo Scientific
Multiflex Round Tips Pipettenspitzen 0.5- 200 µl	peqlab
Nunclon Surface Triple Flasks 500 cm^2	Nunc
PCR tubes flat cap 0.2 µl	peqlab
Protein LoBind Tubes (0.5 ml, 1.5 ml)	Eppendorf
SafeGuard Filtertips (0.1 - 10 µl G, 20 µl, 1000 µl)	peqlab
SafeGuard Filtertips (1-200 µl)	peqlab
Safe-Lock Tubes (0.5 ml, 1.5 ml; 2.0 ml)	Eppendorf
Sterile disposable pipettes (1 ml, 2 ml, 5 ml, 10 ml, 25 ml)	Sarstedt
Syringe Injekt-F 25G	Braun
TipOne 10 µl XL Graduated Tips	StarLab
TipOne 1000 µl Blue Graduated Tips	StarLab
TipOne 200 µl Yellow Bevelled Tips	StarLab
Tissue culture flasks T-80	Nunc

4.2 Chemicals

Acrylamide (Ultra Pure Proto Gel 30%)	National diagnostics

Agar	Invitrogen
Agarose	Sigma
Aluminium sulfate hydrate	Sigma
Ammonium persulfate (APS)	Sigma
Ampicillin	Sigma
Bovine serum albumin (BSA)	Sigma
Boric acid	Roth
Bromophenol blue	Sigma
Coomassie Brilliant Blue G250	Fluka
Dimethyl sulfoxide (DMSO)	Merck
Deoxycholic acid (DOC)	Sigma
Dithiothreitol (DTT)	Sigma
Ethylenediaminetetraacetic acid (EDTA)	Roth
Ethanol	Merck
Glycerol	Roth
Glycine	Merck
Double distilled water (H_2O_{bidest})	generated with MiliQ purification system
HCl	Roth
K_2HPO_4	Merck
KCl	Merck
Methanol	Merck
Mowiol 4-88	Roth
NaCl	Roth
NaH_2HPO_4	Roth
NaN_3	Merck
NH_3	Merck
NP-40	Fluka
Orange G	Sigma
Ortho-phosphoric acid	Roth
Paraformaldehyde (PFA)	Roth
Peptone from Casein	Serva
Skim milk powder	Fluka
Sodium dodecyl sulfate (SDS)	Serva
Sodium bicarbonate	Sigma
Tetramethyletylenediamine (TEMED)	Bio-Rad
Tris(hydroxymethyl)aminoethane (Tris), Trizma® base	Sigma
Tris HCl	Roth

Triton X-100	Sigma
Tween-20	Merck
Xylene Cyanole	ICN
Yeast extract	Roth

4.3 DNA methods

4.3.1 Plasmids

In Table 4.3 all plasmids are listed that were used in this thesis. Table 4.4 shows details of the plasmids constructed in this thesis.

Table 4.3: List of plasmids. Details about vectors and inserts as well as sources/references (Ref.) of each plasmid are given. (1) a kind gift of Y. Durocher (National Research Council, Quebec, Canada), (2) Promega, (3) Duering et al. [71], (4) Table 4.4 in this thesis.

Name	Description	Ref.
pTT5	high yield mammalian protein expression vector	(1)
pFC14A Halo-Tag	mammalian protein expression vector	(2)
pTT5/hN3-EGF1-5-wt-myc	encodes hNotch3 EGF1-5 wt fused to a myc-His tag	(3)
pTT5/hN3-EGF1-5-75-myc	contains the mutation R75P in human Notch3	(4)
pTT5/hN3-EGF1-5-133-myc	contains the mutation R133C in human Notch3	(3)
pTT5/hN3-EGF1-5-183-myc	contains the mutation C183R in human Notch3	(3)
pTT5/hN3-EGF1-5-212-myc	contains the mutation C212Y in human Notch3	(4)
pTT5/hN3-EGF1-5-213-myc	contains the mutation R213K in human Notch3	(4)
pFC14A/hN3-EGF1-5-wt-Halo	encodes hNotch3 EGF1-5 wt fused to a HaloTag	(4)
pTT5/hN3-EGF1-5-wt-Halo	encodes hNotch3 EGF1-5 wt fused to a HaloTag	(4)
pTT5/hN3-EGF1-5-del-Halo	contains the deletion 88AGRV91 in human Notch3	(4)
pTT/hN3-EGF1-5-61-Halo	contains the mutation R61W in human Notch3	(4)
pTT/hN3-EGF1-5-75-Halo	contains the mutation R75P in human Notch3	(4)
pTT/hN3-EGF1-5-80-Halo	contains the mutation D80G in human Notch3	(4)
pTT/hN3-EGF1-5-113-Halo	contains the mutation R113Q in human Notch3	(4)
pTT/hN3-EGF1-5-133-Halo	contains the mutation R133C in human Notch3	(4)
pTT/hN3-EGF1-5-170-Halo	contains the mutation H170R in human Notch3	(4)
pTT/hN3-EGF1-5-179-Halo	contains the mutation G179V in human Notch3	(4)
pTT/hN3-EGF1-5-183-Halo	contains the mutation C183R in human Notch3	(4)
pTT/hN3-EGF1-5-212-Halo	contains the mutation C212Y in human Notch3	(4)
pTT/hN3-EGF1-5-213-Halo	contains the mutation R213K in human Notch3	(4)

Table 4.4: DNA constructs generated in this thesis. Primers (Table 4.5)/inserts, templates and restriction sites for used constructs are listed. Methods used for construct generation are described in section 4.3.3. Polymerase chain reaction (PCR) performed according to the manufacturer's protocol. (SM) site-directed mutagenesis PCR, (SMK) QuikChange Lightning Site-Directed Mutagenesis Kit (Agilent): , (SC) sub-cloning: inserts were cut out from template and inserted into the new vector, (S) standard PCR, (LD) loop-deletion PCR, * performed by Caroline Prell (Institute for stroke and dementia research (ISD), Munich, Germany).

Name	**Primers or inserts**	**Template**	**Restriction enzymes**	**Generation**
pTT5/hN3-EGF1-5-75-myc	N3-65-F/R75P-R, N3-430-R	pTT5/hN3-EGF1-5-wt-myc	BbvCI/NheI	(SM) *
pTT5/hN3-EGF1-5-212-myc	N3-C212Y-F/N3-C212Y-R	pTT5/hN3-EGF1-5-wt-myc	—	(SMK) *
pTT5/hN3-EGF1-5-213-myc	R213K-F/N3-739-R, N3-351-F	pTT5/hN3-EGF1-5-wt-myc	BbvCI/XbaI	(SM) *
pFC14A/hN3-EGF1-5-wt-Halo	SP+AsiSI-F/EGF5+XhoI-R	pTT5/EGF1-5-wt-myc	AsiSI/XhoI	(S)
pTT5/hN3-EGF1-5-wt-Halo	Halo-F/Halo-R	pFC14A	AgeI/XbaI	(S)
pTT5/hN3-EGF1-5-del-Halo	del-1,3-F/del-1-R, del-2-F/del-2,3-R	pTT5/hN3-EGF1-5-wt-Halo	NaeI/XbaI	(LD)
pTT/hN3-EGF1-5-61-Halo	113-1-F/61-1-R, 113-2-R	pTT5/hN3-EGF1-5-wt-Halo	NheI/SbfI	(SM)
pTT5/hN3-EGF1-5-75-Halo	hN3 EGF1-5 R75P	pTT5/hN3-EGF1-5-75-myc	SpeI/XbaI	(SC)
pTT5/hN3-EGF1-5-80-Halo	113-1-F/80-1-R, 113-2-R	pTT5/hN3-EGF1-5-wt-Halo	NheI/SbfI	(SM)
pTT5/hN3-EGF1-5-113-Halo	113-1-F/113-1-R, 113-2-R	pTT5/hN3-EGF1-5-wt-Halo	NheI/SbfI	(SM)
pTT5/hN3-EGF1-5-133-Halo	hN3 EGF1-5 R133C	pTT5/hN3-EGF1-5-133-myc	SpeI/XbaI	(SC)
pTT/hN3-EGF1-5-170-Halo	170-1-F/170-1-R, 170-2-R	pTT5/hN3-EGF1-5-wt-Halo	BbvCI/XbaI	(SM)
pTT5/hN3-EGF1-5-179-Halo	170-1-F/179-1-R, 170-2-R	pTT5/hN3-EGF1-5-wt-Halo	BbvCI/XbaI	(SM)
pTT5/hN3-EGF1-5-212-Halo	hN3 EGF1-5 C212Y	pTT5/hN3-EGF1-5-212-myc	SpeI/XbaI	(SC)
pTT5/hN3-EGF1-5-213-Halo	hN3 EGF1-5 R213K	pTT5/hN3-EGF1-5-213-myc	SpeI/XbaI	(SC)

4.3.2 Oligonucleotides

Table 4.5 lists the oligonucleotides used for PCR.

Table 4.5: List of oligonucleotides Mutations for site-directed mutagenesis PCR are marked in red. All oligonucleotides were designed with CLC Main Workbench and manufactured by Metabion, Martinsried, Germany.

Name	Sequence
N3-65-F	5'-CACCCGTGCGGGCGCT-3'
R75P-R	5'-CTGACACGGCTCACCC-3'
N3-C212Y-F	5'-ACGGGGGCACCTACAGGCAGAGTGG-3'
N3-C212Y-R	5'-CCACTCTGCCTGTAGGTGCCCCCGT-3'
R213K-F	5'-ACCTGCAAGCAGAGTG-3'
N3-739-R	5'-TGAGTTTTTGTTCGAAGGG-3'
N-351-F	5'-CTCCCTGCCAGATCCCTG-3'
SP+AsiSI-F	5'-ACATCCGGCGATCGCGTTCAGCCTGGTTAAGTC-3'
EGF5+XhoI-R	5'-CTATCCGCTCGAGTTCACAATTCTGACCCTCAAAC-3'
Halo-F	5'-ATCGCTCTAGACCAACCACTGAGGATCTG-3'
Halo-R	5'-CTAGCACCGGTCTATTAACCGGAAATCTCC-3'
del1,3-F	5'-CATCCACTTTGCCTTTCTCTCC-3'
del-1-R	5'-CTGGCAGACACAGGGGCCTGAGTGAC-3'
del-2-F	5'-CCCCTGTGTCTGCCAGAGTTCAGTGG-3'
del-2,3-R	5'-TAGGAGGAGGTCGGGTTACC-3'
61-1-R	5'-CTCCCAGGAGGGCAGCTG-3'
80-1-R	5'-ACAGGGGCCCTCCAGCTG-3'
113-1-F	5'-CCCTGCTGCTGCTGCTAG-3'
113-1-R	5'-AGCAGTCAGGGCCTTGGAAGCCA-3'
113-2-R	5'-ACACGTTCACTTCACAATTCTGACCCTCAA-3'
170-1-F	5'-ATTCTCATGCCGGTGCCC-3'
170-1-R	5'-ACCACGGCGGCAGGGCTCAC-3'
170-2-R	5'-ACGTAGGAGGAGGTCGGGTTACCGTGCAGGAACA-3'
179-1-R	5'-CGGAAGGAGACAGGTGTGTT-3'

4.3.3 PCR

Standard PCR

Standard PCR was performed to amplify a certain DNA sequence using the following components (Table 4.6):

Table 4.6: Standard PCR reaction mix

Component	Volume
native Pfu polymerase buffer (10x)	5 µl
Q-solution (5x) (Quiagen)	10 µl
template (100 ng/µl)	0.5 µl
dNTP-mix (10 µM)	1 µl
forward primer (10 µM)	2.5 µl
reverse primer (10 µM)	2.5 µl
native Pfu polymerase	1 µl
Taq polymerase	0.1 µl
H_2O_{bidest}	ad 50 µl

All components were pipetted on ice. Reaction was performed in a Thermocycler using the following program (Table 4.7):

Table 4.7: PCR program. Annealing temperature depends on primer pair that was used.

Step	Temperature	Periode
Denaturation	94°C	3 min
30 cycles:		
Denaturation	94°C	30 sec
Annealing	52 – 62°C	1 min
Elongation	72°C	1 min/1000 bp
Elongation	72°C	10 min
Storage	4°C	∞

PCR products were purified using the QIAquick PCR Purification Kit (Qiagen) according to the manufacturer's protocol.

Site-directed mutagenesis PCR

Mutations were inserted within the first PCR step (Table 4.6 and Table 4.7), whereas one primer contains the desired point mutation. After purification of the first PCR product (see section 4.3.4) this fragment served as megaprimer for the second PCR step, which finally includes an appropriate restriction site. Final concentration of the megaprimer used for the second step was 0.2 µM.

Loop-deletion PCR

Two PCR steps were performed to amplify the 5' and the 3' end of the desired fragment with primers containing an internal overlap after the deletion. After purification (see section 4.3.5) both PCR products served as template for the third PCR step.

4.3.4 Agarose gel electrophoresis

TBE-Buffer:
89 mM Tris, 89 mM boric acid, 2 mM EDTA, pH 8.0

Agarose gels:
0.5-2% (w/V) agarose melted in TBE-Buffer, 1:10000 SYBR$^{\text{textregistered}}$ Safe DNA Gel Stain (Invitrogen)

DNA loading buffer (6x):
60% glycerol, 10 mM Tris HCl, 60 mM EDTA, 0.025% (w/v) Xylene Cyanol, 0.025% (w/v) Orange G, pH 7.6

DNA was separated in 0.5-2% agarose gels, depending on the desired fragment sizes. Electrophoresis was performed in TBE-buffer using the PerfectBlue gelsystems (peqlab) with a constant voltage of 80 V (small chamber) or 100 V (large chamber). As molecular marker, PeqGOLD 50 bp DNA ladder (up to 1 kb, peqlab) or PeqGOLD DNA ladder mix (up to 10 kb, peqlab) was used respectively.

4.3.5 DNA restriction

Preparative restriction for subsequent ligation (see section 4.3.7) contains the following components (Table 4.8.)

Table 4.8: Preparative DNA restriction. Used restriction enzymes are listed in Table 4.4, column Restriction. All enzymes are purchased from NEB. Appropriate restriction enzyme buffer for double digestion was evaluated by the NEB homepage (`https://www.neb.com/tools-and-resources/interactive-tools/double-digest-finder`).

Component	Amount
restriction enzyme 1	10 U
restriction enzyme 2	10 U
DNA	1 µg
BSA 10x (opt.)	2 µl
Restriction enzyme buffer 10x	2 µl
H_2O_{bidest}	ad 20 µl

New ligated plasmids were analyzed for correct insertion by analytic restriction using the following reaction mix (Table 4.9).

Table 4.9: Analytic DNA restriction.

Component	Amount
restriction enzyme 1	5 U
restriction enzyme 2	5 U
DNA	0.5 µg
BSA 10x (opt.)	2 µl
Restriction enzyme buffer 10x	2 µl
H_2O_{bidest}	ad 20 µl

Mixtures were incubated for 1h at 37°C. Restriction enzymes were, if recommended, heat inactivated at 65°C for 30 min. PCR fragments were isolated with agarose gel electrophoresis (see section 4.3.4), excised and purified with the GeneJET Gel Extraction Kit (Fermentas) according to the manufacturer's protocol .

4.3.6 Vector dephosphorylation

To avoid religation, vector DNA was dephosporylated adding 1 µl Antarctic phosphatase (NEB), 3 µl Antarctic phosphatase buffer and 6 µl H_2O_{bidest} to the DNA restriction mix (see section 4.3.5) and incubated for 30 min at 37°C.

4.3.7 Ligation

50 ng of vector was mixed with a threefold excess of insert, 1 µl T4 DNA ligase (NEB), 2 µl ligase buffer and H_2O_{bidest} up to a volume of 20 µl. The mixture was incubated for 1 h at room temperature (RT).

4.3.8 Transformation of competent bacteria

Lysogeny broth medium (LB medium):
1% (w/v) peptone, 0.5% (w/v) yeast extract, 0.5% (w/v) NaCl, pH 7.0

LB_{amp} medium:
LB medium, 100 µg/ml ampicillin

LB_{amp} agar plates:
LB_{amp} medium, 1.5% (w/v) agar

2 µl of ligation mix or 100 ng of DNA plasmid to be amplified was added to competent *E.coli* (DH5α) respectively. Bacteria were incubated on ice for 30 min, heat shocked at 42°C for 90 sec and kept on ice for another 2 min. 300 µl LB medium were added and bacteria suspension shaken for 1 h at 37°C. Bacteria were plated on LB_{amp} agar plates and incubated o/n at 37°C. Colonies were picked and inoculated in fresh LB_{AMP} medium,

volume depending on the plasmid isolation method (see section 4.3.9) and cultivated o/n at 37°C shaking at 230 rpm.

4.3.9 DNA isolation

For small-scale DNA isolation, transformed bacteria (see section 4.3.8) were grown in 4 mL LB_{amp} medium o/n. Plasmids were isolated using the NucleoSpin Plasmid kit (Macherey-Nagel) according to the manufacturer's protocol. Large amount of plasmids were isolated from 300 ml o/n culture in LB_{amp} using the NucleoBond Xtra Midi kit (Macherey-Nagel) according to the manufacturer's protocol. DNA concentration was measured with NanoDrop ND-1000 (peqlab). Plasmid isolation control was done by test restriction using the appropriate restriction enzymes (see section 4.3.5) and subsequent agarose gel electrophoresis (see section 4.3.4). DNA was sent for sequencing to GATC Biotech AG (Konstanz, Germany).

4.4 Cell culture

4.4.1 Cell lines

Table 4.10: Cell lines. Sources: (1) Y. Durocher (National research Council, Quebec, Canada), (2) Eva Scharrer (ISD, Munich, Germany), isolated from 14.5-dpc embryos of C57BL/6J mice, immortalized through serial passaging

Cell line	Description	Source
HEK293E	human embryonic kidney cells	(1)
wt1o	mouse embryonic fibroblasts	(2)
wt2o	mouse embryonic fibroblasts	(2)
wt1	mouse embryonic fibroblasts	(2)
wt3	mouse embryonic fibroblasts	(2)
wt4	mouse embryonic fibroblasts	(2)

4.4.2 Cell cultivation

Phosphate buffered saline (PBS):
154 mM NaCl, 9.5 mM NaH_2HPO_4 x 2 H_2O, 1.7 mM K_2HPO_4, pH 7.4

0.05% Trypsin-EDTA 1x (Gibco, Life Technologies)

Medium:
Dulbecco's Modified Eagle Medium (DMEM) High Glucose GlutaMAX^{TM} Supplement, pyruvate (Gibco, Life Technologies)

Supplements:
Fetal bovine serum (FBS) (Gibco, Life Technologies)
penicillin/streptomycin solution (p/s) (100 U/ml penicillin, 100 µg/ml streptomycin) (Gibco, Life Technologies)
25 µg/ml G418 sulfate, geneticin (G418) (Merck)

Cells were cultured in DMEM supplemented with 10% FBS at 37°C in the presence of 5% CO_2. To HEK293E medium G418 was added for selection. MEFs were kept with p/s. For passaging, cells were washed with PBS and trypsinized for 3 min. Trypsin was inactivated by adding fresh medium. Cells were centrifuged for 7 min at 400 g. Cell pellet was resuspended and an appropriate amount of cells were seeded in fresh medium. Cells were tested for mycoplasma on regular basis using the Venor GeM OneStep kit (Minerva Biolabs) or the MycoAlert™ PLUS Mycoplasma Detection Kit (Lonza).

4.4.3 Cell transfection

Polyethylenimine (PEI) transfection

HEK293E cells were cultivated until a confluence of 70%. Standard medium (see section 4.4.2) was changed to DMEM with 2.5% FBS. DNA was mixed with OptiMEM (Gibco, Life Technologies) and PEI (Polysciences Europe) was added subsequently. Amounts of all components are listed in Table 4.11. Transfection mix was incubated for 25 min at RT and added to the cells. Tranfection medium was changed 24 h later to DMEM.

Table 4.11: Tranfection mixtures for PEI.

Culture dish	Medium	DNA	PEI (1mg/mL)	OptiMEM
6-well	1 ml	2 µg	8 µl	ad 200 µl
T-80 flask	10 ml	12 µg	48 µl	ad 1.2 ml
500 cm^2 flask	90 ml	75 µg	300 µl	ad 3 ml

Lipofectamine2000 transfection

MEF cells were seeded to reach 90% confluency the day of transfection. Then medium was changed to DMEM with 10% FBS. First, DNA and Lipofectamine 2000 (Life Technologies) were mixed separately with OptiMEM and incubated for 5 min at RT. Amounts of all components are listed in Table 4.12. Both mixtures were combined and further incubated for 20 min at RT and added to the cells. Transfection medium was changed 5 h later to DMEM with 10% FBS and p/s .

Table 4.12: Tranfection mixtures for Lipofectamine 2000.

Culture dish	Cells	OptiMEM	DNA	Lipofectamine 2000	
24-well	$0.5x10^5$	500 µl	2x 25 µl	0.5 µg	2 µl
6-well	$2.5x10^5$	2 ml	2x 100 µl	2.5 µg	10 µl
T-80 flask	$2x10^6$	10 ml	2x 750 µl	25 µg	80 µl

4.4.4 Cryoconservation

Freezing medium:
FBS with 10% DMSO

Cells were passaged (see section 4.4.2). Pellet was resuspended in an appropriate volume of freezing medium, transferred into a freezing container, slowly frozen o/n at −80°C and finally transferred into a liquid-nitrogen tank.

4.5 Protein analysis

4.5.1 Antibodies

All antibodies used in this work are listed in Table 4.13 and Table 4.14.

Table 4.13: List of primary antibodies. IB: immunoblot, IF: immunfluorescence; the monoclonal anti-Notch3 (3G6) antibody was raised against the peptide sequence ^{129}AHGARCSVGPDGRFLCSC^{146} of human Notch3.

Antibody	Type	Application	Source
anti-Fibronectin (FN-3E2)	mouse monoclonal	IB 1:1000	Sigma
anti-Fibronectin (N-20)	goat polyclonal	IF 1:100	Santa Cruz
anti-myc (9E10)	mouse monoclonal	IB 1:4000	Hybridoma Bank,Iowa, USA
		IF 1:1000	
anti-Notch3 (3G6)	rat monoclonal	IB 1:2000	E.Kremmer, Helmholtz Zentrum,
anti-PDGFRβ	goat polyclonal	IB 1:5000	R&D
anti-Tubulin (2-28-33)	mouse monoclonal	IB 1:2000	Sigma

Table 4.14: List of secondary antibodies. Secondary antibodies for immunoblots were used in a 1:10000 dilution, for immunofluorescence in a 1:100 dilution. Horseradish peroxidase (HRP)

Antibody	Coupled to	Source
goat anti-mouse	HRP	Dako
rabbit anti-goat	HRP	Jackson
rabbit anti-rat	HRP	Dako
donkey anti-goat	Rhodamine Red-x	Jackson
donkey anti-mouse	Cy2	Jackson

4.5.2 Total protein lysate

PBS:
154 mM NaCl, 9.5 mM NaH_2HPO_4 x 2 H_2O, 1.7 mM K_2HPO_4, pH 7.4

10x protease inhibitor (PI):
1 complete protease inhibitor cocktail EDTA-free tablet (Roche) in 1 ml H_2O_{bidest}

Tris-HCl, NaCl, Tween (TNT) lysis buffer:
50 mM Tris-HCl, 200 mM NaCl, 0.5% NP-40, 1x PI, pH 8.0

24 h after PEI-transfection of HEK293E cells in 6-well culture dishes (see section 4.4.3) medium was changed to 1 ml DMEM without FBS. At indicated time points, conditioned medium was taken off for analysis and centrifuged for 5 min at 1000 g to remove dead cells. Cells were washed with PBS and resuspended in 1 ml PBS. Cell resuspension was centrifuged for 5 min at 1000 g, supernatant was removed and cell pellet was lysed in 100 µl TNT lysis buffer and incubated on ice for 20 min. Cell debris was removed by centrifugation for 30 min at 14000 g and 4°C. Protein concentration was measured using the BCA Protein Assay Kit (Thermo Scientific Pierce) according to the manufacturer's standard protocol. Briefly, 10 µl of BSA standard or (diluted) sample were mixed with 80 µl of working solution in a 96-well reaction plate (peqlab) and incubated for 30 min at 37°C. Absorbance at 562 nm was measured with a Multiscan RC plate reader (Thermo Labsystems). Standards and samples were measured in duplicates.

4.5.3 Matrix isolation

PBS:
154 mM NaCl, 9.5 mM NaH_2HPO_4 x 2 H_2O, 1.7 mM K_2HPO_4, pH 7.4

10x PI:
1 complete protease inhibitor cocktail EDTA-free tablet (Roche) in 1 ml H_2O_{bidest}

Buffer M1:
0.1% Triton, 20 mM NH_3, 1x PI in PBS

Buffer M2:
10 mM Tris, 150 mM Nacl, 0.5% DOC, pH 7.5

Buffer M3:
2 mM Tris pH 7.5

Buffer M4:
10 mM Tris, 150 mM Nacl, 1% SDS, pH 7.5

MEFs were grown in 6-well culture dishes for 2 days after transfection (see section 4.4.3). Then medium was changed to DMEM without FBS. Another 3 days later conditioned medium was removed for analysis and centrifuged for 5 min at 1000 g to remove dead cells. Cells were washed with PBS and cell bodies were lysed with 500 µl buffer M1 at RT by slowly shaking the wells. Cell lysates were carefully taken off and centrifuged at 16,000 g for 30 min at 4°C to remove cell debris. Meanwhile, wells were cleared from cell debris and nuclei by washing with 500 µl buffer M2 for 10 min at 4°C and shortly with 500 µl hypotonic buffer M3. ECM was recovered in 250 µl buffer M4 using a cell scraper for removing everything from the wells and homogenized by passing the samples several times through a 25G syringe. Protein concentration of the M4 fraction was measured using the BCA Protein Assay Kit (Thermo Scientific Pierce) according to the manufacturer's enhanced protocol. Different to the procedure described in section 4.5.2, the enhanced BSA standard was used and the samples were incubated at 60°C for 30 min.

4.5.4 Protein purification

PBS:
154 mM NaCl, 9.5 mM NaH_2HPO_4 x 2 H_2O, 1.7 mM K_2HPO_4, pH 7.4

Washing solution:
2% sodium bicarbonate, 1 mM EDTA

Dialysis buffer 1:
0.5x PBS

Dialysis buffer 2:
0.5x PBS, 200 mM NaCl

Purification buffer:
PBS, 0.01% NP-40

Cleavage solution:
60 µl TEV protease (Promega) in 1 ml purification buffer

Protein purification was performed with the components of the HaloTag Protein Purification System (Promega) using a modified protocol. For purification control, an aliquot was collected after each step.

HEK293E cells were cultured and transfected in 4x 500 cm^2 flasks (see section 4.4.3). 24 h after tranfection medium was changed to 90 ml DMEM without FBS per flask. 5 days later medium was collected and centrifuged for 5 min at 1000 g to remove dead cells. 45 cm of Visking dialysis tubings (Type 27/32 inch, Roth) for each cell flask were washed in 80°C washing solution for 30 min and rinsed with clear water afterward. Medium was dialyzed against dialysis buffer 1 for 2x 2 h at RT and subsequently against dialysis buffer 2 for 3x 1-2 h at 4°C. Meanwhile, 3 ml of thoroughly resuspended HaloLink Resin (375 µl per 90 ml medium of one flask) was spun at 1000 g for 5 min at RT. Supernatant was discarded

and settled beads were equilibrated washing 3 times with 10 ml purification buffer and subsequent centrifugation at 1000 g for 5 min at RT. Finally, beads were resuspended in the original volume of 3 ml. Medium was portioned into 50 mL falcons, supplemented with 0.01% NP-40 and HaloLink Resin was distributed equally to the falcons. Medium/beads suspension was mixed o/n on a end-over-end tube rotator at 4°C. The next day beads were centrifuged for 5 min at 1000 g and supernatant was discarded. Beads were washed three times with 10 ml purification buffer and subsequently centrifuged for 5 min at 1000 g. Settled beads were resuspended in 1 ml cleavage solution containing TEV protease. Suspension was incubated for 1 h at RT on a turning wheel. Beads were centrifuged for 5 min at 1000 g and supernatant was collected. Beads were washed with 1 ml purification buffer, centrifuged again for 5 min at 1000 g and supernatant was collected and pooled with the former supernatant. To remove the TEV protease 50 µl HisLink Resin was added and suspension was incubated for 30 min at RT on a turning wheel. Beads were centrifuged for 5 min at 1000 g and protein solution was collected in LoBind tubes. Beads were washed with 100 µl purification solution, spun again at 1000 g for 5 min and second fraction was collected containing remaining protein. Protein concentration of both fractions was determined using the BCA Protein Assay Kit (Thermo Scientific Pierce) according to the manufacturer's enhanced protocol (as described in section 4.5.3).

4.5.5 SDS-PAGE

4x Lower-Tris buffer:
1.5 M Tris, 0.4% SDS in H_2O_{bidest}, pH 8.8

4x Upper-Tris buffer:
0.5 M Tris, 0.4% (w/v) SDS in H_2O_{bidest}, 6.8

1x Running buffer:
25 mM Tris, 192 mM glycine, 1% (w/v) SDS in H_2O_{bidest}

5x Loading buffer:
375 mM Tris, 30% glycerol, 6% (w/v) SDS, 500 mM DTT, 0.03% (w/v) bromophenol blue in H_2O_{bidest}, pH 6.8

SDS-polyacrylamide gel electrophoresis (PAGE) was performed under denaturing and reducing conditions with the Mini Format Electrophoresis System (Bio-Rad). Gels were prepared due to the discontinous system. Composition of stacking and separation gels is shown in Table 4.15.

Protein samples were mixed with 5x loading buffer and boiled for 5 min at 95°C, except ECM samples in buffer M4 (see section 4.5.3). To prevent aggregation of matrix proteins, ECMsamples were incubated for 30 min at 45°C. Samples were run together with the Precision Plus Protein Standard All Blue (Bio-Rad) as molecular weight marker. Electrophoresis was carried out at constant 80 V, followed by constant 120 V once proteins were migrated into the separating gel. For protein detection, gels were first stained with Imperial Protein Stain (Thermo Fischer) and afterwards with Roti-Black P (Roth) for silver staining, both according to the manufacturer's protocol.

Table 4.15: Composition of separating and stacking SDS polyacrylamide gels. Volumes indicated are sufficient for 2 1.0 mm thick mini-gels.

Solution	5% Separating gel	10% Separating gel	Stacking gel
4x Lower-Tris buffer	3 ml	3 ml	
4x Upper-Tris buffer			1.02 ml
H_2O_{bidest}	6.88 ml	4.88 ml	2.94 ml
Acrylamide	2 ml	4 ml	0.56 ml
TEMED	10 µl	10 µL	4.5 µl
10% APS	100 µl	100 µl	45 µl

4.5.6 Western blot

1x Transfer buffer:
125 mM Tris, 1 M glycine, 20% methanol

Coomassie brilliant blue (CBB)-solution:
5% (w/v) Aluminium sulfate hydrate, 10% ethanol, 0.02% (w/v) Coomassie Brilliant Blue G250, 2% ortho-phosporic acid

1x TBS-T buffer:
10 mM Tris, 150 mM NaCl, 0.05% Tween-20 in H_2O_{bidest}

Blocking solution:
4% (w/v) skim milk powder in 1x TBS-T buffer

PBS:
137 mM NaCl, 2.7 mM KCl, 10 mM Na_2HPO_4 x 2 H_2O, 2 mM KH_2PO_4, pH = 7.4

Proteins were transferred to a Immobilon-P Transfer polyvinylidene fluoride (PVDF) membrane (Milipore) using the Trans Blot SD semi dry transfer cell (Bio-Rad). PVDF membrane was activated shortly in 100% methanol and then washed with transfer buffer. SDS gel and membrane were stacked between extra thick blot paper (Bio-Rad) soaked with transfer buffer. Transfer was performed for 1 h at constant 125 mA per membrane. After transfer, membrane was stained with Ponceau-S solution (Sigma) and gel with CBB-solution for loading and transfer control. Membrane staining was partly removed washing with H_2O_{bidest} and membrane was blocked for 1 h in blocking solution. Blocked membrane was incubated with primary antibody diluted in blocking solution (see section 4.5.1) for 1 h at RT or o/n at 4°C, washed 3 times for 10 min with TBS-T and incubated for 1 h at RT with the appropriate secondary antibody conjugated to HRP (see section 4.5.1). Membrane was washed again 3 times for 10 min with TBS-T and 2 times with PBS. Immobilon Western (Millipore) was added on top of the membrane as chemiluminescent HRP substrate according to the manufacturer's protocol and signal was detected at the Fusion FX7 (Vilber-Lourmat).

4.5.7 Immunofluorescence

PBS:
154 mM NaCl, 9.5 mM NaH_2HPO_4 x 2 H_2O, 1.7 mM K_2HPO_4, pH 7.4

Fixation buffer:
4% PFA in PBS

Blocking solution:
1% BSA in PBS

Mowiol:
6 g glycerol, 2.4 g Mowiol 4-88, 6 mL H_2O_{bidest}, 12 mL 0.2 M Tris-HCl pH 8.5

MEFs were grown in 24-well dishes on coverslips for 2 days after transfection (see section 4.4.3). Then, medium was changed to 350 µl DMEM without FBS. Conditioned medium was removed after 3 days for Western blot analysis and centrifuged for 5 min at 1000 g to remove dead cells. Cells on coverslips were fixed for 10 min with fixation buffer, washed with PBS and blocked for 1 h at RT with blocking solution. Incubation with primary antibody diluted in blocking solution (see section 4.5.1) was performed for 1 h at RT or o/n at 4°C in a humid chamber. Coverslips were washed with PBS and incubated in secondary antibodies diluted in blocking solution for 1 h at RT. Coverslips were washed in PBS, incubated for 10 min at RT in PBS diluted 4'6-diamidino-2-phenylindole (DAPI) (1:4000), washed again with PBS, finally with H_2O_{bidest} and mounted with Mowiol on cover glas. Samples were analyzed with a fluorescent microscope Axiovert 200M (Zeiss).

4.6 Single molecule spectroscopy

4.6.1 Measurement setup

The setup of the Insight II Reader is comparable to a confocal microscope which directs the beams of two laser with different wavelengths into a focus of 1 fl and images the emitted photons of the excited fluorophores for each channel separately.

The exciting radiation is provided by an argon-laser with a wavelength of 488 nm and a helium-neon-laser with a wavelength of 633 nm. The beam of both lasers is initially combined in a dichroic mirror, passes through the optionally activated beam scanner unit and is focused by a water immersions objective with a high numerical aperture 150 µm above the glass bottom of a 384 well plate within the sample volume. The diameter of the Argon-laser focus is about 0.5 µm and is entirely projected within the 0.65 µm diameter of the Helium-Neon-laser.

The optionally activated beam scanner consists of a mirror set that oscillates with variable frequency and amplitude. In this work a frequency of 50 Hz and an amplitude of 100 µm was chosen. Additionally the plate was moved 2000 µm perpendicular to the oscillation direction by a microstep motor. Thus, the focus is scanning through the sample in a meander-like fashion with a resulting scanning speed of 10 mm/sec.

The emitted photons of the excited fluorescent dyes are collected by the same objective and passed through the first dichroic mirror, where the signal is separated from the laser beam. The following pinhole with a diameter of 70 µm blocks any fluorescent light not originating from the focal region, thus separating the signal from unspecific background. Finally the signal consisting of two different wavelengths is separated by another dichroic mirror and is detected by two separate APDs. The measured signal is transferred to a computer and can be analyzed with different programs (see section 4.6.3).

4.6.2 Reader adjustment

To gain constant and reproducible results, excitation intensity, focus size and pinhole position have to be adjusted before measurement. Excitation power of the Argon-laser was set to 200 µW, of the Helium-Neon-laser to 300 µW. As calibrator served a solution of unconjugated Alexa^{488}- and Alexa^{647} dye with known diffusion and emission properties. By means of a shiftable camera the laser focus was positioned 150 µm above the glass bottom of the plate. For an optimal focus laser fibers and pinhole position were adjusted with the help of the FCS+Plus_control software (Evotech). As adjustment parameter served counts per particle (CPP), indicating how many photons per particle can be detected. CPP values of $\geq$ 19 (488) and $\geq$ 11 (647) were pursued. With the measurement of the calibrator solution the diffusion time (τ_{diff}) for both dyes was determined, as an abnormal long diffusion time implies a diffuse focus. τ_{diff} values of 180 ms for Alexa^{488} and 300 ms for Alexa^{647} were pursued. The measurement time for all samples was set to 10 sec.

4.6.3 Evaluation methods

For measurement analysis the programs FCS+_Evaluation 2.0, pooling_NTPs_2Dfida and SIFT-2D (all Evotec) were available. These software packages allow different data evaluation:

FCS evaluation

Autocorrelation is a mathematical model to analyze noisy data. Noise is erased due to its random appearance, whereas particles diffusing through the stationary focus lead to a burst, an increase of the fluorescent signal. The measurement time is divided into small time windows of 50 ns, so called bins. Each bin can have the value 1 or 0 indicating if a photon was collected at this time window or not. Each time window is multiplied with another window of a certain distance, called correlation time. Correlation times vary from 50 ns (neighboring windows) up to the whole measurement time. The multiplications are summed up for each correlation time, normalized and plotted as a curve on a logarithmic

scale of the x-axis (Figure 4.1 A).In this way the autocorrelation allows a differentiation between a randomly distributed signal (value 0 for large correlation times) and a burst derived from a particle (value 1 for larger correlation times). With a mathematical fit of this curve (in Fig. 4.1 A depicted in red), a conclusion about up to four different particle species can be drawn. The quality of the fit is given in the parameter chi^2. Chi^2 is depicted in a residual curve, ideally randomly distributed around the x-axis (Fig. 4.1 B). τ_{diff} is defined as the correlation time at which half the maximal value is reached. Fitting more components gives the percentage of all molecules with a certain diffusion time. Details about the particle concentration gives the total intensity (I_{tot}) in kHz, directly derived from the measurement of the APDs, whereas the particle number N is equivalent to the inverse amplitude of the FCS curve after normalization.[116] FCS evaluation was used for reader adjustment (see section 4.6.2) and purity determination of labeled proteins (see section 4.6.4).

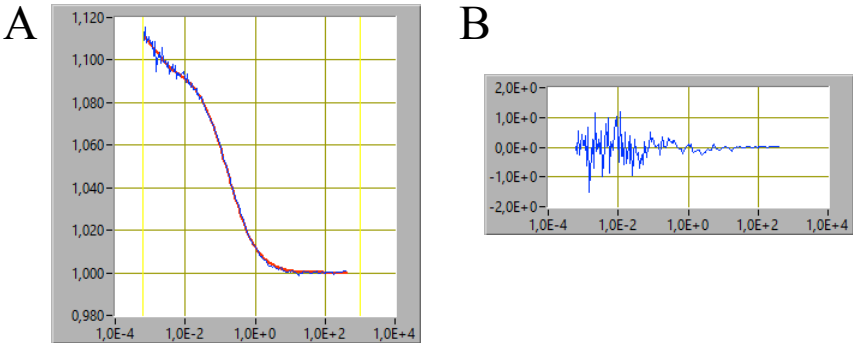

Figure 4.1: FCS curve of a pure dye solution A) Autocorrelation curve of the Alexa^{488} dye. Logarithmic x-axis depicts the correlation times in ms, y-axis the sum over the multiplications for each correlation time. B) Residual curve of the quality parameter chi^2.

SIFT-2D

The SIFT-2D analysis is using the fluorescence intensity distribution analysis (FIDA) data from both channels and generates a 2D histogram with $[\text{photons/bin}]_{488}$ on the x-axis and $[\text{photons/bin}]_{647}$ on the y-axis. The color-coded z-axis depicts the number of events particles of specific size and color passing the focus. In this histogram small monomeric particles are located at the origin, mono-colored multimers along the axes and dual-colored multimers in the middle part of the histogram. For quantification of the data, the histogram is split into 9 equal segments and the photons per segment are summed up. Mono-colored multimers, appearing at the histogram edge in segment 1 and 9, as well as the monomeric fraction, within an appropriate threshold at the lower left corner, are excluded from the quantification. The number of highly intense bins is direct proportional to the number of large aggregates. At the same time the composition of the aggregates can be concluded from the the position of the dual-colored aggregates relative to the axes.

Repeated measurements of the same sample (in one well) can be pooled with the pooling_NTPs_2Dfida program.

4.6.4 Fluorescent protein labeling

Protein storage buffer:
50 mM Tris pH 7.5

For fluorescent labeling, purified proteins (see section 4.5.4) were concentrated up to 100 µM. For this purpose, Amicon Ultra-0.5 ml centrifugal filter devices (3 kDa cutoff, Millipore) were incubated for 2 h in H_2O_{bidest} with 1.4 % NP-40 at RT, washed with H_2O_{bidest} and equilibrated with PBS. Proteins were thawed on ice and concentrated according to the manufacturer's protocol. Protein solution was divided into two equivalent volumes. Fractions were labeled either with $Alexa^{488}$ or $Alexa^{647}$ (Table 4.16). Dyes were added at 3-fold excess in 100 mM sodium bicarbonate buffer (pH 8.5). Mix was incubated o/n at 4°C. Afterward, unbound fluorophores were removed by repeated gelfiltration using Zeba Spin Desalting Columns (Thermo Fisher) according to the manufacturer's protocol until $\leq$ 40% of the free dye was reached. Purity was checked with FCS measurements (see section 4.6.3). During gelfiltration buffer was changed to 50 mM Tris buffer (pH 7.5). Labeling efficiency was checked via proteinase K digestion to ensure equal load of fluorophores for all constructs. Protein samples were incubated with 200 µg/ml proteinase K for 1 h at 37°C. The increase of particles in the FCS measurement compared to the non-digested sample is directly proportional to the label rate of the protein. Typical labeling rates were 3 fluorophores/molecule. Proteins were aliquoted, frozen in liquid nitrogen and stored at −80°C.

Table 4.16: List of fluorescent dyes. Dyes were dissolved in 100% DMSO

Abbreviation	Dye	Stock concentration	Source
$Alexa^{488}$	Alexa Fluor-488-O-Succinimidylester	3.2 mM	Molecular Probes (Eugene, USA)
$Alexa^{647}$	Alexa Fluor-647-O-Succinimidylester	1.6 mM	Molecular Probes (Eugene, USA)

4.6.5 Incubation experiments

SIFT buffer: 50 mM Tris, 1 complete protease inhibitor cocktail EDTA-free tablet (Roche), 0.1% NaN_3, pH 7.5,

Protein samples were thawed on ice, resuspended in 100 µl SIFT buffer and centrifuged at 60,000 g for 30 min at 4°C. 70 µl supernatant was transferred to a new LoBind tube. Concentration of proteins were adjusted to an I_{tot} of 1800 kHz (equivalent to ~80nM).

Proteins labeled with Alexa^{488} (green) were mixed with an equal amount of proteins labeled with Alexa^{647} (red). Samples were incubated at 37°C shaking at 500 rpm. For SIFT analysis at indicated time points, aliquots of the samples were diluted 1:7 into a 384-well measurement plate and measured immediately with the Insight II Reader. Samples were measured as triplicates with 5 repeats per well.

Synthetic compounds were selected from a compound library[98] and were used with kind permission of Armin Giese (Zentrum für Neuropathologie und Prionenforschung, Munich, Germany). Natural polyphenolic compounds were obtaind as a kind gift from Neville Vassallo (University of Malta)[96]. All compounds were stored in 100% DMSO and applied to the sample in a final concentration of 1% DMSO. Compounds were used at a final concentration of 10 µM if not indicated differently.

4.6.6 Statistical analysis

Data generated with SIFT analysis were represented as mean values with SEM. Mann-Whitney test was used for group statistics. For SIFT analysis of different Notch3 variants post hoc Wilcoxon signed-rank sum test with false discovery rate correction was used. Significance was indicated with asterisks: * $p<0.05$; ** $p<0.01$; *** $p<0.001$

Bibliography

[1] World Health Organization, *Dementia A public health priority*; 2012.

[2] World Health Organization, *The top 10 causes of death - Fact sheet No 310*; 2014.

[3] Warlow, C.; Sudlow, C.; Dennis, M.; Wardlaw, J.; Sandercock, P. Stroke. *Lancet* **2003**, *362*, 1211–24.

[4] Adams, H.; Adams, H.; Bendixen, B.; Bendixen, B.; Kappelle, L.; Kappelle, L.; Biller, J.; Biller, J.; Love, B.; Love, B.; Gordon, D.; Gordon, D.; Marsh, E.; Marsh, E. Classification of Subtype of Acute Ischemic Stroke. *Stroke* **1993**, *23*, 35–41.

[5] Pantoni, L. Cerebral small vessel disease: from pathogenesis and clinical characteristics to therapeutic challenges. *Lancet Neurology* **2010**, *9*, 689–701.

[6] Wardlaw, J. M.; Smith, C.; Dichgans, M. Mechanisms of sporadic cerebral small vessel disease: insights from neuroimaging. *Lancet neurology* **2013**, *12*, 483–97.

[7] Wardlaw, J. M.; Dennis, M. S.; Warlow, C. P.; Sandercock, P. A. Imaging appearance of the symptomatic perforating artery in patients with lacunar infarction: Occlusion or other vascular pathology? *Annals of Neurology* **2001**, *50*, 208–215.

[8] Goldstein, L. B.; Adams, R.; Alberts, M. J.; Appel, L. J.; Brass, L. M.; Bushnell, C. D.; Culebras, A.; DeGraba, T. J.; Gorelick, P. B.; Guyton, J. R.; Hart, R. G.; Howard, G.; Kelly-Hayes, M.; Nixon, J. V. I.; Sacco, R. L. *Stroke*; 2006; Vol. 11373; pp 1583–1633.

[9] Wardlaw, J. M.; Allerhand, M.; Doubal, F. N.; Morris, Z.; Gow, A. J.; Bastin, M. E.; Starr, J. M.; Dennis, M. S. Vascular risk factors , large-artery atheroma , and brain white matter hyperintensities. *Neurology* **2014**, *82*, 1331–1338.

[10] Joutel, A.; Corpechot, C.; Ducros, A.; Vahedi, K.; Chabriat, H.; Mouton, P.; Alamowitch, S.; Domenga, V.; Cécillion, M.; Marechal, E.; Maciazek, J.; Vayssiere, C.; Cruaud, C.; Cabanis, E. A.; Ruchoux, M. M.; Weissenbach, J.; Bach, J. F.; Bousser, M. G.; Tournier-Lasserve, E. Notch3 mutations in CADASIL, a hereditary adult-onset condition causing stroke and dementia. 1996.

[11] Chabriat, H.; Joutel, A.; Dichgans, M.; Tournier-Lasserve, E.; Bousser, M. G. Cadasil. *The Lancet Neurology* **2009**, *8*, 643–653.

[12] Stevens, D.; Hewlett, R. H.; Brownell, B. Chronic Familial Vascular Encephalopathy. *The Lancet* **1977**, *309*, 1364–1365.

[13] Sourander, P.; Walinder, J. Hereditary Multi-Infarct Dementia. *The Lancet* **1977**, *309*, 1015.

[14] Sonninen, V.; Savontaus, M. L. Hereditary multi-infarct dementia. *Eur Neurol* **1987**, *27*.

[15] Tournier-Lasserve, E.; Iba-Zizen, M. T.; Romero, N.; Bousser, M. G. Autosomal dominant syndrome with strokelike episodes and leukoencephalopathy. *Stroke* **1991**, *22*, 1297–302.

[16] Mas, J. L.; Dilouya, A.; de Recondo, J. A familial disorder with subcortical ischemic strokes, dementia, and leukoencephalopathy. *Neurology* **1992**, *42*, 1015–1019.

[17] Tournier-Lasserve, E.; Joutel, a.; Melki, J.; Weissenbach, J.; Lathrop, G. M.; Chabriat, H.; Mas, J. L.; Cabanis, E. a.; Baudrimont, M.; Maciazek, J. Cerebral autosomal dominant arteriopathy with subcortical infarcts and leukoencephalopathy maps to chromosome 19q12. *Nature genetics* **1993**, *3*, 256–259.

[18] Joutel, A.; Corpechot, C.; Ducros, A.; Vahedi, K.; Chabriat, H.; Mouton, P.; Alamowitch, S.; Domenga, V.; Cécillion, M.; Maréchal, E.; Maciazek, J.; Vayssière, C.; Cruaud, C.; Cabanis, E. A.; Ruchoux, M. M.; Weissenbach, J.; Bach, J. F.; Bousser, M. G.; Tournier-Lasserve, E. Notch3 mutations in cerebral autosomal dominant arteriopathy with subcortical infarcts and leukoencephalopathy (CADASIL), a mendelian condition causing stroke and vascular dementia. *Annals of the New York Academy of Sciences* **1997**, *826*, 213–217.

[19] Chabriat, H.; Tournier-Lasserve, E.; Vahedi, K.; Leys, D.; Joutel, A.; Nibbio, A.; Escaillas, J. P.; Iba-Zizen, M. T.; Bracard, S.; Tehindrazanarivelo, A. Autosomal dominant migraine with MRI white-matter abnormalities mapping to the CADASIL locus. *Neurology* **1995**, *45*, 1086–91.

[20] Vahedi, K.; Chabriat, H.; Levy, C.; Joutel, A.; Tournier-Lasserve, E.; Bousser, M.-G. Migraine with aura and brain magnetic resonance imaging abnormalities in patients with CADASIL. *Archives of neurology* **2004**, *61*, 1237–40.

[21] Opherk, C.; Peters, N.; Herzog, J.; Luedtke, R.; Dichgans, M. Long-term prognosis and causes of death in CADASIL: A retrospective study in 411 patients. *Brain* **2004**, *127*, 2533–2539.

[22] Amberla, K.; Wäljas, M.; Tuominen, S.; Almkvist, O.; Pöyhönen, M.; Tuisku, S.; Kalimo, H.; Viitanen, M. Insidious cognitive decline in CADASIL. *Stroke* **2004**, *35*, 1598–1602.

[23] Dichgans, M. Cerebral autosomal dominant arteriopathy with subcortical infarcts and leukoencephalopathy: Phenotypic and mutational spectrum. *Journal of the Neurological Sciences* **2002**, *203-204*, 77–80.

[24] Ruchoux MM1, M. C. CADASIL: Cerebral autosomal dominant arteriopathy with subcortical infarcts and leukoencephalopathy. *J Neuropathol Exp Neurol.* **1997**, *56*, 947–64.

[25] Kalimo, H.; Ruchoux, M.-M.; Viitanen, M.; Kalaria, R. N. CADASIL: a common form of hereditary arteriopathy causing brain infarcts and dementia. *Brain pathology (Zurich, Switzerland)* **2002**, *12*, 371–84.

[26] Dichgans, M.; Mayer, M.; Uttner, I.; Brüning, R.; Müller-Höcker, J.; Rungger, G.; Ebke, M.; Klockgether, T.; Gasser, T. The phenotypic spectrum of CADASIL: clinical findings in 102 cases. *Annals of neurology* **1998**, *44*, 731–739.

[27] Chabriat, H.; Levy, C.; Taillia, H.; Iba-Zizen, M. T.; Vahedi, K.; Joutel, a.; Tournier-Lasserve, E.; Bousser, M. G. Patterns of MRI lesions in CADASIL. *Neurology* **1998**, *51*, 452–457.

[28] Peters, N.; Holtmannspötter, M.; Opherk, C.; Gschwendtner, A.; Herzog, J.; Sämann, P.; Dichgans, M. Brain volume changes in CADASIL: A serial MRI study in pure subcortical ischemic vascular disease. *Neurology* **2006**, *66*, 1517–1522.

[29] Jouvent, E.; Viswanathan, A.; Mangin, J. F.; O'Sullivan, M.; Guichard, J. P.; Gschwendtner, A.; Cumurciuc, R.; Buffon, F.; Peters, N.; Pachaï, C.; Bousser, M. G.; Dichgans, M.; Chabriat, H. Brain atrophy is related to lacunar lesions and tissue microstructural changes in CADASIL. *Stroke* **2007**, *38*, 1786–1790.

[30] Duering, M.; Righart, R.; Csanadi, E.; Jouvent, E.; Herve, D.; Chabriat, H.; Dichgans, M. Incident subcortical infarcts induce focal thinning in connected cortical regions. *Neurology* **2012**, *79*, 2025–2028.

[31] Duering, M.; Csanadi, E.; Gesierich, B.; Jouvent, E.; Hervé, D.; Seiler, S.; Belaroussi, B.; Ropele, S.; Schmidt, R.; Chabriat, H.; Dichgans, M. Incident lacunes preferentially localize to the edge of white matter hyperintensities: insights into the pathophysiology of cerebral small vessel disease. *Brain* **2013**, *136*, 2717–2726.

[32] Okeda, R.; Arima, K.; Kawai, M. Arterial changes in cerebral autosomal dominant arteriopathy with subcortical infarcts and leukoencephalopathy (CADASIL) in relation to pathogenesis of diffuse myelin loss of cerebral white matter: Examination of cerebral medullary arteries by reconstruct. *Stroke* **2002**, *33*, 2565–2569.

[33] Miao, Q.; Paloneva, T.; Tuominen, S.; Pöyhönen, M.; Tuisku, S.; Viitanen, M.; Kalimo, H. Fibrosis and stenosis of the long penetrating cerebral arteries: the cause of the white matter pathology in cerebral autosomal dominant arteriopathy with subcortical infarcts and leukoencephalopathy. *Brain pathology (Zurich, Switzerland)* **2004**, *14*, 358–364.

[34] Kast, J.; Hanecker, P.; Beaufort, N.; Giese, A.; Joutel, A.; Dichgans, M.; Opherk, C.; Haffner, C. Sequestration of latent TGF-β binding protein 1 into CADASIL-related Notch3-ECD deposits. *Acta neuropathologica communications* **2014**, *2*, 96.

[35] Ruchoux, M. M.; Chabriat, H.; Bousser, M. G.; Baudrimont, M.; Tournier-Lasserve, E. Presence of ultrastructural arterial lesions in muscle and skin vessels of patients with CADASIL. *Stroke* **1994**, *25*, 2291–2.

[36] Ruchoux, M. M.; Guerouaou, D.; Vandenhaute, B.; Pruvo, J. P.; Vermersch, P.; Leys, D. Systemic vascular smooth muscle cell impairment in cerebral autosomal dominant arteriopathy with subcortical infarcts and leukoencephalopathy. *Acta Neuropathologica* **1995**, *89*, 500–512.

[37] Ragno, M.; Tournier-lasserve, E.; Fiori, M. G.; Manca, S. A.; Patrosso, M. C.; Ferlini, A.; Sirocchi, G.; Trojano, L.; Chabriat, H.; Salvi, F.; Manca, A.; Patrosso, M. C.; Ferlini, A.; Sirocchi, G.; Trojano, L.; Chabriat, H.; Salvi, F. An Italian kindred with cerebral autosomal dominant arteriopathy with subcortical infarcts and leukoencephalopathy (CADASIL). *Annals of Neurology* **1995**, *38*, 231–236.

[38] Forteza, a. M.; Brozman, B.; Rabinstein, a. a.; Romano, J. G.; Bradley, W. G. Acetazolamide for the treatment of migraine with aura in CADASIL. *Neurology* **2001**, *57*, 2144–2145.

[39] Dichgans, M.; Markus, H. S.; Salloway, S.; Verkkoniemi, A.; Moline, M.; Wang, Q.; Posner, H.; Chabriat, H. S. Donepezil in patients with subcortical vascular cognitive impairment: a randomised double-blind trial in CADASIL. *The Lancet Neurology* **2008**, *7*, 310–318.

[40] Peters, N.; Freilinger, T.; Opherk, C.; Pfefferkorn, T.; Dichgans, M. Enhanced L-arginine-induced vasoreactivity suggests endothelial dysfunction in CADASIL. *Journal of Neurology* **2008**, *255*, 1203–1208.

[41] Artavanis-Tsakonas, S.; Rand, M.; Lake, R. Notch Signaling: Cell Fate Control and Signal Integration in Development. *Science* **1999**, *284*, 770–776.

[42] Blaumueller, C. M.; Qi, H.; Zagouras, P.; Artavanis-Tsakonas, S. Intracellular cleavage of Notch leads to a heterodimeric receptor on the plasma membrane. *Cell* **1997**, *90*, 281–291.

[43] Brou, C.; Logeat, F.; Gupta, N.; Bessia, C.; LeBail, O.; Doedens, J. R.; Cumano, A.; Roux, P.; Black, R. A.; Israël, A. A Novel Proteolytic Cleavage Involved in Notch Signaling. *Molecular Cell* **2000**, *5*, 207–216.

[44] Mumm, J. S.; Schroeter, E. H.; Saxena, M. T.; Griesemer, A.; Tian, X.; Pan, D. J.; Ray, W. J.; Kopan, R. A ligand-induced extracellular cleavage regulates gamma-secretase-like proteolytic activation of Notch1. *Molecular cell* **2000**, *5*, 197–206.

[45] Fouillade, C.; Baron-Menguy, C.; Domenga-Denier, V.; Thibault, C.; Takamiya, K.; Huganir, R.; Joutel, A. Transcriptome analysis for Notch3 target genes identifies Grip2 as a novel regulator of myogenic response in the cerebrovasculature. *Arteriosclerosis, Thrombosis, and Vascular Biology* **2013**, *33*, 76–86.

[46] Nichols, J. T.; Miyamoto, A.; Weinmaster, G. Notch signaling - Constantly on the move. *Traffic* **2007**, *8*, 959–969.

[47] Penton, A. L.; Leonard, L. D.; Spinner, N. B. Notch signaling in development and disease. *Seminars in Cell & Developmental Biology* **2012**, *23*, 450457.

[48] Joutel, a.; Andreux, F.; Gaulis, S.; Domenga, V.; Cecillon, M.; Battail, N.; Piga, N.; Chapon, F.; Godfrain, C.; Tournier-Lasserve, E. The ectodomain of the Notch3 receptor accumulates within the cerebrovasculature of CADASIL patients. *The Journal of clinical investigation* **2000**, *105*, 597–605.

[49] Krebs, L. T.; Xue, Y.; Norton, C. R.; Shutter, J. R.; Maguire, M.; Sundberg, J. P.; Gallahan, D.; Closson, V.; Kitajewski, J.; Callahan, R.; Smith, G. H.; Stark, K. L.; Gridley, T. Notch signaling is essential for vascular morphogenesis in mice. *Genes and Development* **2000**, *14*, 1343–1352.

[50] Domenga, V.; Fardoux, P.; Lacombe, P.; Monet, M.; Maciazek, J.; Krebs, L. T.; Klonjkowski, B.; Berrou, E.; Mericskay, M.; Li, Z.; Tournier-Lasserve, E.; Gridley, T.; Joutel, A. Notch3 is required for arterial identity and maturation of vascular smooth muscle cells. *Genes and Development* **2004**, *18*, 2730–2735.

[51] Belin De Chantemèle, E. J.; Retailleau, K.; Pinaud, F.; Vessières, E.; Bocquet, A.; Guihot, A. L.; Lemaire, B.; Domenga, V.; Baufreton, C.; Loufrani, L.; Joutel, A.; Henrion, D. Notch3 is a major regulator of vascular tone in cerebral and tail resistance arteries. *Arteriosclerosis, Thrombosis, and Vascular Biology* **2008**, *28*, 2216–2224.

[52] Bork, P.; Campebell, I. Epidermal growth factor-like modules. *Current Opinions in Structural Biology* **1993**, *3*, 385–392.

[53] Peters, N.; Opherk, C.; Bergmann, T.; Castro, M.; Herzog, J.; Dichgans, M.; Contribution, O. Spectrum of mutations in biopsy-proven CADASIL: implications for diagnostic strategies. *Archives of neurology* **2005**, *62*, 2–5.

[54] Joutel, A.; Vahedi, K.; Corpechot, C.; Troesch, A.; Chabriat, H.; Vayssi??re, C.; Cruaud, C.; Maciazek, J.; Weissenbach, J.; Bousser, M. G.; Bach, J. F.; Tournier-Lasserve, E. Strong clustering and stereotyped nature of Notch3 mutations in CADASIL patients. *Lancet* **1997**, *350*, 1511–1515.

[55] Monet, M.; Domenga, V.; Lemaire, B.; Souilhol, C.; Langa, F.; Babinet, C.; Gridley, T.; Tournier-Lasserve, E.; Cohen-Tannoudji, M.; Joutel, A. The archetypal R90C CADASIL-NOTCH3 mutation retains NOTCH3 function in vivo. *Human Molecular Genetics* **2007**, *16*, 982–992.

[56] Haritunians, T.; Boulter, J.; Hicks, C.; Buhrman, J.; DiSibio, G.; Shawber, C.; Weinmaster, G.; Nofziger, D.; Schanen, C. CADASIL Notch3 mutant proteins localize to the cell surface and bind ligand. *Circulation Research* **2002**, *90*, 506–508.

[57] Karlström, H.; Beatus, P.; Dannaeus, K.; Chapman, G.; Lendahl, U.; Lundkvist, J. A CADASIL-mutated Notch 3 receptor exhibits impaired intracellular trafficking and maturation but normal ligand-induced signaling. *Proceedings of the National Academy of Sciences of the United States of America* **2002**, *99*, 17119–17124.

[58] Joutel, A.; Monet, M.; Domenga, V.; Riant, F.; Tournier-Lasserve, E. Pathogenic Mutations Associated with Cerebral Autosomal Dominant Arteriopathy with Subcortical Infarcts and Leukoencephalopathy Differently Affect Jagged1 Binding and Notch3 Activity via the RBP/JK Signaling Pathway. *The American Journal of Human Genetics* **2004**, *74*, 338–347.

[59] Peters, N.; Opherk, C.; Zacherle, S.; Capell, A.; Gempel, P.; Dichgans, M. CADASIL-associated Notch3 mutations have differential effects both on ligand binding and ligand-induced Notch3 receptor signaling through RBP-Jk. *Experimental Cell Research* **2004**, *299*, 454–464.

[60] Low, W. C.; Santa, Y.; Takahashi, K.; Tabira, T.; Kalaria, R. N. CADASIL-causing mutations do not alter Notch3 receptor processing and activation. *Neuroreport* **2006**, *17*, 945–949.

[61] Dubroca, C.; Lacombe, P.; Domenga, V.; Maciazek, J.; Levy, B.; Tournier-Lasserve, E.; Joutel, A.; Henrion, D. Impaired vascular mechanotransduction in a transgenic mouse model of CADASIL arteriopathy. *Stroke* **2005**, *36*, 113–117.

[62] Monet-Lepretre, M.; Bardot, B.; Lemaire, B.; Domenga, V.; Godin, O.; Dichgans, M.; Tournier-Lasserve, E.; Cohen-Tannoudji, M.; Chabriat, H.; Joutel, A.

Distinct phenotypic and functional features of CADASIL mutations in the Notch3 ligand binding domain. *Brain* **2009**, *132*, 1601–1612.

[63] Joutel, A.; Monet-Lepretre, M.; Gosele, C.; Baron-Menguy, C.; Hammes, A.; Schmidt, S.; Lemaire-Carrette, B.; Domenga, V.; Schedl, A.; Lacombe, P.; Hubner, N. Cerebrovascular dysfunction and microcirculation rarefaction precede white matter lesions in a mouse genetic model of cerebral ischemic small vessel. *J Clin Invest* **2010**, *120*, 433–45.

[64] Wallays, G.; Nuyens, D.; Silasi-Mansat, R.; Souffreau, J.; Callaerts-Vegh, Z.; Van Nuffelen, A.; Moons, L.; D'Hooge, R.; Lupu, F.; Carmeliet, P.; Collen, D.; Dewerchin, M. Notch3 Arg170Cys knock-in mice display pathologic and clinical features of the neurovascular disorder cerebral autosomal dominant arteriopathy with subcortical infarcts and leukoencephalopathy. *Arteriosclerosis, Thrombosis, and Vascular Biology* **2011**, *31*, 2881–2888.

[65] Joutel, A. Pathogenesis of CADASIL: Transgenic and knock-out mice to probe function and dysfunction of the mutated gene, Notch3, in the cerebrovasculature. *BioEssays* **2011**, *33*, 73–80.

[66] Ishiko, A.; Shimizu, A.; Nagata, E.; Takahashi, K.; Tabira, T.; Suzuki, N. Notch3 ectodomain is a major component of granular osmiophilic material (GOM) in CADASIL. 2006.

[67] Mayer, M.; Straube, A.; Bruening, R.; Uttner, I.; Pongratz, D.; Gasser, T.; Dichgans, M.; Müller-Höcker, J. Muscle and skin biopsies are a sensitive diagnostic tool in the diagnosis of CADASIL. *Journal of Neurology* **1999**, *246*, 526–532.

[68] Lesnik Oberstein, S. A. J.; van Duinen, S. G.; van den Boom, R.; Maat-Schieman, M. L. C.; van Buchem, M. A.; van Houwelingen, H. C.; Hegeman-Kleinn, I. M.; Ferrari, M. D.; Breuning, M. H.; Haan, J. Evaluation of diagnostic NOTCH3 immunostaining in CADASIL. *Acta Neuropathologica* **2003**, *106*, 107–111.

[69] Dichgans, M.; Ludwig, H.; Müller-Höcker, J.; Messerschmidt, a.; Gasser, T. Small in-frame deletions and missense mutations in CADASIL: 3D models predict misfolding of Notch3 EGF-like repeat domains. *European journal of human genetics : EJHG* **2000**, *8*, 280–5.

[70] Opherk, C.; Duering, M.; Peters, N.; Karpinska, A.; Rosner, S.; Schneider, E.; Bader, B.; Giese, A.; Dichgans, M. CADASIL mutations enhance spontaneous multimerization of NOTCH3. *Human Molecular Genetics* **2009**, *18*, 2761–2767.

[71] Duering, M.; Karpinska, A.; Rosner, S.; Hopfner, F.; Zechmeister, M.; Peters, N.; Kremmer, E.; Haffner, C.; Giese, A.; Dichgans, M.; Opherk, C. Co-aggregate formation of CADASIL-mutant NOTCH3: a single-particle analysis. *Human molecular genetics* **2011**, *20*, 3256–3265.

[72] Monet-Leprêtre, M.; Haddad, I.; Baron-Menguy, C.; Fouillot-Panchal, M.; Riani, M.; Domenga-Denier, V.; Dussaule, C.; Cognat, E.; Vinh, J.; Joutel, A. Abnormal recruitment of extracellular matrix proteins by excess Notch3 ECD: a new pathomechanism in CADASIL. *Brain : a journal of neurology* **2013**, *136*, 1830–45.

[73] Rutten, J. W.; Haan, J.; Terwindt, G. M.; van Duinen, S. G.; Boon, E. M.; Lesnik Oberstein, S. A. Interpretation of NOTCH3 mutations in the diagnosis of CADASIL. *Expert Review of Molecular Diagnostics* **2014**, *14*, 593–603.

[74] Uchino, M.; Hirano, T.; Uyama, E.; Hashimoto, Y.; Xwrvrpdo, H.; Uwhulrsdwk, R.; Dqg, Q. Cerebral autosomal dominant arteriopathy with subcortical infarcts and leukoencephalopathy (CADASIL) and CADASIL-like disorders in Japan. *Ann N Y Acad Sci* **2002**, *977*, 273–8.

[75] Santa, Y.; Uyama, E.; Chui, D. H.; Arima, M.; Kotorii, S.; Takahashi, K.; Tabira, T. Genetic, clinical and pathological studies of CADASIL in Japan: A partial contribution of Notch3 mutations and implications of smooth muscle cell degeneration for the pathogenesis. *Journal of the Neurological Sciences* **2003**, *212*, 79–84.

[76] Mazzei, R.; Conforti, F. L.; Lanza, P. L.; Sprovieri, T.; Lupo, M. R.; Gallo, O.; Patitucci, A.; Magariello, A.; Caracciolo, M.; Gabriele, A. L.; Fera, F.; Valentino, P.; Bono, F.; Cenacchi, G.; Santoro, G.; Muglia, M.; Quattrone, A. A novel Notch3 gene mutation not involving a cysteine residue in an Italian family with CADASIL. *Neurology* **2004**, *63*, 561–564.

[77] Kim, Y.; Choi, E. J.; Choi, C. G.; Kim, G.; Choi, J. H.; Yoo, H. W.; Kim, J. S. Characteristics of CADASIL in Korea: a novel cysteine-sparing Notch3 mutation. *Neurology* **2006**, *66*, 1511–6.

[78] Choi, J. C.; Kang, S.-Y.; Kang, J.-H.; Park, J.-K. Intracerebral hemorrhages in CADASIL. *Neurology* **2006**, *67*, 2042–4.

[79] Mizuno, T.; Muranishi, M.; Torugun, T.; Tango, H.; Nagakane, Y.; Kudeken, T.; Kawase, Y.; Kawabe, K.; Oshima, F.; Yaoi, T.; Itoh, K.; Fushiki, S.; Nakagawa, M. Two Japanese CADASIL Families Exhibiting Notch3 Mutation R75P Not Involving Cysteine Residue. *Internal Medicine* **2008**, *47*, 2067–2072.

[80] Ferreira, S.; Malheiro, F.; Oliveira, J. P. Novel human pathological mutations. *Human genetics* **2008**, *123*, 537–555.

[81] Scheid, R.; Heinritz, W.; Leyhe, T.; Thal, D. R.; Schober, R.; Strenge, S.; von Cramon, D. Y.; Froster, U. G. Cysteine-sparing Notch3 Mutations: CADASIL or CADASIL variants? *Neurology* **2008**, *71*, 774–776.

[82] Brass, S. D.; Smith, E. E.; Arboleda-Velasquez, J. F.; Copen, W. A.; Frosch, M. P. Case records of the Massachusetts General Hospital. Case 12-2009. A 46-year-old man with migraine, aphasia, and hemiparesis and similarly affected family members. *N Engl J Med* **2009**, *360*, 1656–65.

[83] Wang, Z.; Yuan, Y.; Zhang, W.; Lv, H.; Hong, D.; Chen, B.; Liu, Y.; Luan, X.; Xie, S.; Wu, S. NOTCH3 mutations and clinical features in 33 mainland Chinese families with CADASIL. *Journal of neurology, neurosurgery, and psychiatry* **2011**, *82*, 534–9.

[84] Kim, Y. E.; Yoon, C. W.; Seo, S. W.; Ki, C. S.; Kim, Y. B.; Kim, J. W.; Bang, O. Y.; Lee, K. H.; Kim, G. M.; Chung, C. S.; Na, D. L. Spectrum of NOTCH3 mutations in Korean patients with clinically suspicious cerebral autosomal dominant arteriopathy with subcortical infarcts and leukoencephalopathy. *Neurobiology of Aging* **2014**, *35*, 726.e1–726.e6.

[85] Wollenweber, F. A.; Hanecker, P.; Bayer-Karpinska, A.; Malik, R.; Bäzner, H.; Moreton, F.; Muir, K. W.; Müller, S.; Giese, A.; Opherk, C.; Dichgans, M.; Haffner, C.; Duering, M. Cysteine-Sparing CADASIL Mutations in NOTCH3 Show Proaggregatory Properties In Vitro. *Stroke* **2015**, *46*, 786–792.

[86] Ungaro, C.; Mazzei, R.; Conforti, F. L.; Sprovieri, T.; Servillo, P.; Liguori, M.; Citrigno, L.; Gabriele, a. L.; Magariello, a.; Patitucci, a.; Muglia, M.; Quattrone, a. CADASIL: extended polymorphisms and mutational analysis of the NOTCH3 gene. *Journal of neuroscience research* **2009**, *87*, 1162–7.

[87] Ampuero, I.; Alegre-Abarrategui, J.; Rodal, I.; España, A.; Ros, R.; Sendón, J. L. L.; Galloway, E. G.; Cervelló, A.; Caminero, A. B.; Zabala, A.; Erro, E.; Jarauta, F.; Morlán, L.; López-Valdés, E.; Aladro, Y.; Seijo, M.; Rivas, G. G.; Muñoz, D. G.; de Yébenes, J. G. On the diagnosis of CADASIL. *Journal of Alzheimer's disease : JAD* **2009**, *17*, 787–94.

[88] Schwille, P. Fluoreszenz-Korrelations-Spektroskopie : Analyse biochemischer Systeme auf Einzelmolekülebene. Ph.D. thesis, Technical University Braunschweig, 1996.

[89] Schwille, P.; Meyer-Almes, F. J.; Rigler, R. Dual-color fluorescence cross-correlation spectroscopy for multicomponent diffusional analysis in solution. *Biophysical journal* **1997**, *72*, 1878–1886.

[90] Bieschke, J.; Giese, A.; Schulz-Schaeffer, W.; Zerr, I.; Poser, S.; Eigen, M.; Kretzschmar, H. Ultrasensitive detection of pathological prion protein aggregates by dual-color scanning for intensely fluorescent targets. *Proceedings of the National Academy of Sciences of the United States of America* **2000**, *97*, 5468–5473.

[91] Giese, A.; Bieschke, J.; Eigen, M.; Kretzschmar, H. A. Putting prions into focus: application of single molecule detection to the diagnosis of prion diseases. *Archives of virology. Supplementum* **2000**, 161–171.

[92] Giese, A.; Bader, B.; Bieschke, J.; Schaffar, G.; Odoy, S.; Kahle, P. J.; Haass, C.; Kretzschmar, H. Single particle detection and characterization of synuclein coaggregation. *Biochemical and Biophysical Research Communications* **2005**, *333*, 1202–1210.

[93] Los, G. V.; Wood, K. *Methods in Molecular Biology: High Content Screening: A Powerful Approach to Systems Cell Biology and Drug Discovery*; 2006; Vol. 356; pp 195–208.

[94] Durocher, Y.; Perret, S.; Kamen, A. High-level and high-throughput recombinant protein production by transient transfection of suspension-growing human 293-EBNA1 cells. *Nucleic acids research* **2002**, *30*, E9.

[95] Bentley, P.; Wang, T.; Malik, O.; Nicholas, R.; Ban, M.; Sawcer, S.; Sharma, P. CADASIL with cord involvement associated with a novel and atypical NOTCH3 mutation. *Journal of neurology, neurosurgery, and psychiatry* **2011**, *82*, 855–60.

[96] Caruana, M.; Högen, T.; Levin, J.; Hillmer, A.; Giese, A.; Vassallo, N. Inhibition and disaggregation of α-synuclein oligomers by natural polyphenolic compounds. *FEBS letters* **2011**, *585*, 1113–1120.

[97] Caruana, M.; Neuner, J.; Högen, T.; Schmidt, F.; Kamp, F.; Scerri, C.; Giese, A.; Vassallo, N. Polyphenolic compounds are novel protective agents against lipid membrane damage by α-synuclein aggregates in vitro. *Biochimica et biophysica acta* **2012**, *1818*, 2502–10.

[98] Wagner, J.; Ryazanov, S.; Leonov, A.; Levin, J.; Shi, S.; Schmidt, F.; Prix, C.; Pan-Montojo, F.; Bertsch, U.; Mitteregger-Kretzschmar, G.; Geissen, M.; Eiden, M.; Leidel, F.; Hirschberger, T.; Deeg, A. a.; Krauth, J. J.; Zinth, W.; Tavan, P.; Pilger, J.; Zweckstetter, M.; Frank, T.; Bähr, M.; Weishaupt, J. H.; Uhr, M.; Urlaub, H.; Teichmann, U.; Samwer, M.; Bötzel, K.; Groschup, M.; Kretzschmar, H.; Griesinger, C.; Giese, A. Anle138b: a novel oligomer modulator for disease-modifying therapy of neurodegenerative diseases such as prion and Parkinson's disease. *Acta neuropathologica* **2013**, *125*, 795–813.

[99] Tomás-Barberán, F. a.; Andrés-Lacueva, C. Polyphenols and health: current state and progress. *Journal of agricultural and food chemistry* **2012**, *60*, 8773–5.

[100] Vassallo, N. In *Polyphenols and Health: New and recent advances*; Vassallo, N., Ed.; Nova Science Publishers, Inc., New York, 2008; pp 7 x 10, 394pp.

[101] Scharrer, E. Consequences of HtrA1 deficiency on TGF-β signaling. Ph.D. thesis, 2014.

[102] Quattrone, A.; Mazzei, R. Cysteine-sparing NOTCH3 mutations: CADASIL or CADASIL variants? *Neurology* **2009**, *72*, 2135–2136.

[103] Haffner, C.; Malik, R.; Dichgans, M. Genetic factors in cerebral small vessel disease and their impact on stroke and dementia. *Journal of Cerebral Blood Flow & Metabolism* **2015**, 1–10.

[104] Bertsch, U.; Winklhofer, K. F.; Hirschberger, T.; Bieschke, J.; Weber, P.; Hartl, F. U.; Tavan, P.; Tatzelt, J.; Kretzschmar, H. a.; Giese, A. Systematic identification of antiprion drugs by high-throughput screening based on scanning for intensely fluorescent targets. *Journal of virology* **2005**, *79*, 7785–7791.

[105] Stefani, M.; Rigacci, S. Beneficial properties of natural phenols: Highlight on protection against pathological conditions associated with amyloid aggregation. *BioFactors* **2014**, 482–493.

[106] Haritunians, T.; Chow, T.; De Lange, R. P. J.; Nichols, J. T.; Ghavimi, D.; Dorrani, N.; St Clair, D. M.; Weinmaster, G.; Schanen, C. Functional analysis of a recurrent missense mutation in Notch3 in CADASIL. *Journal of neurology, neurosurgery, and psychiatry* **2005**, *76*, 1242–8.

[107] Watanabe-Hosomi, A.; Watanabe, Y.; Tanaka, M.; Nakagawa, M.; Mizuno, T. Transendocytosis is impaired in CADASIL-mutant NOTCH3. *Experimental Neurology* **2012**, *233*, 303–311.

[108] Meng, H.; Zhang, X.; Yu, G.; Lee, S. J.; Chen, Y. E.; Prudovsky, I.; Wang, M. M. Biochemical Characterization and Cellular Effects of CADASIL Mutants of NOTCH3. *PLoS ONE* **2012**, *7*, 1–13.

[109] Tikka, S.; Peng Ng, Y.; Di Maio, G.; Mykkänen, K.; Siitonen, M.; Lepikhova, T.; Pöyhönen, M.; Viitanen, M.; Virtanen, I.; Kalimo, H.; Baumann, M. CADASIL mutations and shRNA silencing of NOTCH3 affect actin organization in cultured vascular smooth muscle cells. *Journal of Cerebral Blood Flow & Metabolism* **2012**, 2171–2180.

[110] Viitanen, M.; Sundström, E.; Baumann, M.; Poyhonen, M.; Tikka, S.; Behbahani, H. Experimental studies of mitochondrial function in CADASIL vascular smooth muscle cells. *Experimental Cell Research* **2013**, *319*, 134–143.

[111] Ghosh, M.; Balbi, M.; Hellal, F.; Dichgans, M.; Lindauer, U.; Plesnila, N. Pericytes are involved in the pathogenesis of cerebral autosomal dominant arteriopathy with subcortical infarcts and leukoencephalopathy. *Annals of Neurology* **2015**, *78*, 887–900.

[112] Capone, C.; Cognat, E.; Ghezali, L.; Baron-Menguy, C.; Aubin, D.; Mesnard, L.; Stöhr, H.; Domenga-Denier, V.; Nelson, M. T.; Joutel, A. Reducing Timp3 or vitronectin ameliorates disease manifestations in CADASIL mice. *Annals of Neurology* **2016**, *79*, 387–403.

[113] Gilman, S.; Koller, M.; Black, R.; Jenkins, L.; Griffith, S.; Fox, N.; Eisner, L.; Kirby, L.; Rovira, M. B.; Forette, F.; Orgogozo, J. Clinical Effect of AB immunization(AN1792) in patients with AD in an interrupted trial. *Neurology* **2005**, *64*, 1553–1562.

[114] Rutten, J. W.; Dauwerse, H. G.; Peters, D. J. M.; Goldfarb, A.; Venselaar, H.; Haffner, C.; Van Ommen, G. J. B.; Aartsma-Rus, A. M.; Lesnik Oberstein, S. A. J. Therapeutic NOTCH3 cysteine correction in CADASIL using exon skipping: In vitro proof of concept. *Brain* **2016**, *139*, 1123–1135.

[115] Veltrop, M.; Aartsma-Rus, A. Antisense-mediated exon skipping: Taking advantage of a trick from Mother Nature to treat rare genetic diseases. *Experimental Cell Research* **2014**, *325*, 50–55.

[116] evotec OAI, *FCS +plus Theory and Handling*; 2001; Vol. 49.

Acronyms

τ_{diff} . . . . . diffusion time
α-syn . . . . . α-synuclein
β-ME . . . . . β-mercaptoethanol
Notch3 $^{-/-}$ . . . . . Notch3 knockout

AD . . . . . Alzheimer's disease
AON . . . . . antisense oligonucleotide
APD . . . . . avalanche photo diode
APS . . . . . ammonium persulfate

BSA . . . . . bovine serum albumin
BTE . . . . . black tea extract

CADASIL . . . . . cerebral autosomal dominant arteriopathy with subcortical infarcts and leukoencephalopathy
CARASIL . . . . . cerebral autosomal recessive arteriopathy with subcortical infarcts and leukoencephalopathy
CBB . . . . . Coomassie brilliant blue
CBF . . . . . cerebral blood flow
CJD . . . . . Creutzfeldt-Jakob disease
CMV . . . . . cytomegalovirus
CPP . . . . . counts per particle

DAPI . . . . . 4'6-diamidino-2-phenylindole
DMD . . . . . Duchenne muscular dystrophy
DMEM . . . . . Dulbecco's Modified Eagle Medium
DMSO . . . . . dimethyl sulfoxide
DOC . . . . . deoxycholic acid
DPP . . . . . diphenylpyrazole
DTT . . . . . dithiothreitol

ECD . . . . . extracellular domain
ECM . . . . . extracellular matrix
EDTA . . . . . ethylenediaminetetraacetic acid
EGCG . . . . . (-)-epigallocatechin gallate
EGF . . . . . epidermal growth factor

ESP . . . . . exome sequencing project

FBS . . . . . fetal bovine serum
FCS . . . . . fluorescence correlation spectroscopy
FIDA . . . . . fluorescence intensity distribution analysis
FTD . . . . . frontotemporal dementia

G418 . . . . . G418 sulfate, geneticin
GOM . . . . . granular osmiophilic material

H_2O_{bidest} . . . . . double distilled water
HD . . . . . Huntington disease
HRP . . . . . horseradish peroxidase

I_{tot} . . . . . total intensity
ICD . . . . . intracellular domain
ISD . . . . . Institute for stroke and dementia research

kDa . . . . . kilodalton

LB medium . . . . . lysogeny broth medium
LNR . . . . . lin12/notch repeats
LRS . . . . . ligand recognition site
LTBP-1 . . . . . latent TGF-β binding protein

MEF . . . . . mouse embryonic fibroblast
MRI . . . . . magnetic resonance imaging

Notch3-EGF$_{1-5}$ . . Notch3 fragment containing EGF-like repeats $1-5$
Notch3-ECD . . . . extracellular domain of Notch3

o/n . . . . . over night
OH group . . . . . hydroxyl group

p/s . . . . . penicillin/streptomycin solution
PAC . . . . . P1-derived artificial chromosome
PAGE . . . . . polyacrylamide gel electrophoresis
PBS . . . . . phosphate buffered saline
PCR . . . . . polymerase chain reaction
PD . . . . . Parkinson's disease
PDGFRβ . . . . . platelet-derived growth factor receptor beta
PEI . . . . . polyethylenimine
PFA . . . . . paraformaldehyde
PI . . . . . protease inhibitor
PrP . . . . . prion protein

PVDF . . . . . polyvinylidene fluoride

RT . . . . . room temperature
RVCL . . . . . retinal vasculopathy with cerebral leukodystrophy

SDS . . . . . sodium dodecyl sulfate
SEM . . . . . standard error of the mean
SIFT . . . . . scanning for intensely fluorescent targets
SMA . . . . . spinal muscular atrophy
SNP . . . . . single nucleotide polymorphism
SVD . . . . . small vessel disease

TACE . . . . . TNFα-converting enzyme
TEMED . . . . . tetramethyletylenediamine
TEV . . . . . tobacco etch virus
TM . . . . . transmembrane domain
TNT . . . . . Tris-HCl, NaCl, Tween
Tris . . . . . tris(hydroxymethyl)aminoethane
TSP-2 . . . . . thrombospondin 2

vSMC . . . . . vascular smooth muscle cell

WMH . . . . . white matter hyperintensities
wt . . . . . wild-type

List of Figures

List of Tables

Publications and meetings

Publications

Wollenweber, F.A.*; **Hanecker, P.***; Bayer-Karpinska, A.; Malik, R.; Bäzner, H.; Moreton, F., Muir, K.W.; Müller, S.; Giese, A.; Opherk, C.; Dichgans, M.; Haffner, C.; Duering, M. Cysteine-sparing CADASIL mutations in NOTCH3 show proaggregatory properties in vitro. *Stroke* **2015**, *46*, 786-792

* joint first authors

Kast, J.; **Hanecker, P.**; Beaufort, N.; Giese, A.; Joutel, A.; Dichgans M.; Opherk, C.; Haffner, C. Sequestration of latent TGF-β binding protein 1 into CADASIL-related Notch3-ECD deposits. *Acta neuropathologica communications* **2014**, *2*, 96

Sugiarto, S.; Persson A.I.; Munoz E.G.; Waldhuber M.; Lamagna, C.; Andor, N.; **Hanecker, P.**; Ayers-Ringler, J.; Phillips, J.; Siu, J.; Lim, D.A.; Vandenberg, S.; Stallcup, W.; Berger, M.S., Bergers, G.; Weiss, W.A.; Petritsch, C. Asymmetry-defective oligodendrocyte progenitors are glioma precursors. *Cancer Cell* **2011**, *20*, 328-340

Geiger, S.R.; Lorenzen, K.; Schreieck A.; **Hanecker, P.**; Kostrewa, D.; Heck, A.J., Cramer, P. RNA polymerase I contains a TFIIF-related DNA-binding subcomplex. *Mol Cell* **2010**, *39*, 583-594

Meetings

October 2013	The Notch Meeting, Athens, Greece	Oral presentation
March 2013	<interact> 2013, Munich, Germany	Poster presentation
January 2013	ANIM, Mannheim, Germany	Poster presentation

Acknowledgements

An erster Stelle gilt mein Dank **Prof. Dr. Don Lamb** für die Übernahme der Fachvertretung, seiner investierten Zeit und dem großen Interesse, das er meiner Arbeit entgegen gebracht hat. **Prof. Dr. Martin Dichgans** möchte ich dafür danken, dass er mir die Möglichkeit gegeben hat, an seinem gut ausgestatteten Institut meine Doktorarbeit durchzuführen.

Mein besonderer Dank gilt **Prof. Dr. Christian Opherk**, der mich durch die ersten drei Jahre meiner Doktorarbeit geleitet hat und dessen Begeisterung und Motivation unglaublich ansteckend waren. In gleicher Weise bedanke ich mich ganz herzlich bei **PD Dr. Christof Haffner**, der die weitere Betreuung meiner Arbeit übernommen und mich besonders in der kritischen Phase an die Hand genommen hat. Danke, dass Deine Tür immer für mich offen stand, Du mich bei allen Problemen und Wissensfragen trotz aller "nein, aber..." unterstützt hast und immer daran geglaubt hast, dass diese Arbeit irgendwann tatsächlich noch ein Ende finden wird. Ich werde die endlosen Diskussionen mit Dir wirklich vermissen! **Prof. Dr. Armin Giese** möchte ich danken für die herzliche Beherbergung in seinem Labor während der SIFT-Messungen, für seine guten Ideen beim Planen und Auswerten der Experimente und seinem unendlichen Fachwissen, das er sehr gut verständlich an den Doktoranden gebracht hat.

PD Dr. Dietmar Martin, **Prof. Dr. Klaus Förstemann** und **Prof. Dr. Christian Wahl-Schott** danke ich für die Bewertung dieser Arbeit und deren Bereitschaft an der Prüfungskommission teilzunehmen.

Des Weiteren danke ich **Dr. Anna Bayer-Karpinska** für ihre Starthilfe bei meinen SIFT-Experimenten und **PD Dr. Marco Düring** für seine Hilfe bei meiner Arbeit.

Barbara Lindner möchte ich danken für die kräftige Unterstützung im Labor, vor allem bei den Aufreinigungen und die unterhaltsamen tierischen Fachsimpeleien. **Daniel Loose** gebührt ein großer Dank für die Lösung meiner abstrusesten Computerprobleme und für die lustigen Hagelgrill-, Berggeh- und Wiesnaktionen.

Felix Schmidt, **Martin Bartels** und **Viktoria Ruf** aus dem Giese-Labor danke ich für die herzliche Aufnahme an meinem Zweit-arbeits/wohn-platz, für die musikalische Untermalung des Labor-Alltags und für die Hilfe bei meinen Experimenten. Ohne Euch hätte ich mir die Füße platt gelaufen und wäre komplett am SIFT-Reader verzweifelt.

Ebenso möchte ich allen **ISD Mitarbeitern** für die gute Zusammenarbeit, die Hilfsbereitschaft und die tolle Atmosphäre danken.

Ein ganz besonderer Dank gilt den drei Labor-Weibsen, **Eva Scharrer**, **Caroline Prell-Schicker** und **Jessica Schorr**. Entstanden durch den gemeinsamen Leidensdruck mit einer dreischichtigen Lösung als Katalysator, verbunden durch eine große Ansammlung an schlechten Witzen, noch schlechteren Liedern und vielen unvergesslichen Erlebnissen, ließ mich unsere Freundschaft den täglichen Wahnsinn überleben. Erst durch Eure Motivation und Eurem unglaublich hartnäckigen Antreiben existiert diese Arbeit in ihrer vollendeten Form.

Ein Herzensdank geht an all meine **Freunde** für ihre Unterstützung jeglicher Art. Euch alle beim Namen zu nennen, würde hier den Rahmen sprengen, aber fühlt Euch alle angesprochen und umarmt. Durch Eure Ablenkung in der Freizeit, Euer Mitfiebern und Antreiben habt Ihr einen nicht unerheblichen Teil zu dieser Arbeit beigetragen.

Ein ganz besonderer Dank gilt meinen Eltern **Annemarie** und **Johann**. Ihr steht voller Überzeugung hinter mir und habt mir immer das Gefühl gegeben, dass ich das Richtige mache.

Schließlich danke ich von ganzem Herzen meinem mittlerweile angetrauten Mann **Flo**. Du hast mich in all den schwierigen Phasen mit stoischer Ruhe ertragen, mir immer Halt gegeben und mich stets tatkräftig unterstützt. Danke, dass Du immer an mich glaubst. Und zum Schluß möchte ich noch der Jüngsten im Bunde danken, unserer Tochter **Felicitas**, die eine kleine kraftschöpfende Pause in diese Arbeit gebracht hat und mir gezeigt hat, dass man auch am Schluß das Ganze am besten tiefenentspannt angehen sollte.